Numerical Investigations of Coherent Structures in Axial Flow in Single Rod-Channel Geometry

Santosh K Gurunath

PNR-131-2012-011
29th August 2012

Faculty of Applied Sciences

Section Physics of Nuclear Reactors
Department Radiation, Radionuclide's and Reactors
Faculty of Applied Physics
Delft University of Technology
Mekelweg 15, 2629 JB Delft
The Netherlands

Numerical Investigations of Coherent Structures in Axial Flow in Single Rod-Channel Geometry

Santosh K Gurunath

MSc Chemical Engineering
Student number: 4119363

MSc Thesis

Starting date: 1 December 2011
End date: 29 August 2012

Supervisors:
Dr. ir. Martin Rohde
Dr. Eng. Luis Portela

Committee Members:
Dr. ir. Martin Rohde
Dr. Eng. Luis Portela
Prof dr. ir. Chris Kleijn
Dr. Dipl. Ing. Sasa Kenjeres

Abstract

In order to ramp up the conversion ratios and burn-up of nuclear reactors, it is inevitable to go to tightly packed fuel rods in the reactor. These nuclear reactors with tightly packed rod-bundles are characterized by interesting flow patterns, different from the ones encountered in regular channel and pipe flows. The correct prediction and control of the flow distribution is essential for the reactor design and safety assessment, and has been an active area of research in reactor thermal-hydraulics. Apart from the axial flow of coolant parallel to the rod bundles, there exists cross-flow between the sub-channels.

The cross-flow promotes homogeneous enthalpy distribution and enhanced mixing between the coolant flowing in the sub-channels. Turbulent mixing is an important phenomenon, which influences the flow and temperature patterns in the rod bundles. Large-scale coherent structures along with transverse flow pulsations have been identified in the rod-rod and rod-wall gap regions. This large-scale structure has a quasi-periodic behavior and is considered an important factor for high mixing-rate.

The aim of this work is to get a better understanding of the flow in a rod-bundle. This is done by performing numerical investigations on a simplified rod-channel geometry. The Unsteady Reynolds Averaged Navier Stokes equations are solved using the Computational Fluid Dynamics software OpenFOAM. Extensive benchmark and validation studies were done in order to determine the simulation technique that offers a good balance between computational cost and accuracy. The flow dynamics and the transport and mixing of a passive scalar due to the coherent structures are studied.

Different turbulence models were used to study their effect on flow dynamics, and no major differences were observed. Following this, the computationally cheaper $k - \varepsilon$ turbulence model with wall functions was chosen for the simulations. The time required for flow development in this geometry was significantly higher than that in regular turbulent channel or pipe flow. This led to different results than the ones observed in the experiments and in previous simulation results published in the literature. It was concluded that the flow in the experiments was not fully developed and that probably not enough time was used to allow flow development in the previous simulations. Our results indicate that the shear-layer becomes thinner and the number of structures decreased with flow development, which would explain the higher number of structures found in previous simulations.

High values of velocity fluctuations and the kinetic energy due to these fluctuations indicated the presence of structures in the near-gap region. Large-scale three-dimensional counter-rotating sledge-shaped structures were observed via the flow visualization of resolved velocity. These structures were not only restricted to the gap region, but encompassed the entire flow domain. The high periodicity and stability of these structures indicate that they are not *turbulence structures*.

The effect of gap-size on the coherent structures was studied, and this study suggested that the presence of more than one mechanism for the formation of these structures. A critical gap-size was obtained, at which the intensity of the structures

has a maximum value, and a cut-off gap size was identified, at which a transition takes place between the two mechanisms.

The coherent structures were found to play a significant role in both the transport and mixing of the passive scalar. The contribution were similar to that of the turbulent diffusion. The simulations indicate that the effect of the coherent structures on the transport and mixing of a passive scalar is of the same order of magnitude of the effect of the turbulent diffusion.

Acknowledgements

Firstly, I would like to to thank my supervior, Martin Rohde for giving me an opportunity to do the MSc thesis at the Physics of Nuclear Reactors group. The weekly meetings with him along with the regular feedbacks played a very important role towards completion of the thesis. His constant encouragement even at difficult times was something which I am really thankful for.

I am greatly indebted to my daily supervisor, Luis Portela, without whom I would not have been able to complete the thesis. The highly insightful technical discussions played a crucial role in the progress of the work. His dedication and commitment towards the supervision of the thesis was one of my main motivation towards working hard.

I would also like to express my highest gratitude to the PhD students, Bernhard Righolt (TNW) and Hoang Duong (TNW) who were really patient and helpful with all my queries on OpenFOAM. Without them, I would have taken a far longer time to learn the software. I would also like to thank Galileu de Oliveira, Maolong Liu and Bernhard Gschaider for their help on various aspects of OpenFOAM.

Next, I would like to thank Rick Bulk for his insights into the experimental aspects of flow in rod-bundles. General discussions with Rick on coherent structures, flow development etc were very helpful while writing certain sections of the thesis.

Many thanks go to the support staff of both PNR and MSP for their help with the administrative issues. I am also thankful to all my PNR colleagues and the cluster administrator for co-operating with my excessive usage of the processors, without which the simulations would have never ended.

Finally, I would like to thank my friends and family for their support and encouragement throught the MSc programme and the thesis.

List of Symbols

Latin Symbols

Symbol	Description	Units
A	Area	$[m^2]$
A_c	Area of cross-section	$[m^2]$
B	Constant	[ ]
$C_{\nu 1}$	Constant	[ ]
C_s	Model constant in LRR turbulence model	[ ]
C_p	Specific heat	$[JK^{-1}]$
C_ε	Model constant in LRR turbulence model	[ ]
$C_{\varepsilon 1}$	Model constant in $k-\varepsilon$ and LRR turbulence model	[ ]
$C_{\varepsilon 2}$	Model constant in $k-\varepsilon$ and LRR turbulence model	[ ]
C_μ	Model constant in $k-\varepsilon$ and LRR turbulence model	[ ]
D	Rod diameter	$[m]$
D_h	Hydraulic diameter	$[m]$
D_h^{gap}	Hydraulic diameter of the gap	$[m]$
f_p	Peak frequency	$[s^{-1}]$
k	Turbulence kinetic energy	$[m^2s^{-2}]$
k_p	Turbulence kinetic energy at the first cell next to the wall	$[m^2s^{-2}]$
k_c	Kinetic energy of resolved fluctuations	$[m^2s^{-2}]$
k_nc	Un-resolved turbulence kinetic energy	$[m^2s^{-2}]$
l	Mixing-length	$[m]$
l_0	Characteristic length of the domain	$[m]$
L_z	Streamwise length	$[m]$
p	Pressure	$[N/m^2]$
P_k	Production of turbulence kinetic energy	$[m^2s^{-3}]$
P_{ij}	Generation of Reynolds-stress	$[m^2s^{-3}]$
P_w	Wetted perimeter	$[m]$
P/D	Rod-rod gap size	[ ]
q_w	Heat flux at the wall	$[Jm^2s^{-1}]$

Latin Symbols

Symbol	Description	Units
Q	Factor used to visualize coherent structures	$[s^{-2}]$
q	Heat-flux	$[Jm^2s^{-1}]$
q_{diff}	Heat-flux due to turbulence diffusion	$[Jm^2s^{-1}]$
q_{res}	Heat-flux due to resolved fluctuations	$[Jm^2s^{-1}]$
R	Reynolds-stress	$[N/m^2]$
$R_{u_xu_x}$	Streamwise space-time correlation coefficient	[ ]
S_{ij}	Strain rate tensor	$[s^{-1}]$
t	Time	[s]
Δt	Time step	$[t]$
T	Temperature	$[K]$
$\tilde{T}$	Effective temperature	$[K]$
T_c	Flow over run time	$[s]$
u	Velocity	$[ms^{-1}]$
u_η	Kolgomorov velocity scale	$[ms^{-1}]$
u_0	Characteristic mean velocity	$[ms^{-1}]$
u'	Resolved velocity	$[ms^{-1}]$
u_τ	Viscous velocity	$[ms^{-1}]$
u_b	Bulk velocity	$[ms^{-1}]$
u_1	Streamwise velocity	$[ms^{-1}]$
U_c	Convection velocity of structures	$[ms^{-1}]$
W/D	Rod-wall gap size	[ ]
x	Spanwise direction	$[m]$
Δx	Grid spacing	$[m]$
y	Wall-normal direction	$[m]$
y^+	Wall units	[ ]
y_p	Distance between the wall and center of first cell next to it	$[m]$
z	Stream-wise direction	$[m]$

Greek Symbols

Symbol	Description	Units
α	Thermal diffusivity	$[m^2s^{-1}]$
γ	Model constant in LRR turbulence model	[ ]
δ	Channel half width	[m]
δ_{ij}	Kronecker delta	[ ]
δ_τ	Viscous length scale	$[m]$
ε	Turbulence dissipation rate	$[m^2s^{-3}]$

Greek Symbols

Symbol	Description	Units
ε_p	Turbulence dissipation rate at the first cell next to the wall	$[m^2 s^{-3}]$
η	Kolgomorov length scale	$[m]$
θ	Inter-channel tracer transfer rate	$[\%]$
θ	Dimensionless temperature difference	[ ]
κ	von Kármán constant	[ ]
λ	Streamwise spacing	$[m]$
μ	Dynamic viscosity	$[N.sm^{-2}]$
μ_t	Turbulence dynamic viscosity	$[N.sm^{-2}]$
ν	Kinematic viscosity	$[m^2 s^{-1}]$
ν_t	Turbulence kinematic viscosity	$[m^2 s^{-1}]$
ρ	Density	$[kg/m^3]$
σ_k	Model constant in $k-\varepsilon$ and LRR turbulence model	[ ]
σ_ε	Model constant in $k-\varepsilon$ and LRR turbulence model	[ ]
τ	Total shear-stress	$[N/m^2]$
τ_η	Kolgomorov time scale	$[s]$
τ_w	Wall shear-stress	$[N/m^2]$
Ω_{ij}	Rotation tensor	$[s^-1]$
ϑ^2	Variance of total temperature fluctuations	$[K^2]$

Abbreviations

Abbreviation	Description
ACGD	Advanced Gas Cooled Reactor
BWR	Boiling Water Reactor
CFD	Computational Fluid Dynamics
CFL	Courant-Friedrichs-Lewy condition
CHF	Critical Heat Flux
CST	Continuous Stirred Tanks
CV	Control-Volume
DIC	Diagonal Incomplete Cholesky
DNS	Direct Numerical Simulations
EARSM	Explicit Algebraic Reynolds Stress Model
LES	Large Eddy Simulations
LMFBR	Liquid Metal Fast Breeder Reactor
LRR	Launder Reece and Rodi Turbulence Model
NURETH	Nuclear Reactor Thermal-Hydraulics
PBiCG	Pre-conditioned Bi-Conjugate Gradient Solver

Abbreviations

Abbreviation	Description
PCG	Pre-conditioned Conjugate Gradient
PHWR	Pressurized Heavy Water Reactor
PISO	Pressure Implicit with Splitting of Operations
PWR	Pressurized Water Reactor
RANS	Reynolds Averaged Navier Stokes
RSM	Reynolds Stress Model
URANS	Unsteady Reynolds Averaged Navier Stokes

Dimensionless Groups

Group	Description
Pr	Prandlt number
Pr_t	Turbulent Prandlt number
Re	Reynold number
Re_0	Characteristic Reynolds number
Re_b	Bulk Reynolds number
Re_τ	Friction Reynolds number
St	Strouhal number

Contents

Chapter 1

Introduction

The flow in a simplified rod-channel geometry tries to emulate the coolant flow between the rod bundles inside a nuclear reactor. Given the high priority of safety in the operation of nuclear reactors, it is necessary to have a comprehensive understanding of the coolant flow behavior. The interesting geometry of the rod bundles, with the presence of wide and narrow regions results in a unique flow profile, with the presence of large-scale swirling structures. These structures are known to be coherent in nature and result in cross-flow zones in the otherwise axial flow in rod bundles.

1.1 Nuclear Energy and Reactors

With the dwindling conventional energy resources and slow development of renewable energy, nuclear power will continue to be in the world energy mix for years to come. There has been a steady growth in the world nuclear-fission reactor capacity over the past few decades, and it continues to grow. With more countries joining the league of developing countries, further development of nuclear fission energy is very important. Figure 1.1 shows the projected nuclear-fission generation capacity worldwide.

Figure 1.2 shows a schematic of the basic operation of a pressurized water nuclear reactor. Most of the nuclear reactors consist of cylindrical fuel rod assemblies, where controlled nuclear fission reactions take place. Large amount of heat is generated as a by-product of these fission reactions. In most of the nuclear reactors a coolant is used to remove the heat produced. In pressurized water reactors, the heated coolant is subsequently sent to a secondary loop, where steam is produced, and this steam is used to run turbines and generate electricity.

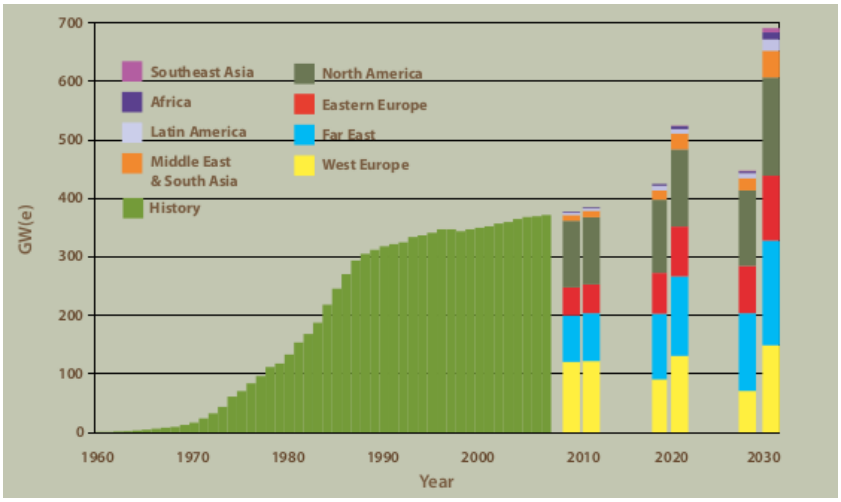

Figure 1.1: Projections of nuclear fission generation capacity, 2020-2030

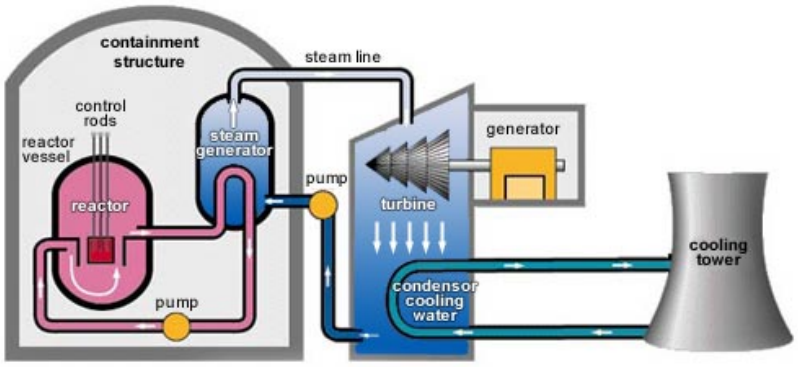

Figure 1.2: Schematic of a pressurized water nuclear reactor

1.2 Safety of Nuclear Reactors

Two of the biggest challenges in the development and widespread use of nuclear energy are operational safety and radioactive waste disposal. The Chernobyl disaster in 1986 and the more recent Fukushima disaster in 2011 are two of the well known nuclear accidents which have caused major apprehensions to the future of nuclear power. The Fukushima accident was caused due to the loss of power supply and cooling, hence leading to partial melting of the fuel rods.

The knowledge of flow and energy distribution inside the reactor is crucial given the high chances of coolant overheating or loss of coolant accident. This may lead to the Critical Heat Flux (CHF) phenomena. In this condition, there is a rapid increase in the wall temperature or rapid decrease in the heat flux, leading to very low heat transfer coefficients. This could lead to the departure from nucleate boiling (leading to vapor blanketing of the rod) or liquid film dry-out depending upon the vapor quality in the

core (Todreas and Kazimi [1993]). In other words, the heat produced due to the fission reactions is not removed and a build up of temperature takes place. Due to material limitations of the various components inside the reactor, this build-up could lead to initiation of cracks and other thermo-mechanical related failures. Hence, it becomes all the more important to be able to predict accurately the energy distributions inside the reactor.

1.3 Flow in Rod Bundles

The Boiling Water Reactors (BWR), Pressurized Water Reactors (PWR), Pressurized Heavy Water Reactors (PHWR), Liquid Metal Fast Breeder Reactors (LMFBR) and Advanced Gas Cooled Reactor (AGCR) all contain nuclear fuel rods. A schematic of a nuclear fuel rod element is shown in Figure 1.3. These fuel rod sub-assemblies are mainly characterized by their geometric layout (triagonal, hexagonal or square - shown in Fig 1.4) and rod spacing.

Figure 1.3: Schematic view of fuel rod element

Rod spacing is one of the main design characteristic of the fuel rod assemblies. The rod-rod spacing is defined as the pitch to diameter ratio (P/D), and the rod-wall spacing is defined by W/D ratio (shown in Fig 1.5). The spacing determines how tightly the fuel rods are packed in the assembly: lower the spacing, higher the number of rods in the

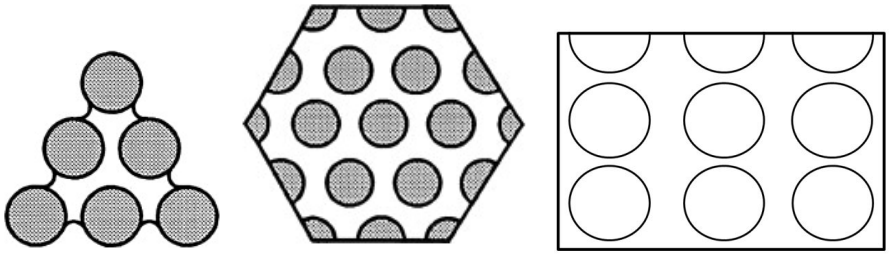

(a) (b) (c)

Figure 1.4: Geometric layout of fuel rod sub-assemblies: (a) Triangular, (b) Hexagonal and (c) Square

same cross-sectional area. In order to realize higher power-densities, conversion ratios and burn-up of reactors, the fuel rods have to be tightly packed.

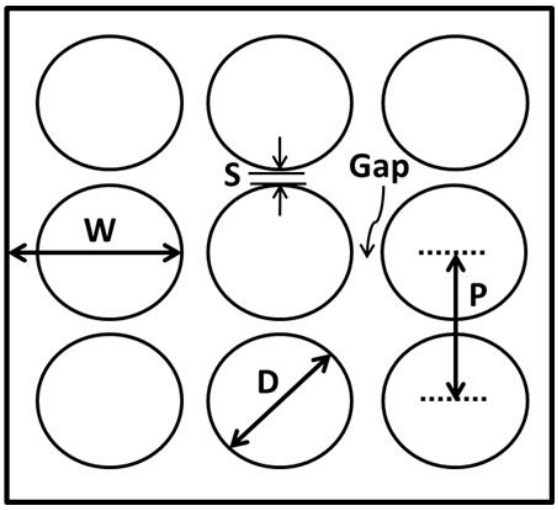

Figure 1.5: Gap spacing in a rod bundle

These tightly packed rod bundles are characterized by interesting flow patterns, different from the ones encountered in regular channel and pipe flows. The correct prediction and control of these flow distribution is essential for the reactor design and safety assessment, and has been an active area of research in reactor thermal-hydraulics. In fact, the well-known international conference on the nuclear reactor thermal-hydraulics (NURETH–13, NURETH–14) has a special session devoted to this phenomenon in rod bundles. Turbulent mixing is an important phenomena which influences the flow and temperature patterns in these rod bundles. Large-scale swirling coherent structures along with transverse flow pulsations have been identified in the rod-rod and rod-wall gap regions. These structures are quasi-periodic in nature and are considered an important factor for high mixing-rate. The enhanced mixing due to these structures helps in reducing the local temperature in the region, thereby reducing overheating and occur-

rence of CHF phenomena. Figure 1.6 shows a schematic of the transverse flow pulsations in rod bundles.

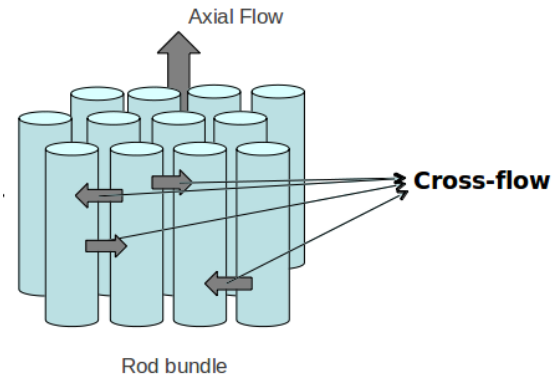

Figure 1.6: Schematic view of transverse flow pulsations in rod-bundles

The analysis of a full scale rod bundle is computationally very expensive, and experimental data is not available for validation of simulations. Hence the numerical simulations are done on a simplified geometry consisting of a cylindrical rod inside a rectangular channel. This geometry tries to emulate the gap region between a fuel rod and the pressure vessel wall inside the reactor. Detailed experimental and simulation results pertaining to the chosen configuration are reported in the literature. These will be used for benchmarking the results of the simulations.

1.4 Objectives

The following objectives were defined for the thesis:

1. Investigate the effect of different numerical approaches on the simulation results, and determine the most suitable approach. Validate the results of the most suitable approach with those of the experimental and simulation results reported in the literature. (Chapter 5)

2. Study the effect of the large-scale swirling coherent structures on the mean flow and investigate the dynamics of the coherent structures. (Chapter 6)

3. Study the effect of different geometrical configurations on the dynamics of the large-scale structures, and determine the configuration at which these structures are the most prevalent. (Chapter 6)

4. Analyze the transport and mixing of a passive scalar by the coherent structures and compare their contribution with that of turbulence. (Chapter 7)

The open source CFD solver, OpenFoam v2.0.1 is used for the simulations.

1.5 Thesis Outline

Chapter 2 deals with the background theory concerning the work. The conservation equations, turbulence and turbulence modeling are discussed. The underlying physics of the coherent structures; mechanism behind their formation and an overview of the previous work done is discussed in Chapter 3.The numerical schemes used in the thesis are discussed in Chapter 4. An introduction to OpenFOAM is given, followed by a description of the implementations done. The contents of the Chapters 5, 6 and 7 were already mentioned before. The conclusions and recommendations for future work are discussed in Chapter 8. The Appendix A covers the governing equations of the turbulence models used.

Chapter 2

Background Theory

The important physics relating to the work is summarized in this section. The Navier-Stokes equations are discussed, followed by an overview of turbulent flows. The various methodologies for turbulence modeling has been discussed, and the governing equations of the turbulence models used in this work are described.

2.1 Conservation Equations

The continuity equation for an incompressible fluid is given by

$$\frac{\partial u_i}{\partial x_i} = 0 \tag{2.1}$$

The momentum conservation is described by the Navier-Stokes equations. The equation for an incompressible Newtonian fluid is given by

$$\frac{\partial u_i}{\partial t} + u_j \frac{\partial u_i}{\partial x_j} = -\frac{1}{\rho}\frac{\partial p}{\partial x_i} + \nu \frac{\partial^2 u_i}{\partial {x_j}^2} \tag{2.2}$$

The conservation equation for a passive scalar T is described by

$$\frac{\partial T}{\partial t} + u_j \frac{\partial T}{\partial x_j} = \alpha \frac{\partial^2 T}{\partial {x_j}^2} \tag{2.3}$$

2.2 Overview of Turbulent Flows

Turbulent flows are unsteady and three dimensional in nature, with the presence of both small and large scale flow structures: eddies and vortical structures. One of the main advantage turbulence offers in industrial applications is enhanced mixing. Inside a nuclear reactor, it is important that the coolant is well mixed and the heat is distributed

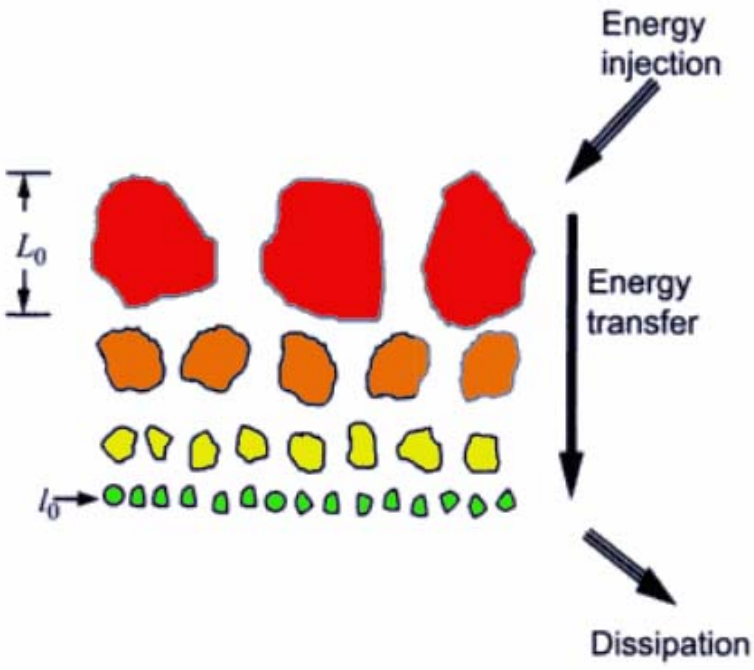

Figure 2.1: Cartoon of energy cascading process

evenly. The physics of turbulence can be explained by the energy cascade concept described first by Richardson in 1922 (Pope [2000]). The turbulence kinetic energy is produced at the largest scales, which are of the order of the mean flow. These large eddies are unstable and anisotropic, and break into smaller eddies leading to the phenomenon of an energy cascade from the largest to the smallest eddies. The smallest scales of turbulence (called the Kolgomorov scales) are stable and dissipative in nature. A cartoon of the energy cascade is shown in Fig. 2.1.

It is interesting to discuss in brief the length-scales of the largest and smallest eddies of turbulence. The production of turbulence kinetic energy occurs at the largest scales, which have a characteristic velocity u_0 and a characteristic length of the order of l_0, where u_0 is the mean velocity and l_0 is the length of the flow domain. Hence, the kinetic energy content and the time-scale of the largest scales can be expressed as u_0^2 and l_0/u_0 respectively. The production of turbulence kinetic energy, P_{l_0} will be proportional to u_0^3/l_0 and this is equal to the viscous dissipation at the smallest scales, expressed by ε. If ν is the kinematic viscosity of the fluid, then a simple dimensional analysis will lead to the Kolgomorov scales, η, u_η and τ_η are length, velocity and time scales respectively.

$$\eta = (\frac{\nu^3}{\varepsilon})^{1/4}, \quad u_\eta = (\varepsilon\nu)^{1/4}, \quad \tau_\eta = (\frac{\nu}{\varepsilon})^{1/2} \tag{2.4}$$

The ratio of the smallest scales to that of the mean flow are given by

$$\frac{\eta}{l_0} \simeq {Re_0}^{-3/4}, \quad \frac{u_\eta}{u_0} \simeq {Re_0}^{-1/4}, \quad \frac{\tau_\eta}{\tau_0} \simeq {Re_0}^{-1/2} \tag{2.5}$$

2.2.1 Reynolds Equations

In order to obtain an equation for the mean flow, Reynolds decomposition is applied to the Navier-Stokes equations. The vector and scalar fields are decomposed into a mean and a fluctuation component. The velocity field, for instance, is expressed as $u = u' + \overline{u}$, where u' is the fluctuation component and $\overline{u}$ is the mean component. This decomposition follows a set of rules, or the Reynolds conditions. If x and y are two fields and c is a constant, then the conditions are as follows

$$\overline{x+y} = \overline{x} + \overline{y} \tag{2.6}$$

$$\overline{cx} = c\overline{x} \tag{2.7}$$

$$\overline{\frac{\partial x}{\partial s}} = \frac{\partial \overline{x}}{\partial s} \tag{2.8}$$

$$\overline{\overline{x}y} = \overline{x}\overline{y} \tag{2.9}$$

Applying the Reynolds decomposition to the Navier-Stokes equations, the Reynolds Averaged Navier Stokes equations (RANS) are obtained. The RANS equations for continuity, momentum and scalar conservation are described by

$$\frac{\partial \overline{u_i}}{\partial x_i} = 0 \tag{2.10}$$

$$\rho\frac{\partial \overline{u_i}}{\partial t} + \overline{u_j}\frac{\partial \overline{u_i}}{\partial x_j} = -\frac{\partial \overline{p}}{\partial x_i} + \mu\frac{\partial^2 \overline{u_i}}{\partial {x_j}^2} - \rho\frac{\partial \overline{u_i' u_j'}}{\partial x_j} \tag{2.11}$$

$$\frac{\partial \overline{T}}{\partial t} + \overline{u_j}\frac{\partial \overline{T}}{\partial x_j} = \alpha\frac{\partial^2 \overline{T}}{\partial {x_j}^2} - \frac{\partial \overline{u_j' T'}}{\partial x_j} \tag{2.12}$$

The decomposition leads to additional terms in the momentum and scalar conservation equations. The $\rho\overline{u_i' u_j'}$ term is called the Reynolds-stress. The Reynolds equations are not closed due to the Reynolds-stress term; a closure is required in terms of known flow parameters.

2.2.2 Wall-Bounded Turbulent Flows

A brief overview of different terms used in wall flows is given. As the flow in rod bundles is affected by the gap region, the effect of the wall is probably quite important. For a fully developed channel flow, the total shear stress, τ, is the sum of viscous stress, $\rho\nu\frac{d\overline{u_i}}{dx_j}$, and Reynolds-stress $-\rho\overline{u_i'u_j'}$.

$$\tau = \rho\nu\frac{d\overline{u_i}}{dx_j} - \rho\overline{u_i'u_j'} \tag{2.13}$$

At the wall, $u_i = 0$, hence the Reynolds-stress goes to zero. Therefore the viscous stress is the only contribution to the wall shear-stress (τ_w), given by

$$\tau_w = \rho\nu\left(\frac{d\overline{u_i}}{dy}\right)_{y=0} \tag{2.14}$$

where u_i is the streamwise velocity and y the wall-normal direction. The viscous velocity scale, u_τ and length scale, δ_τ are defined as the following:

$$u_\tau = \sqrt{\frac{\tau_w}{\rho}} \quad \delta_\tau^+ = \frac{\nu}{u_\tau} \tag{2.15}$$

On basis of the above defined velocity and length scales, the friction Reynolds number Re_τ is defined as

$$Re_\tau = \frac{u_\tau\delta}{\nu} \tag{2.16}$$

where, δ is the half width of the channel. The distance from the wall is measured in terms of wall units, y^+. It is given by

$$y^+ = \frac{u_\tau y}{\nu} \tag{2.17}$$

Table 2.1, constructed from Pope [2000] shows the different wall regions defined on the basis of wall units and the corresponding property there, where $u_i^+ = \overline{u_i}/u_\tau$,

2.3 Prediction of Turbulence

In order to accurately predict turbulence, all the length and time scales have to be resolved, and the simulation technique which does this is called Direct Numerical Simulations (DNS). There is no modeling in DNS, all the scales are resolved and the Navier Stokes equations are solved. Following the discussion of turbulent length and time scales in Section 2.2, the number of computational mesh points required for a three dimensional

Table 2.1: Wall regions (Pope [2000])

Region	Location	Property
Inner layer	$y/\delta < 0.1$	$\overline{u_i}$ determined by u_τ and y^+, independent of bulk velocity and δ
Viscous wall region	$y^+ < 50$	Significant viscous contribution to total shear stress
Viscous sublayer	$y^+ < 5$	Reynolds shear-stress is negligible compared to viscous stress
Outer layer	$y^+ > 50$	Negligible effects of viscosity on mean flow
Overlap region	$y^+ > 50, y/\delta < 0.1$	Region of overlap between inner and outer layers
Log-law region	$y^+ > 30, y/\delta < 0.3$	$u_i^+ = f(ln(y^+))$
Buffer layer	$5 < y^+ < 30$	Transition region between viscosity dominated and inertia dominated parts

geometry scales as $Re^{9/4}$. Even for a very low Reynolds number of 1000, the number of mesh points required are of the order of 5.10^6. In the regime of turbulent flow in rod bundles, the Reynolds number is much higher (order of 10^5), and it is impossible to perform DNS, given the current available computational resources.

Another technique used for predicting turbulent flows is the Large-Eddy Simulation (LES). It is based on the concept that the smallest dissipative scales of turbulence are isotropic and easy to predict and the energy is mainly contained in the larger scales. Hence, the smallest scales are modeled using equations and the large scales are resolved explicitly. Although the number of computational mesh points required are less than DNS, it is still computationally very expensive.

Due to the high computational costs of both DNS and LES, the prediction of turbulence is done mainly by solving the Reynolds equations, and not the Navier Stokes equations. These are the Reynolds Averaged Navier Stokes (RANS) simulations. As discussed in the previous section, a closure for the additional Reynolds stresses, $\rho\overline{u_i'u_j'}$, $\rho\overline{u_j'u_k'}$, $\rho\overline{u_i'u_k'}$ etc. is required. A turbulence model is used for the closure, which represents these stresses in terms of known flow parameters. In practice, the RANS equations can be solved in two ways: 1) steady and 2) unsteady. In the steady RANS, the time dependent terms are not included, and it is useful for flows which do not contain any temporal dynamics. The unsteady RANS or URANS on the other hand solves the complete RANS equations including the time-dependent terms. In cases of wall resolved flows, the size of the mesh is very small close to the wall and therefore small time-steps of the order of $10^{-3} - 10^{-5}$ s is required. This makes URANS computationally expensive than steady-RANS, but still they remain less expensive than DNS and LES.

Among the three approaches discussed above for turbulence prediction, LES and DNS have proved to be most accurate in predicting flows in rod bundles. But, due to the high

Re number, the computational resources act as a barrier in applying these approaches for the more practical reactor flow conditions. As of now, they can be used only for simulating the flow in test geometries which operate at lower Re numbers. Whereas, the computationally cheaper URANS was able to predict the flows in such geometries fairly accurately. Chang and Tavoularis [2012] conducted LES on the geometry used in this work, and the time required for one set of simulations were of the order three months. Hence considering all these factors, URANS methodology is used in this thesis. In view of this, LES and DNS techniques are not discussed further. A general description of the different types of RANS turbulence models is given.

2.3.1 Turbulence Models

There exist different approaches to obtain a closure relationship for the Reynolds stresses. They can be roughly divided into the following three types

1. based on the linear eddy-viscosity hypothesis
2. based on the non-linear eddy-viscosity hypothesis
3. solving equations for each Reynolds stress

The turbulence models of the first and third types are used in this thesis and discussed below.

Models Based on Linear Eddy-Viscosity Hypothesis

In the Boussinesq or the eddy-viscosity hypothesis, the Reynolds-stresses are expressed as a product of a turbulence viscosity and the strain rate. For an incompressible flow the formulation is as follows:

$$\rho\overline{u_i'u_j'} = -\mu_t\left(\frac{\partial\overline{u_i}}{\partial x_j} + \frac{\partial\overline{u_j}}{\partial x_i}\right) \tag{2.18}$$

A closure relationship is required for the turbulence viscosity, μ_t. Most of the simulations carried out in this thesis are based on the $k-\varepsilon$ model. This is a form of a two-equation model in which transport equations are solved for two turbulence quantities: the turbulence kinetic energy, k and the turbulence dissipation rate, ε. The equations for k and ε are as follows:

$$\frac{Dk}{Dt} = \frac{\partial}{\partial x_j}\left[(\nu + \frac{\nu_t}{\sigma_k})\frac{\partial k}{\partial x_j}\right] + P_k - \varepsilon \tag{2.19}$$

$$\frac{D\varepsilon}{Dt} = \frac{\partial}{\partial x_j}\left[(\nu + \frac{\nu_t}{\sigma_\varepsilon})\frac{\partial \varepsilon}{\partial x_j}\right] + C_{\varepsilon 1}\frac{\varepsilon}{k}P_k - C_{\varepsilon 2}\frac{\varepsilon^2}{k} \tag{2.20}$$

The turbulence viscosity is expressed as

$$\nu_t = C_\mu \frac{k^2}{\varepsilon} \tag{2.21}$$

The standard model coefficients are as expressed in Table 2.2.

Table 2.2: Model coefficients for standard $k-\varepsilon$ turbulence model (Pope [2000])

Coefficient	Value
P_k	$\nu_t S^2$
S	$\sqrt{2\overline{S_{ij}}\overline{S_{ji}}}$
S_{ij}	$0.5\left[\frac{\partial \overline{u_i}}{\partial x_j} + \frac{\partial \overline{u_j}}{\partial x_i}\right]$
$C_{\varepsilon 1}$	1.44
$C_{\varepsilon 2}$	1.92
C_μ	0.09
σ_k	1
σ_ε	1.3

The eddy-viscosity hypothesis is also applied for the closure of $\overline{u_j' T'}$ term in Equation 2.12

$$-\overline{u_j' T'} = \frac{\nu_t}{Pr_t}\frac{\partial T}{\partial x_j} \tag{2.22}$$

where Pr_t is the turbulent Prandlt number and it is taken as 0.85, following the simulations of Chang and Tavoularis [2006].

Reynolds-Stress Models

Reynolds stress models (RSM) are the other major class of RANS turbulence models. In these models, transport equations are solved separately for each of the six Reynolds-stresses; usually, considered superior than the models based on the Boussinesq hypothesis(Wilcox [1993]). The *LRR* (Launder, Reece and Rodi) turbulence model proposed by Launder et al. [1975] is used here. The transport equations are solved for the Reynolds stresses and turbulence dissipation rate, ε. This leads to five additional equations compared to the $k-\varepsilon$ model, hence making it computationally expensive. The model equations for the RSM are

$$\begin{aligned}\frac{D\overline{u_i'u_j'}}{Dt} &= -\left[\overline{u_j'u_k'}\frac{\partial\overline{u_i}}{\partial x_k} + \overline{u_i'u_k'}\frac{\partial\overline{u_j}}{\partial x_k}\right] - \frac{2}{3}\delta_{ij}\varepsilon \\ &- C_{\varepsilon 1}\frac{\varepsilon}{k}(\overline{u_i'u_j'} - \frac{2}{3}\delta_{ij}k) + (\phi_{ij}+\phi_{ji})_2 + (\phi_{ij}+\phi_{ji})_w \\ &+ C_s\frac{\partial}{\partial x_k}\frac{k}{\varepsilon}\left[\overline{u_i'u_l'}\frac{\partial\overline{u_j'u_k'}}{\partial x_l} + \overline{u_j'u_l'}\frac{\partial\overline{u_k'u_i'}}{\partial x_l} + \overline{u_k'u_l'}\frac{\partial\overline{u_i'u_j'}}{\partial x_l}\right] \end{aligned} \tag{2.23}$$

$$\frac{D\varepsilon}{Dt} = C_\varepsilon\frac{\partial}{\partial x_k}\left(\frac{k}{\varepsilon}\overline{u_k'u_l'}\frac{\partial\varepsilon}{\partial x_l}\right) - C_{\varepsilon 1}\frac{\varepsilon\overline{u_i'u_k'}}{k}\frac{\partial\overline{u_i}}{\partial x_k} - C_{\varepsilon 2}\frac{\varepsilon^2}{k} \tag{2.24}$$

The model coefficients are given in Table 2.3.

Table 2.3: Model coefficients for LRR turbulence model (Launder et al. [1975])

Coefficient	Value
$(\phi_{ij}+\phi_{ji})_w$	$\left[0.125\frac{\epsilon}{k}(\overline{u_i'u_j'} - \frac{2}{3}k\delta_{ij}) + 0.015(P_{ij}-D_{ij})\right]\left(\frac{k^{1.5}}{\varepsilon x_2}\right)$
$(\phi_{ij}+\phi_{ji})_2$	$\gamma(P_{ij} - \frac{2}{3}P\delta_{ij})$
P_{ij}	$\overline{u_i'u_k'}\frac{\partial\overline{u_j}}{\partial x_k} + \overline{u_j'u_k'}\frac{\partial\overline{u_i}}{\partial x_k}$
D_{ij}	$\overline{u_i'u_k'}\frac{\partial\overline{u_k}}{\partial x_j} + \overline{u_j'u_k'}\frac{\partial\overline{u_k}}{\partial x_i}$
P	$-2\overline{u_i'u_j'}\frac{\partial U_i}{\partial x_j}$
C_ε	0.15
C_s	0.25
$C_{\varepsilon 1}$	1.44
$C_{\varepsilon 2}$	1.92
σ_k	1
σ_ε	1.3
γ	0.6
x_2	Normal distance of the cell to the surface

2.3.2 Treatment Near the Walls

Due to the sharp gradients of different flow parameters near the wall-region, special attention needs to paid to its modeling. The two approaches are: 1) using wall functions or 2) resolving the flow in the near wall region by including more grid points and using damping functions. The schematic of the computational mesh for both the cases is shown in Figure 2.2.

(a) (b)

Figure 2.2: Schematic of the mesh in the near the wall region for (a) Wall function approach and (b) Resolving the flow in the near wall region (not to scale)

Wall Functions

The wall functions are applied as boundary conditions in the log-law region (discussed in Section 2.2.2), hence working on the assumption that the region close to the wall can be approximated to a turbulent boundary layer. The log-law, at $y^+ > 30$, takes the form

$$\overline{u_i} = u_\tau \left[\frac{1}{\kappa} ln(y^+) + B \right] \tag{2.25}$$

Here u_τ and y^+ follow the definitions in Section 2.2.2, κ is the von Kármán constant with a value of 0.41, and $B = 5.2$ is a constant.

Following the derivation found in Pope [2000], the boundary condition for the turbulence kinetic energy becomes

$$k_p = {C_\mu}^{(-1/2)} {u_\tau}^2 \tag{2.26}$$

here index p denotes the first cell next to the wall.

The turbulence dissipation rate boundary condition is

$$\varepsilon_p = \frac{{u_\tau}^3}{\kappa y_p} \tag{2.27}$$

It is to be noted that in order to use wall functions, the first cell should be located at a distance $30 < y^+ < 100$ for the log-law approximation to be accurate.

Near-Wall Turbulence Models

Although the wall functions are computationally cheap and attractive, they fail to work in cases of strong pressure gradients or impinging flows. In such cases, more number of cells are included close to the wall and the transport equations for the turbulence quantities are modified using damping functions. The first computational cell must be located at a distance $y^+ < 1$. These models are also called low-Re turbulence models. Three different low-Reynolds number variants of the $k-\varepsilon$ model were available in OpenFOAM and are used in the present work. They are based on the following references:

- Lam and Bremhorst [1981]
- Launder and Sharma [1974]
- Lien and Leshziner [1995]

The governing equations of these models are given in Appendix A.

Chapter 3

Flow in Rod Bundles

The axial flow in tight-lattice rod bundle geometries are known to contain large-scale swirling structures. The characteristics of these structures, i.e., the length scale (wavelength) and time scale (frequency) depend parameters such as the gap spacing (P/D and W/D ratio) and Re number. These structures are also known to cause high cross-flow mixing, leading to uniform enthalpy distribution in the rod bundles. In this chapter, the underlying physics of coherent structures is discussed.

Firstly, a brief introduction to the two mechanisms (Kelvin-Helmholtz instability and secondary flows) commonly associated with the formation of the large-scale coherent structures is given. This is followed by an overview of the past experimental and numerical studies carried out, pertaining to the flows in rod-bundles. Based on these, specific objectives are defined for the thesis.

3.1 Kelvin-Helmholtz Instability

One of the mechanisms associated with the formation of the large-scale structures is the Kelvin-Helmholtz instability. The Kelvin-Helmholtz instability describes the production of a vortex sheet at the interface of two parallel horizontal streams having different velocities or densities (Kundu and Cohen [2002]). The sharp shear layer at the interface leads to vortical structures. A linear stability analysis of a simple inviscid fluid with a pattern shown in Figure 3.1a always leads to an unstable mode if $U_1 \neq U_2$(Kundu and Cohen [2002]). This leads to a vortex sheet similar to the one shown in Figure 3.1b. Such patterns are very common in the atmosphere in the form of clouds and also in oceans.

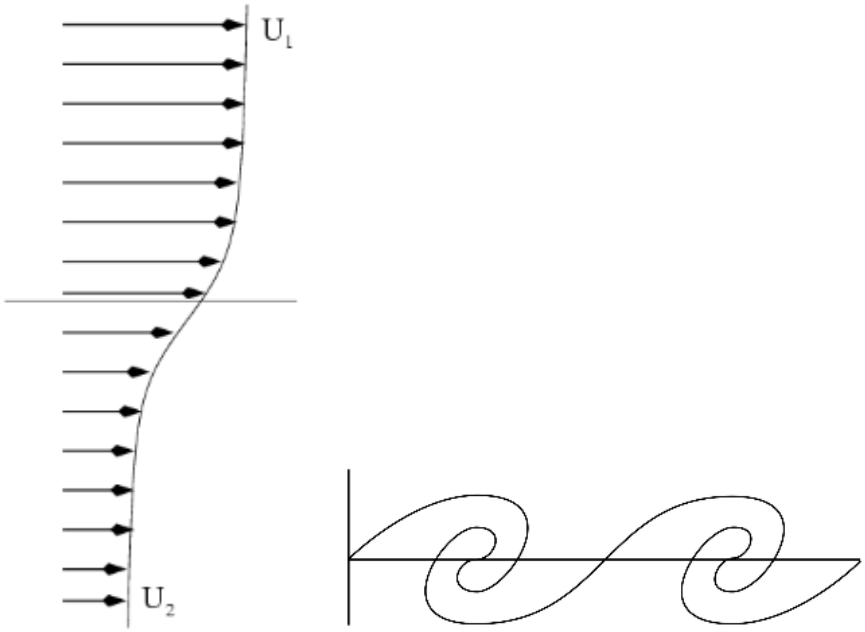

(a) (b)

Figure 3.1: (a) Shear layer - Kelvin Helmholtz Instability; (b) Schematic view of a vortex sheet due to the Kelvin Helmholtz Instability

3.2 Secondary Flows

Another mechanism used to explain the presence of the structures is secondary flow. In a fully developed turbulent channel-flow, the anisotropy of Reynolds-stresses lead to additional flow patterns in the normal plane to the bulk streamwise flow. This mean flow pattern is called secondary flow, a schematic of which is shown in Figure 3.2. Secondary flow are of the order of 1-2 % of the mean bulk flow, and can cause enhancements in heat or scalar transport (Belt [2007]).

3.3 Flow in Rod Bundles

Meyer [2010] has given a comprehensive review of both experimental and numerical work done on the prediction of large-scale swirling structures in rod-bundle flows. The experimental studies have observed that the momentum transfer and the eddy-diffusivity's for such flows were strongly anisotropic. In the 1970s-1980s, there was a consensus that secondary flows were responsible for high transfer rates in the gap regions. But, with further experiments and simulations it was concluded that they contribute only to a small extent (1-2 %). The mechanism causing such flows was explained with the help of a new kind of instability for a fluid similar to the one present in the mixing layer

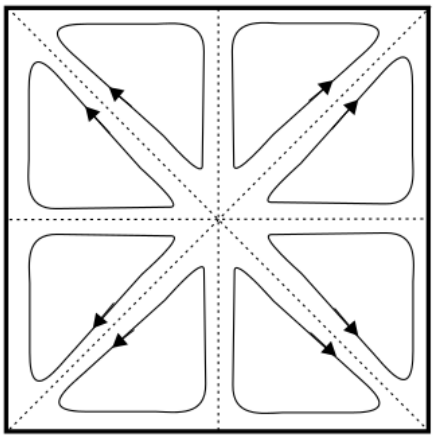

Figure 3.2: Secondary flow in cross-section of a channel flow

between the high-speed flow in the open core and low-speed flow in the gap region. The formation of quasi-periodic vortices were attributed to the Kelvin-Helmholtz instability mechanism.

Most of the results cited by Meyer [2010] conclude that the gap-spacing (P/D or W/D) is the most important parameter affecting the flow structure, decreasing which would lead to higher turbulence intensities. In terms of the computational work done, the review concludes that the flow characteristics can be only captured by Direct Numerical Simulations (DNS) or Large Eddy Simulations (LES), or by using anisotropic Unsteady Reynolds averaged Navier Stokes (URANS) modeling.

The low velocity in the narrow gap region and the high velocity in the sub-channels results in a shear-layer pattern (shown in Figure 3.3). In addition to the presence of the shear-layer, the flow in the channel is highly turbulent in nature. Gosset and Tavoularis [2006] were the first to observe coherent structures in laminar flow using an experimental geometry similar to the one in Figure 3.5b. They observed that the span-wise velocity profile is similar to the low-speed streaks observed in boundary layers, which have a wake-like profile and not an inflectional profile observed in Kelvin-Helmholtz type mixing layer instability. They cite similarities to the von Kármán vortex street which is formed in a wake region behind a cylinder.

Linear stability analysis of laminar Pouseille flow in an eccentric annulus was carried out by Merzari et al. [2008] and they confirm the presence of an additional instability mechanism, compared to that observed in pipe and channel flows. Similar analysis by Piot and Tavoularis [2011] observes two inflectional points on either side of the gap, indicating the Kelvin-Helmholtz type of instability. A comparison is also made to the study by Gosset and Tavoularis [2006] and differences in the geometry has been cited as the reason of different instability mechanisms. The high stability of the vortical structures is reported by Meyer [2010]. This is generally not the case in the typical

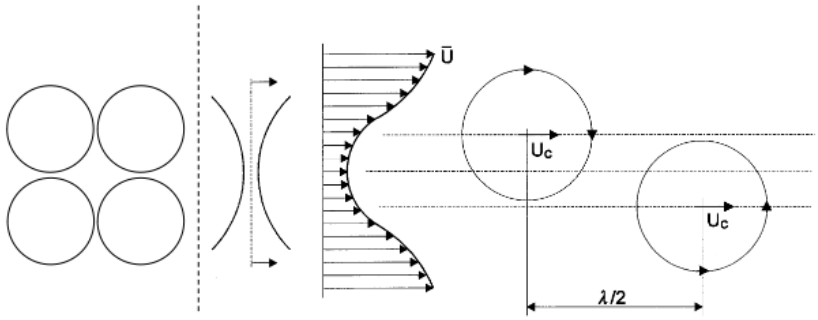

Figure 3.3: Schematic view of a shear layer pattern in rod bundles (Krauss and Meyer [1998])

instability mechanisms, where there is both a growth and destruction of structures.

Figure 3.4 shows the schematic of the structures and cross flow (Derksen [2010]). They are a set of counter-rotating vortices moving with the flow, and generate span-wise or cross-flow regions at their interface.

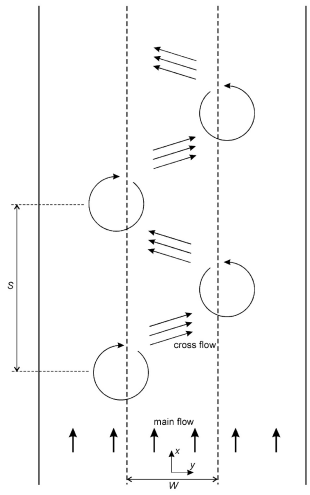

Figure 3.4: Schematic view of cross-flow

An overview of the different experimental and numerical studies carried out for the investigation of flows in rod bundles are discussed further.

3.3.1 Experimental Studies

Due to the difficulties in emulating the complex rod bundle geometry, many simpler geometries have been used for experiments. Most of the numerical works try to benchmark the experiments done by Meyer and Rehme [1994], Krauss and Meyer [1996, 1998] and Guellouz and Tavoularis [2000a,b]. The geometries used by them are shown in Figure 3.5. The summary of the experimental conditions are listed in Table 3.1, where Re_b,

U_b and D_h refer to the bulk Reynolds number, bulk velocity and hydraulic diameter respectively. Air was used as the working fluid in all these experiments.

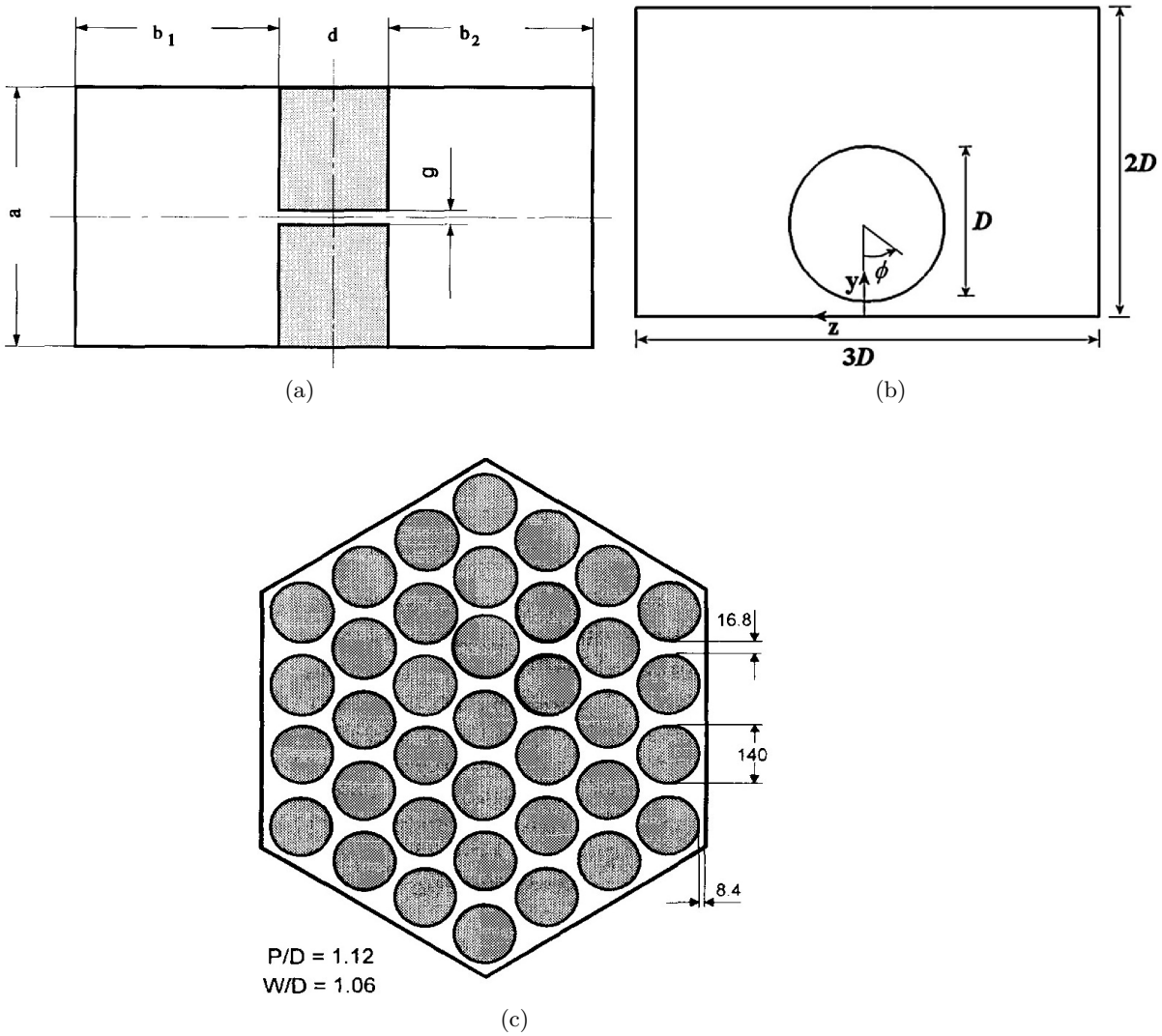

Figure 3.5: Experimental geometries: (a) Meyer & Rehme [1994]; (b) Guellouz & Tavoularis [2000a,b]; (c) Krauss & Meyer [1996, 1998]

Table 3.1: Details of benchmark experiments

Reference	P/D	Re_b	$U_b(ms^{-1})$	$D_h(mm)$
Meyer and Rehme [1994]	1.06 - 1.30	250000	20	180
Krauss and Meyer [1996,1998]	1.12 (P/D), 1.06 (W/D)	38574-64590	20	33-55
Guellouz and Tavoularis [2000a,b]	1.10 (W/D)	108000	10.1	160.6

Meyer and Rehme [1994] did measurements in 18 different geometries, corresponding to different values of a, b_1, b_2, d and g in Figure 3.5a. They observed high turbulence intensities and Reynolds shear-stresses very close to the gap, and this was attributed to the presence of strong large-scale quasi-periodic flow oscillations. The frequency of these structures depended only on the gap size.

Krauss and Meyer [1996, 1998] conducted measurements of a heated rod bundle, and observed large values of the intensities of temperature fluctuations, with the maximum in the gap region. Also, very high anisotropy of both momentum and heat transport was observed, which increased at lower P/D ratios. The spectral analysis of velocity and temperature fluctuations showed characteristic frequencies of the fluctuations in the gaps, hence attributing the high momentum and heat transport in such channels to periodic structures.

Guellouz and Tavoularis [2000a,b] also observed these large scale quasi-periodic structures, and obtained a correlation of the convection speed and streamwise spacing of them as a function of the gap width. Mahmood [2011] in his Ph.D. thesis conducted extensive experiments to characterize these flow patterns in compound channels (Figures 3.6a and 3.6b) as well as in tube bundle geometries (Figure 3.6c).

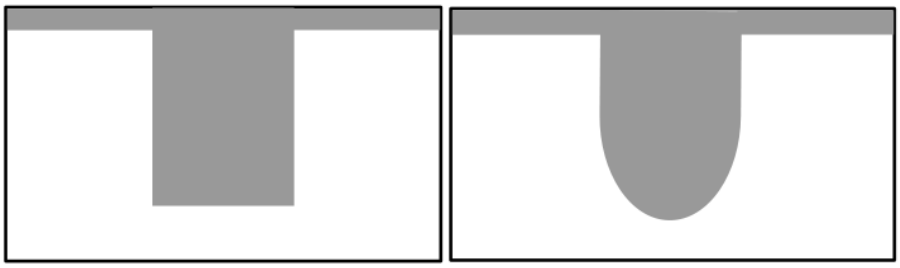

(a) (b)

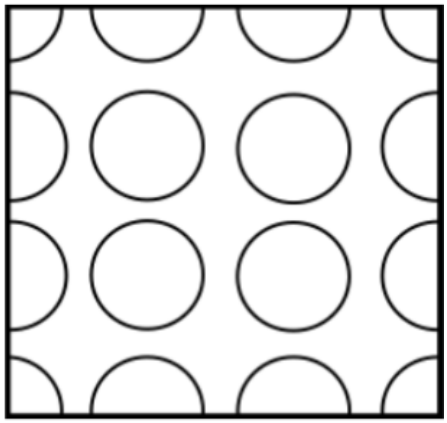

(c)

Figure 3.6: Experimental geometries investigated by Mahmood [2011]: (a) and (b) Compound channels; (c) Rod bundle

He tried to quantify the the total cross-flow mixing as a sum of contributions from the coherent structures and turbulent mixing (Figure 3.7). θ^{exp} represents the inter-channel tracer transfer, S the gap spacing and D_h^{gap} is the hydraulic diameter of the gap. It can be clearly seen that the effect of coherent structures on mixing fades away above a gap size of 9 mm.

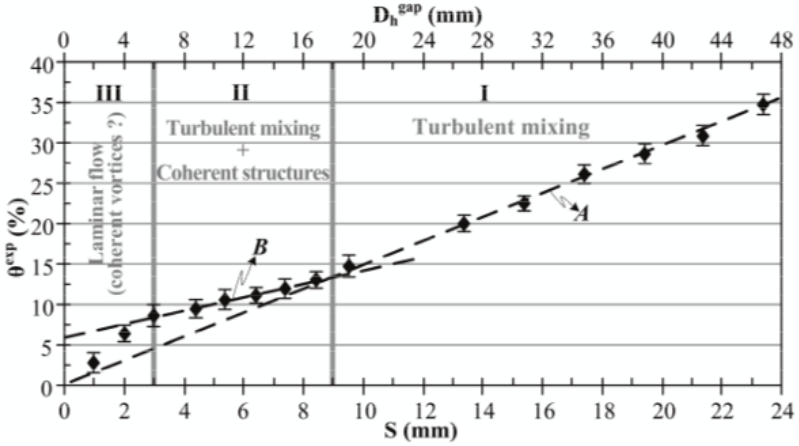

Figure 3.7: Mixing as a function of gap spacing

In order to correlate the inter-channel cross-flow mixing as a function of gap spacing, velocity of the coherent structures and other flow parameters, Mahmood [2011] developed a mixing-model. This was based on the transport of a passive scalar via the coherent structures represented as continuously stirred tanks (CST). The model was able to predict the total cross-flow mixing fairly accurately, however for turbulent flow in the gap region, it under-predicted the turbulent mixing.

3.3.2 Numerical Studies

A host of numerical techniques have been used to understand the characteristics of rod-bundle flows. Among all, LES (Merzari and Ninokata [2008, 2009], Ikeno and Kajishima [2010], Merzari and Ninokata [2011], Chang and Tavoularis [2012]) yields the most accurate results when compared to the experiments. In spite of its high accuracy, the requirements of high spatial resolution and computing power limits its use to few research groups around the world. Hence, the widely used steady RANS (Tóth and Aszódi [2010]) and URANS techniques (Yan and Yu [2011], Liu and Ishiwatari [2011], Yu et al. [2011], Chang and Tavoularis [2012], Yan et al. [2012a,b]) continues to be the most popular. Some of the major conclusions obtained from the numerical simulations reported in the literature are:

- There is negligible effect (∼1-2 %) of secondary flows on the high mixing rates.

- High values of velocity fluctuations and Reynolds shear-stresses are observed in region close to the gap. This is attributed to the presence of large-scale velocity fluctuations or quasi-periodic structures.

- The temporal characteristics and intensity of the coherent structures depend on the Re number and the gap spacing (P/D or W/D). The intensity is found to be directly proportional to the Re number and inversely proportional to the gap spacing.

- High anisotropy of momentum and heat transport is observed at lower gap sizes.

- There exists a critical gap size (P/D $\sim$ 1.03) at which the cross-flow mixing is the strongest.

- The LES techniques is the most accurate in predicting the flow structures, although URANS simulations also yielded reasonable estimates.

3.4 Specific Objectives

The different URANS turbulence models were discussed in Section 2.3.1. There exist significant differences in the computational costs between an eddy-viscosity based and Reynolds-stress based models, and that between different wall-treatment approaches. A study to analyze the effect of these different approaches in predicting the flow characteristics will help in obtaining a reasonable balance of accuracy and computational cost.

There is no clear consensus on the precise mechanism behind the formation of these structures. Some of the mechanisms popularly reported are: (1) Kelvin-Helmholtz instability, (2) instability associated with the wake-region of a flow across a cylinder, (3) similar to the structures formed during the laminar to turbulence transition and (4) association with the turbulence structures formed in the near wall region in a fully developed turbulent flow. An attempt will be made to shed further insights into the possible mechanism for the formation of the structures.

Very little information on the three-dimensional nature of these structures has been reported. The only parameter used in the literature to describe them is the streamwise spacing, which is a one-dimensional description. No attempt has been made to analyze the extent of these structures away from the gap region. Hence, it will be interesting to study the global structure of these fluctuations. The effect of gap size on the coherent structures have been widely discussed in the literature. Only a few works in the literature try to quantify the contribution of coherent structures towards total scalar transport and mixing.

Therefore, based on the past work carried out, specific objectives are defined for this work:

- Study the effect of the turbulence model on the dynamics of flow in the experimental geometry of Guellouz and Tavoularis [2000a,b]. Compare the results by using different wall treatment and the type of URANS model.
- Determine the length of periodic domain sufficient to resolve the temporal scales of the the flow accurately. The length should be long enough such that the periodicity of the flow domain has no effect on the dynamics of the flow.
- Validate the results of the simulations using the experimental results of Guellouz and Tavoularis [2000a,b] and the simulations of Chang and Tavoularis [2005, 2006, 2008, 2012].
- Analyze the effect of the large-scale swirling structures on the time-averaged velocity, their fluctuations and turbulence kinetic energy.
- Investigate the extent of the structures via flow-visualization of streamlines and determine the specific length, time and velocity scales of the fluctuations.
- Study the effect of gap size on the coherent structures, and determine the critical gap size at which the structures are the most dominant.
- Analyze the cross-flow mixing by including passive scalar, and quantify the contributions of turbulence and coherent structures.

Chapter 4

Numerical Techniques

In this chapter, an overview of the various numerical techniques used is given. An introduction to OpenFOAM and its features is highlighted. This is followed by the code implementation done for the passive scalar equation and related boundary conditions. The details of the discretization procedures, solvers used, convergence criterion and other settings are also mentioned.

4.1 OpenFOAM

OpenFOAM is an acronym for Open Source Field Operation and Manipulation. It is an object oriented C++ library used for CFD applications. OpenFOAM uses the finite volume method for computing the flow field. This method solves the integral form of the conservation equations. The flow domain is divided into a number of finite control volumes, and the discretized differential equations are solved over these volumes. OpenFOAM also includes utilities for pre and post-processing steps. Figure 4.1 gives an overview of the structure of OpenFOAM (OpenFOAM Documentation).

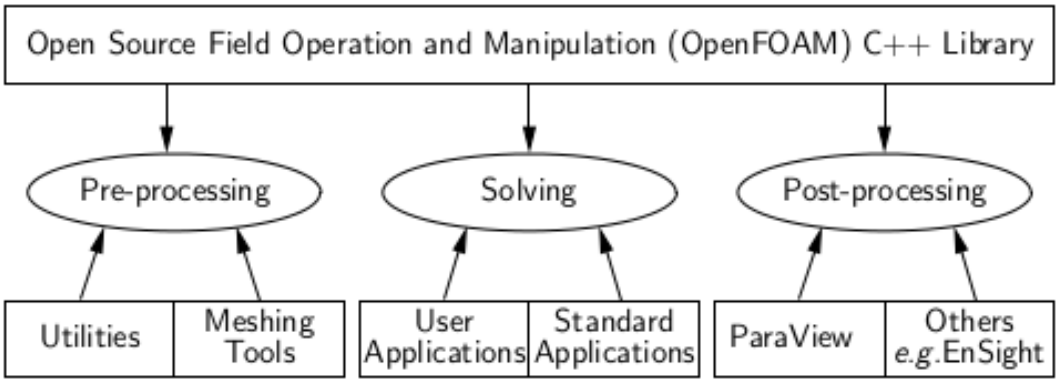

Figure 4.1: Structure of OpenFOAM (OpenFOAM Documentation)

OpenFOAM consists of a number of dynamically linked pre-compiled applications. It also gives users freedom to create new applications or modify the previous applications according to their specific needs. The two main categories of applications are:

- Solvers - algorithms for solving the partial differential equations arising in different problems, e.g., steady and unsteady incompressible flows, turbulent flows, flows with heat transfer, compressible flows, etc.
- Utilities - used for data manipulation, algebraic calculations and various pre- and post-processing steps, e.g., modifying the mesh, calculating averages of fields, etc

The OpenFOAM version 2.0.1 is used for simulations in this work. The PISO (Pressure Implicit with Splitting of Operators) algorithm is used for solving the unsteady Navier-Stokes and continuity equations. The algorithm is shown in Figure 4.2.

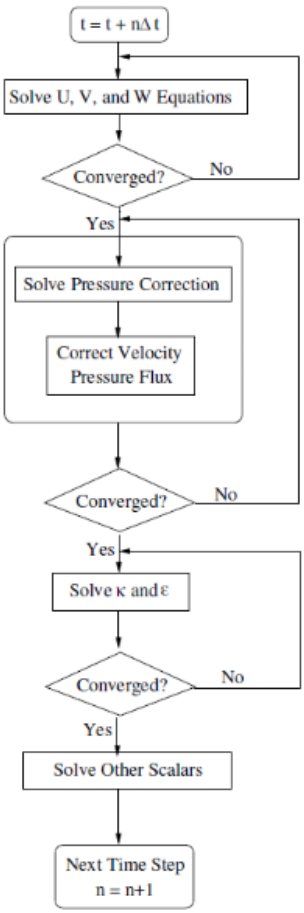

Figure 4.2: PISO algorithm

The open source pre-processing software SALOME v.6.4.0 was used for constructing the CAD geometry and computational mesh. The constructed 3D mesh was imported

into OpenFOAM as a .unv format, and was subsequently converted into the standard OpenFOAM format by using the already present pre-processing utilities in OpenFOAM.

4.2 Computational Procedures

4.2.1 Discretization, Solvers and Preconditioners

The discretization scheme for the various terms is listed in Table 4.1.

Table 4.1: Discretization schemes

Term	Scheme
$\partial/\partial t$	Second-order implicit
$\nabla(X)$	Linear interpolation Central differencing
$\nabla.(\rho UU)$	First order Upwind differencing
$\nabla.(\rho Uk)$	First order Upwind differencing
$\nabla.(\rho U\varepsilon)$	First order Upwind differencing
$\nabla.(\rho UR)$	First order Upwind differencing
$\nabla.(R)$	Second order Central differencing
$\nabla.(\nu_{eff}(\nabla(U)+\nabla(U)^T))$	First order Upwind differencing
$\nabla.(\rho UT)$	Second order Upwind differencing
$\nabla.(X\nabla Y)$	Unbounded second order explicit

where R is the Reynolds-stress tensor. X and Y refers to all the corresponding fields which occur in the various equations. The preconditioned bi-conjugate gradient solver (PBiCG) is used for the velocity fields and the turbulence quantities. The asymmetric diagonal incomplete LU preconditioner is used for the solver. For the pressure, preconditioned conjugate gradient (PCG) solver, along with the symmetric diagonal incomplete-cholesky (DIC) is used. The choices for solvers and discretization schemes were made on basis of the various OpenFOAM tutorials on turbulent flows.

4.2.2 Convergence Criterion

Table 4.2 shows the convergence criterion set for various quantities. No significant differences were observed in the results when changing the criterion from 10^5 to 10^6.

Table 4.2: Convergence criterion

Quantity	Convergence criterion
p	10^6
U	10^5
k	10^6
ϵ	10^6
R	10^6
T	10^5

4.2.3 Courant Number and CPU Time

As all the simulations were unsteady, the time step was chosen pertaining to the Courant-Friedrichs-Lewy (CFL) condition, which is defined as

$$CFL_{max} = \frac{U_{max}\Delta t}{\Delta x_{min}} < 1 \tag{4.1}$$

where, U_{max} represents the maximum velocity corresponding to the smallest cell with a grid spacing Δx_{min}. Δt is the time step used for simulations, and it is kept constant throughout. All the simulations were run in parallel. Table 4.3 shows the time step, maximum CFL number, number of processors used and the CPU time per time step for each of the simulations.

Table 4.3: Details of simulations

Simulations	Time Step Δt(s)	CFL_{max}	Processors	Wall clock time per Δt(s)
Standard $k-\varepsilon$ model	5.10^{-4}	0.62	4	12
High Re based LRR model	5.10^{-4}	0.8	4	35
Launder-Sharma low Re $k-\varepsilon$	1.10^{-5}	0.1	48	5
Lam-Bremhorst low Re $k-\varepsilon$	$2.5.10^{-5}$	0.05	48	5
Lien-Leschziner low Re $k-\varepsilon$	$2.5.10^{-5}$	0.1	48	6
Standard $k-\varepsilon$ with passive scalar	5.10^{-4}	0.64	8	9

4.2.4 Boundary Conditions

Periodic boundary conditions are applied for U, k, ε and T (except case of developing passive scalar field simulations in Section 7.3) in the streamwise direction. At the walls, No-slip boundary condition is used for velocity, $U = 0$ and zero-gradient for the pressure correction. The wall boundary conditions for k and ε are discussed in Section 4.3.

Periodic Flow Field

Generally, two approaches can used to enforce periodicity of the flow: (1) splitting the pressure field into a periodic and non-periodic part, and adding the constant pressure gradient as a source term in the momentum equation or (2) adjusting the pressure in the channel such that a constant inlet flow rate is maintained.

The second approach is applied in the current work, using the boundary condition (directMapped) which is available in OpenFOAM. Zero-gradient boundary condition is used for the pressure correction, which automatically adjusts itself in order to maintain a constant inlet velocity of $U_{bulk} = 10$ m/s.

Periodic Passive Scalar Field

For the passive scalar temperature field, simulations are done using two different wall boundary conditions: (1) constant temperature and (2) constant heat flux. In the first case, the periodic boundary conditions are applied simply by matching the temperature values at the outlet and inlet. Whereas for the second case with constant heat flux at the walls, the effect of the heat flux source has to be accounted for in the energy equation. In order to do that, an effective temperature $\tilde{T}$ is defined as

$$\tilde{T} = T(z) - \frac{dT_{bulk}}{dz} \tag{4.2}$$

where z is the streamwise direction. The expression for the term, dT_{bulk}/dz is obtained by performing an energy balance over an arbitrary control volume with an area of cross-section, A_c and wetted perimeter, P_w. If the heat flux at the wall is given by q_w, the energy balance leads to

$$\rho C_p dT_{bulk} A_c L_z U_{bulk} = q_w P_w L_z dz \tag{4.3}$$

where L_z is the streamwise length of the periodic domain. From this, the dT_{bulk}/dz term can be obtained as

$$\frac{dT_{bulk}}{dz} = \frac{q_w P_w}{\rho A_c U_{bulk} C_p} \tag{4.4}$$

The hydraulic diameter of the cross-section can be defined as, $D_h = 4A_c/P_w$. An equation for the effective temperature $\tilde{T}$ is obtained by substituting $T(z)$ in terms of $\tilde{T}$ and the temperature gradient in Equation 2.12.

$$\frac{\partial \tilde{T}}{\partial t} + \overline{u_j}\frac{\partial \tilde{T}}{\partial x_j} = \alpha \frac{\partial^2 \tilde{T}}{\partial {x_j}^2} - \frac{\partial \overline{u_j' \tilde{T}'}}{\partial x_j} - \frac{4q_w}{\rho D_h U_{bulk} C_p} \tag{4.5}$$

This modified equation along with the boundary condition (Equation 4.6) is implemented in OpenFOAM.

$$T_{inlet} = T_{outlet} - \frac{4q_w}{\rho D_h U_{bulk} C_p} L_z \tag{4.6}$$

4.3 Turbulence Models

OpenFOAM consists of a wide range of RANS turbulence models. They include linear and non-linear eddy viscosity models, Reynolds-stress and low-Re (using damping functions near the wall) turbulence models. The wall boundary conditions for k and ε for the different turbulence models are listed in Table 4.4.

Table 4.4: Wall boundary conditions of k and ε

Turbulence model	k	ε
High Re turbulence models: $k-\varepsilon$ and LRR	Wall-functions	Wall-functions
Launder Sharma based $k-\varepsilon$	0	$2\nu(\frac{\partial\sqrt{k}}{\partial y})^2$
Lam-Bremhorst and Lien-Leschziner	0	Zero-gradient

4.4 Post-Processing

In order to compare the temporal scales of the fluctuations, a dimensionless frequency (Strouhal number, St) is defined. The St is calculated at the equidistant plane and is defined as

$$St = \frac{fD}{U_b} \tag{4.7}$$

where, f refers to the frequency of the power spectrum. The St number defined for the dominant frequency in the power spectra is used for comparisons.

The convection velocity of the structures is determined by the streamwise space-time correlation coefficient of the cross-flow velocity fluctuations, $R_{u_x u_x}$.

$$R_{u_x u_x}(\Delta z, \Delta t) = \frac{\sum_{i=1}^{N} \left[(u_{xi}(z,t) - \overline{u_x(z)})(u_{xi}(z+\Delta z, t+\Delta t) - \overline{u_x(z+\Delta z)})\right]}{\sqrt{\sum_{i=1}^{N}(u_{xi}(z,t) - \overline{u_x(z)})^2}\sqrt{\sum_{i=1}^{N}(u_{xi}(z+\Delta z, t+\Delta t) - \overline{u_x(z+\Delta z)})^2}} \tag{4.8}$$

The time delay corresponding to the maximum correlation is plotted as a function of streamwise distance, the slope of which gives the convection velocity, U_c of the gap vortices. The streamwise spacing (λ) or the wavelength of the structures is then calculated by using this velocity and the St number corresponding to the dominant frequency obtained in the power spectra.

$$\frac{\lambda}{D} = \frac{U_c}{U_b}\frac{1}{St} \tag{4.9}$$

Chapter 5

Benchmark and Validation

The aim of this chapter is to report the extensive benchmark and validation studies carried out. The description of the benchmark experimental geometry used for the simulations along with the computational domain is given. In order to ensure that the numerical solution is not an artifact of the numerical grid, a grid independence test was done. This was followed by a study on the effect of the length of the periodic domain on the flow dynamics, and whether the length is long enough for the spatial de-correlation of the periodicity of flow-domain and the periodicity of the fluctuations in the flow.

After obtaining a certain level of confidence over the numerical procedures with regards to the mesh and the length of the domain, the next step was to study the effect of various turbulence models on the flow dynamics. It has been claimed in the literature that the eddy-viscosity based models are not sufficient to capture the flow characteristics accurately, and only the Reynolds-stress models (RSM) can be expected to give reasonable results. A comparative study between $k-\varepsilon$ model and the Launder-Reece-Rodi (LRR) RSM was done to verify the literature claims. A comparison was also done between the two different wall-treatment approaches. Based on these studies, a turbulence model was chosen such that it offers an optimum balance between the accuracy and the required computational effort.

Using the optimum settings obtained from the validations, simulations are done and compared with the results of the experiments and other simulations reported in the literature.

5.1 Computational Domain

CFD simulations were carried out in the Guellouz and Tavoularis [2000a,b] geometry discussed in Chapter 3. The detailed geometry is shown in Figure 5.1 and the experimental conditions in Table 5.1. Air was used as the working fluid in the experiments.

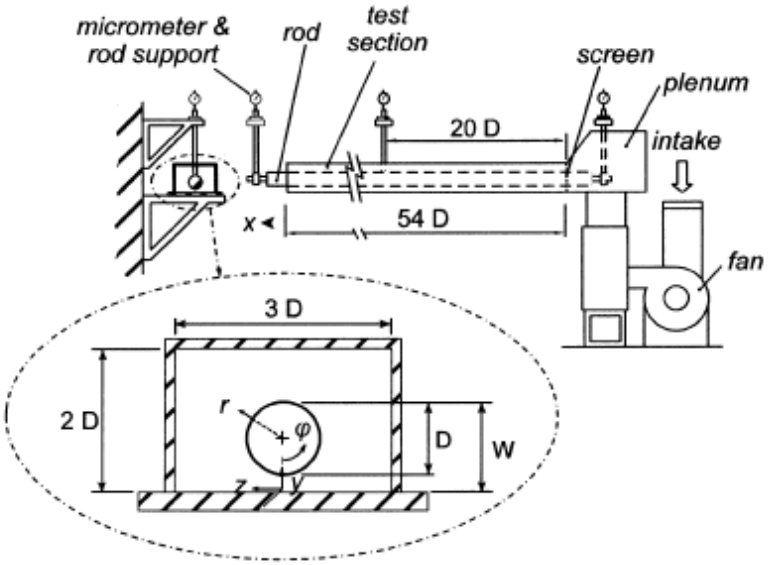

Figure 5.1: Benchmark geometry

Table 5.1: Details of benchmark geometry

W/D	1.025-1.25
Re_b	108000
$U_b(ms^{-1})$	10.1
$D_h(mm)$	160.6

The experiments were conducted on different gap sizes ranging from W/D = 1.025 - 1.25, and a detailed study of the Reynolds-averaged measurements, flow spectrum and phase-averaged quantities of the coherent structures was done. Most of the measurements were done only on the *equidistant plane* (a plane parallel to the bottom wall located at the center of the gap; see Figure 5.2a), at a distance 1.8D from the exit.

Figure 5.2 shows the computational domain used for simulations. Due to the availability of results from both experiments and past simulations, the benchmark studies were carried out with W/D = 1.10. The flow conditions were same as that of the experiment, with the bulk velocity, $U_{bulk} = 10m/s$, and Re based on the hydraulic diameter, $D_h = 1.59D$, equal to 108,000. The equidistant plane shown in Figure 5.2a is defined in Equation 5.1.

$$y = 0.5\frac{W - D}{D} \tag{5.1}$$

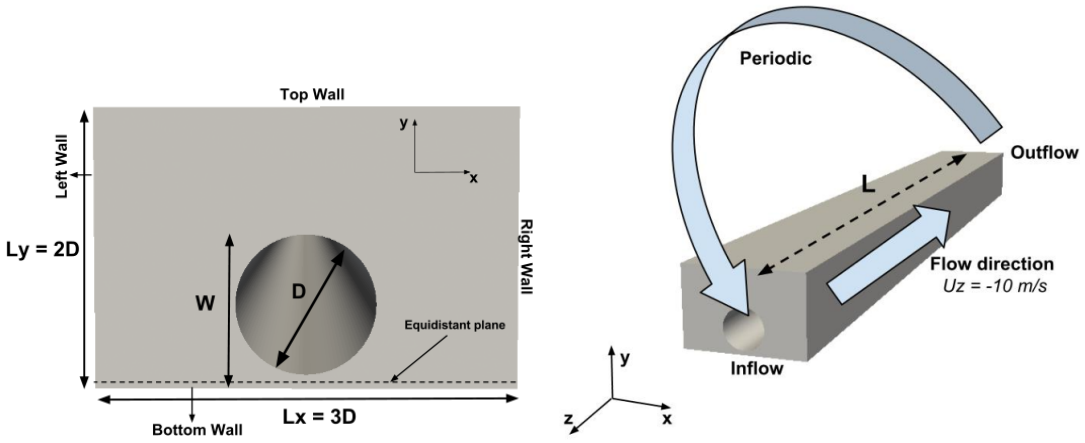

(a) (b)

Figure 5.2: Computational flow domain, (a) Cross-section, (b) 3D flow domain

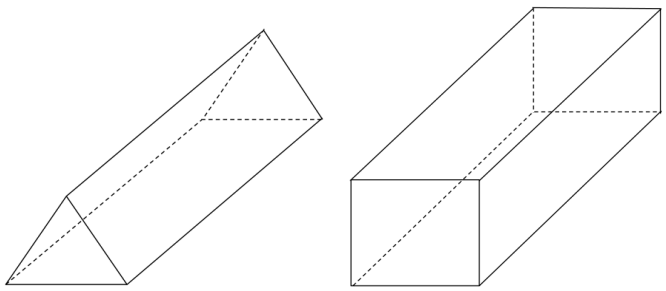

(a) (b)

Figure 5.3: 3-D mesh: Right-prism cells with cross-sectional face as (a) Triangular (b) Quadrilateral

5.2 Grid Independence Studies

Due to the high computational time required for the low-Re turbulence models simulations, grid independence tests were done only for the simulations with the $k - \varepsilon$ turbulence model using wall functions. The 3-D mesh is formed by right-prism cells with the cross-sectional faces formed by either triangles or quadrilaterals (Figure 5.3). The cross-section of the M1 mesh contains only triangular cells, whereas the M2 mesh consists of both triangular and quadrilateral cells (Figure 5.4). The streamwise length is equal for all the cells. The near gap mesh for both of them is shown in Figure 5.5.

Simulations were done using various meshing configurations to check the grid independence. Table 5.2 shows the list of configurations used, the size of the grid elements and the total the number of elements.

The velocity contours on the half of a cross-plane and in the near-gap region for all

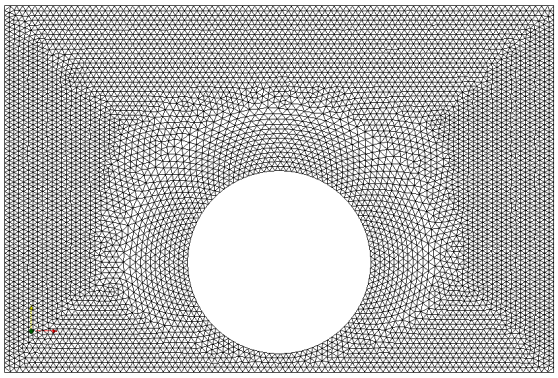

(a)

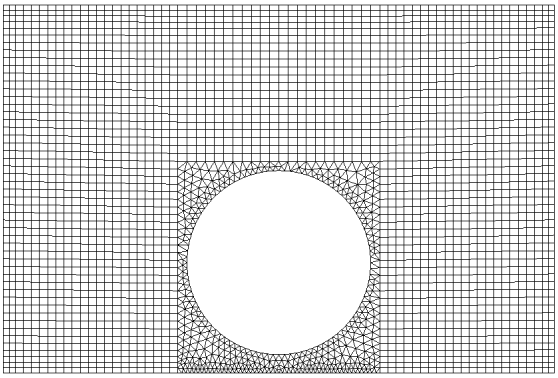

(b)

Figure 5.4: Cross-sectional mesh (a) Triangular elements (M1) and (b) Quad elements (M2)

Table 5.2: Details of the different grids used

Case	Grid Element Size			Number of grid elements	Total number
	x/D	y/D	z/D	x y z	of elements
M2-1	0.045	0.040	0.50	66x50x50	174600
M2-2	0.038	0.033	0.50	78x60x50	235800
M1-1	0.033	0.026	0.50	90x77x50	615850
M1-2	0.033	0.026	0.60	90x77x60	739020
M1-3	0.033	0.026	0.75	90x77x75	923775

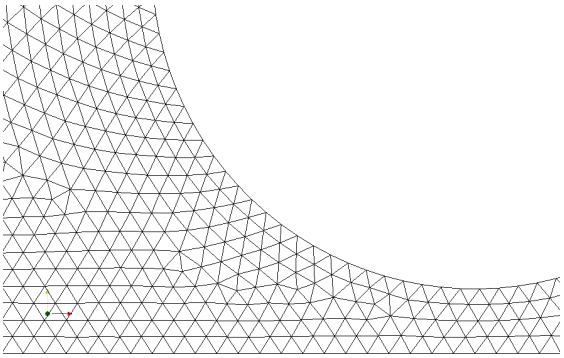

(a)

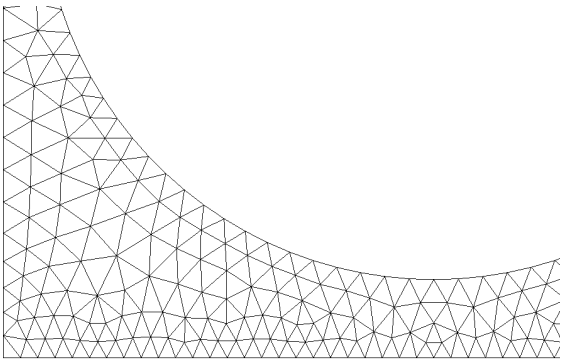

(b)

Figure 5.5: Meshing in the gap region (a) M1-1 and (b) M2-1

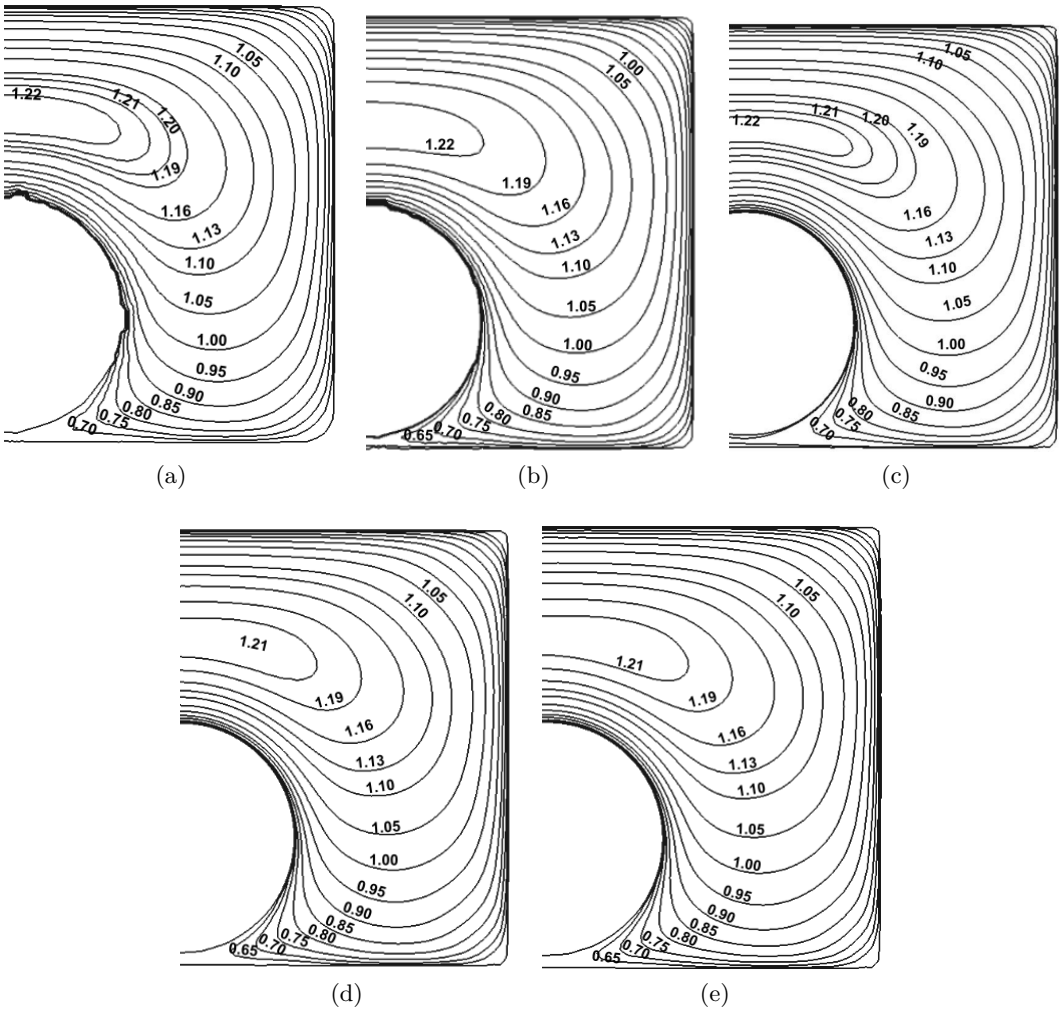

Figure 5.6: Time-averaged dimensionless streamwise velocity component (u_z/U_b) on the cross-plane for the different cases with L_z = 25D: (a) M2-1, (b) M2-2, (c) M1-1, (d) M1-2 and (e) M1-3

the lengths is shown in Figure 5.6 and Figure 5.7 respectively. Identical profiles can be observed in all the cases. The convection velocity (U_c) and streamwise spacing (λ) of the structures are calculated by the technique explained in Section 4.4. Table 5.3 compares the values of St, Uc, λ, peak streamwise velocity and turbulence kinetic energy at the gap center.

The maximum differences are of the order of 8.5 % for St, 2.5 % for U_c, 10 % for λ, 5 % for the streamwise velocity and 8 % for the turbulence kinetic energy. Considering the time constraints, further refinement studies were not carried out, and the current tests are deemed sufficient for the scope of this work. The meshing scheme with the least number of cells, M2-1 is used for all the simulations in this work.

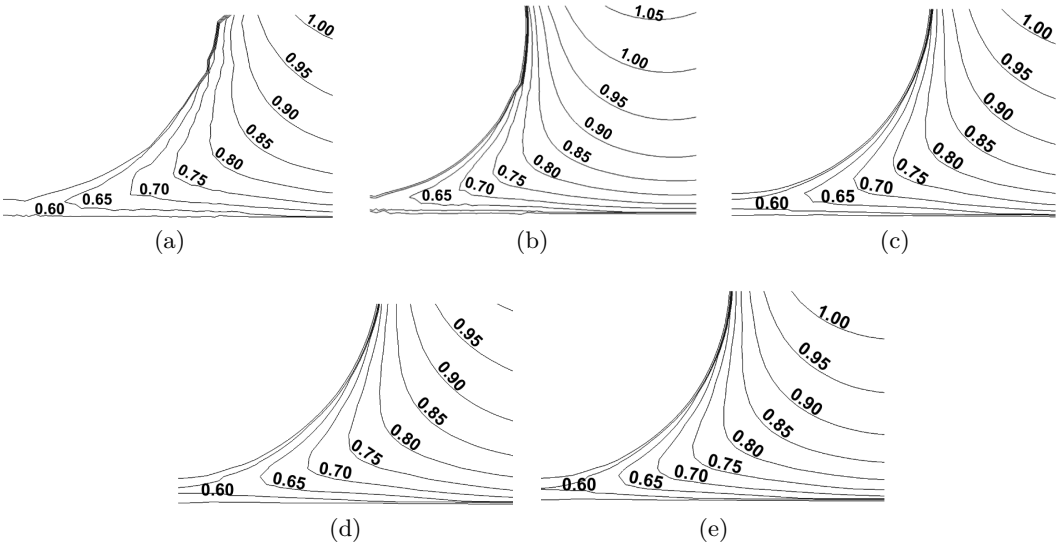

Figure 5.7: Time-averaged dimensionless streamwise velocity component (u_z/U_b) in the near-gap region with L_z = 25D: (a) M2-1, (b) M2-2, (c) M1-1, (d) M1-2 and (e) M1-3

Table 5.3: Effect of the computational grid on the results

Case	St	U_c/U_b	λ/D	U/U_b	k/U_b^2
				at gap center	near the gap
M2-1	0.035	0.808	23.06	0.63	0.0125
M2-2	0.032	0.813	25.40	0.62	0.0130
M1-1	0.034	0.792	23.73	0.60	0.0135
M1-2	0.033	0.798	23.90	0.61	0.0124
M1-3	0.034	0.806	23.93	0.60	0.0125

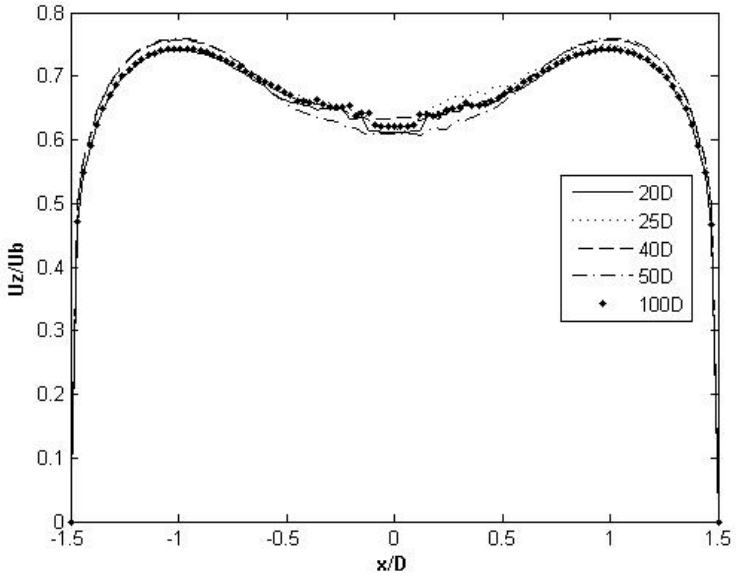

Figure 5.8: Effect of length of periodic domain on the axial velocity profile in the equidistant plane

5.3 Effect of Length of Periodic Domain

It is important that the periodic domain is long enough so that it does not have any influence on the periodicity of the fluctuations in the flow. Chang and Tavoularis [2005, 2008] and Liu and Ishiwatari [2011] conducted simulations with a streamwise length, L_z of 20D. This length is almost six times the experimentally determined wavelength of flow fluctuations (4.2D), and was considered long enough not to effect the periodicity of the fluctuations. Although a recent study by Chang and Tavoularis [2012] concluded that the length of 20D is not long enough for the required spatial decorrelation. Hence, simulations were done using different streamwise lengths (20D, 25D, 40D, 50D and 100D) to determine the sufficient L_z.

Figure 5.8 shows the profile of the normalized time-averaged axial velocity component at the equidistant plane, and no significant differences are observed between the different domain lengths. The velocity contours on the half of a cross-plane and that in the near-gap region for all the lengths are shown in Figures 5.9 and 5.10 respectively, and similar patterns are observed in all the cases.

Figure 5.11 shows the power spectral distributions of the spanwise velocity fluctuations for all the turbulence models. A peak St of around 0.035-0.040 can be observed in all the cases, with similar shapes of the power spectra.

Table 5.4 gives the summary of the different lengths simulated, with the corresponding St, U_c, λ, streamwise velocity and turbulence kinetic energy in the near gap regions.

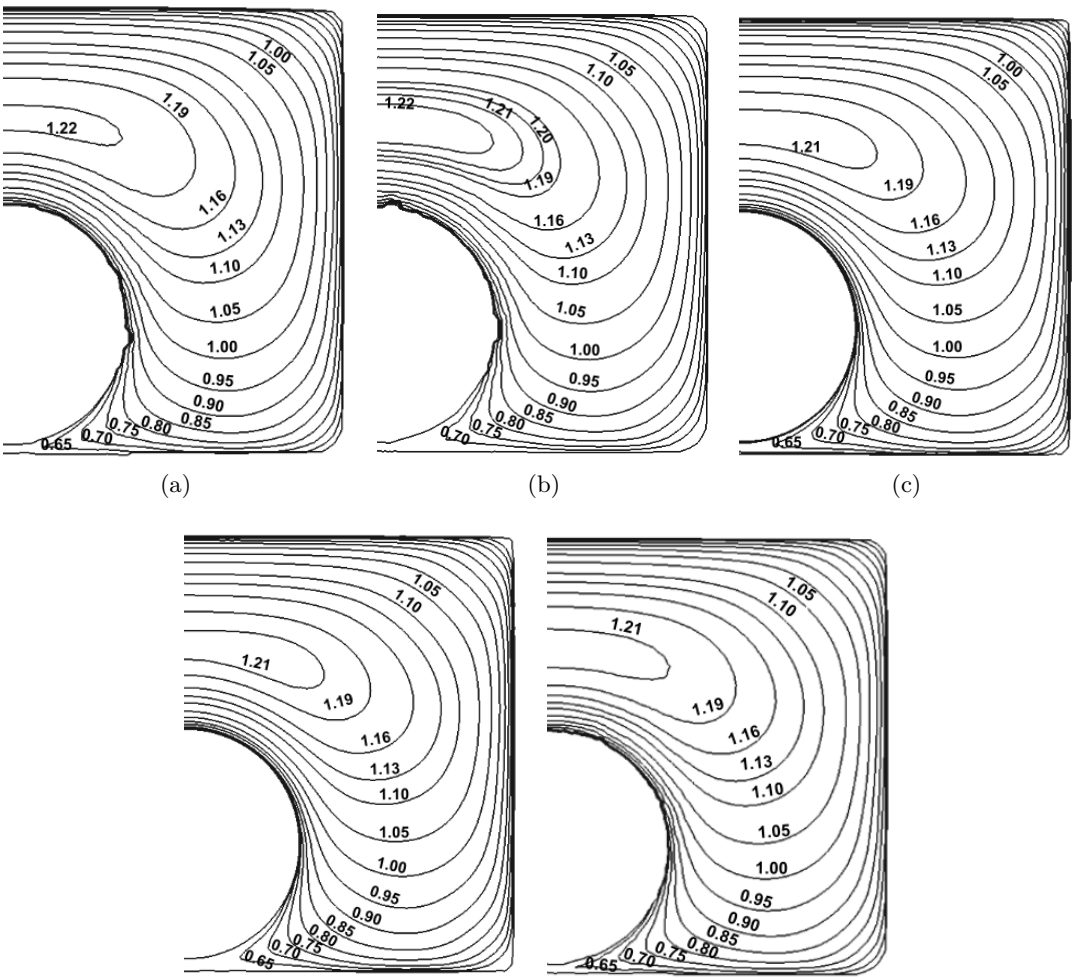

Figure 5.9: Time-averaged dimensionless streamwise velocity component (u_z/Ub) on the cross-plane for different lengths of periodic domain: (a) 20D, (b) 25D, (c) 40D, (d) 50D and (e) 100D

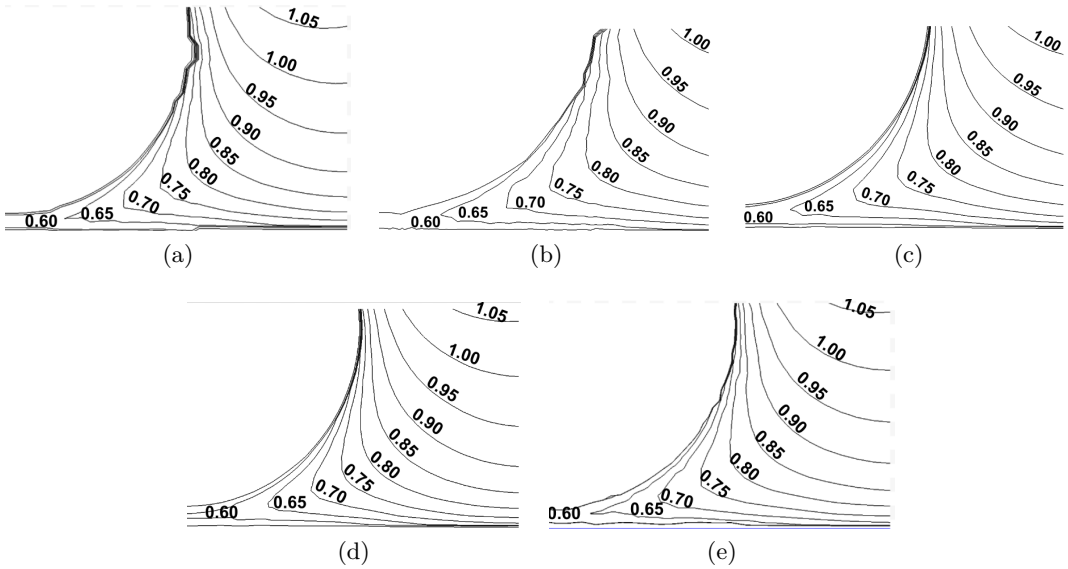

Figure 5.10: Time-averaged dimensionless streamwise velocity component (u_z/Ub) near the gap for different lengths of periodic domain: (a) 20D, (b) 25D, (c) 40D, (d) 50D and (e) 100D

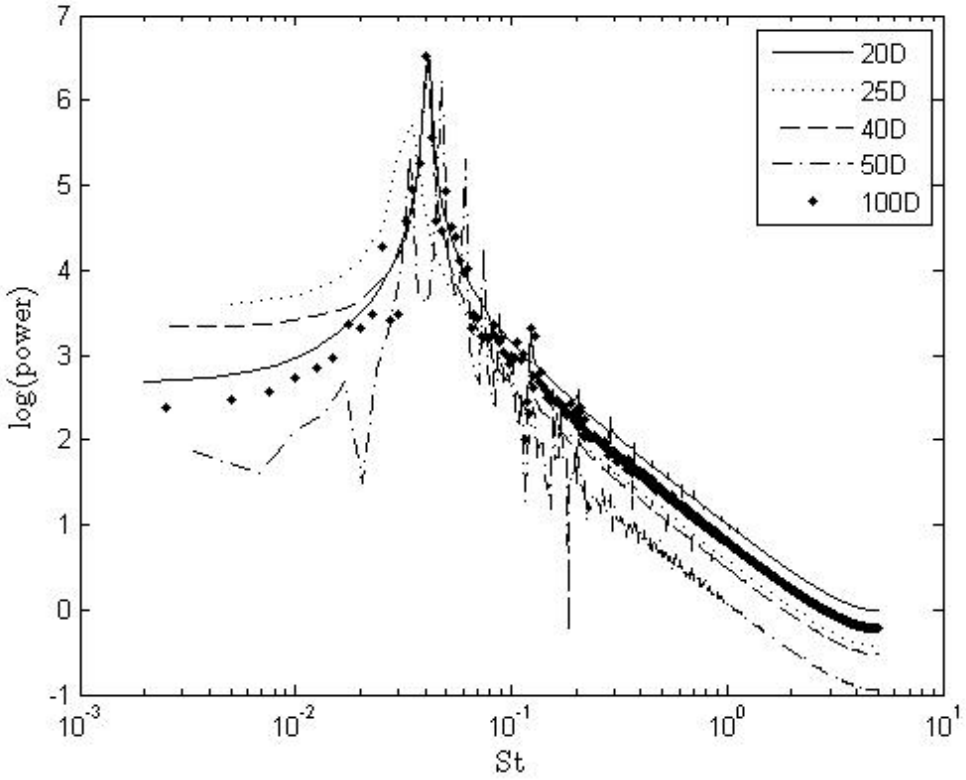

Figure 5.11: Comparison of power spectral distributions of spanwise velocity fluctuations measured at the center of the gap for different lengths of the periodic domain

Table 5.4: Effect of the length of periodic domain

Length L_z/D	St	U_c/U_b	λ/D	U/U_b at gap center	k/U_b^2 near the gap
20	0.042	0.803	19.11	0.60	0.0118
25	0.035	0.808	23.06	0.63	0.0125
40	0.041	0.794	19.27	0.63	0.0120
50	0.047	0.775	16.31	0.60	0.0107
100	0.040	0.799	19.98	0.60	0.0119

The maximum differences, with respect to the longest length (L_z = 100D) are around 15 % for λ, 17.5 % for St and 3 % for U_c. The values at the center of the gap differ by a maximum of 10 % for the axial velocity and 15 % for turbulent kinetic energy. This shows that the length chosen for the current work, 25D is long enough for the de-correlation of the periodicity of flow and that of the fluctuations, contrary to the conclusions of Chang and Tavoularis [2012].

5.4 Effect of Turbulence Model

Different turbulence models were used to study their effect on the dynamics of flow. Due to the strong anisotropic nature of the flow in rod bundles, the low-Re Reynolds-stress models (resolving the wall layer) was chosen in most of the URANS simulations reported in the literature (Chang and Tavoularis [2006], Liu and Ishiwatari [2011], Chang and Tavoularis [2012]). Although RSM requires comparatively lower computational effort to LES and DNS, the total time required for the simulations is pretty high (of the order of months as reported by Chang and Tavoularis [2012]). This is a prohibiting factor while conducting large-scale three-dimensional simulations as in the present case. In comparison, the eddy-viscosity based models as well as RSM with wall functions are nearly ten times computationally less expensive.

The velocity contours in the half cross-sectional plane and in the near-gap region are shown in Figures 5.12 and 5.13 respectively. The contours do not indicate any significant differences.

Figure 5.14 shows the power spectral distributions of the spanwise velocity fluctuations at the center of the gap for all the turbulence models. It can be noticed that the St number corresponding to the peak frequency is roughly the same in all the cases. However, the power spectral shape of the Reynolds-stress equations based LRR turbulence model is different from the others with representation of many sub-harmonics and

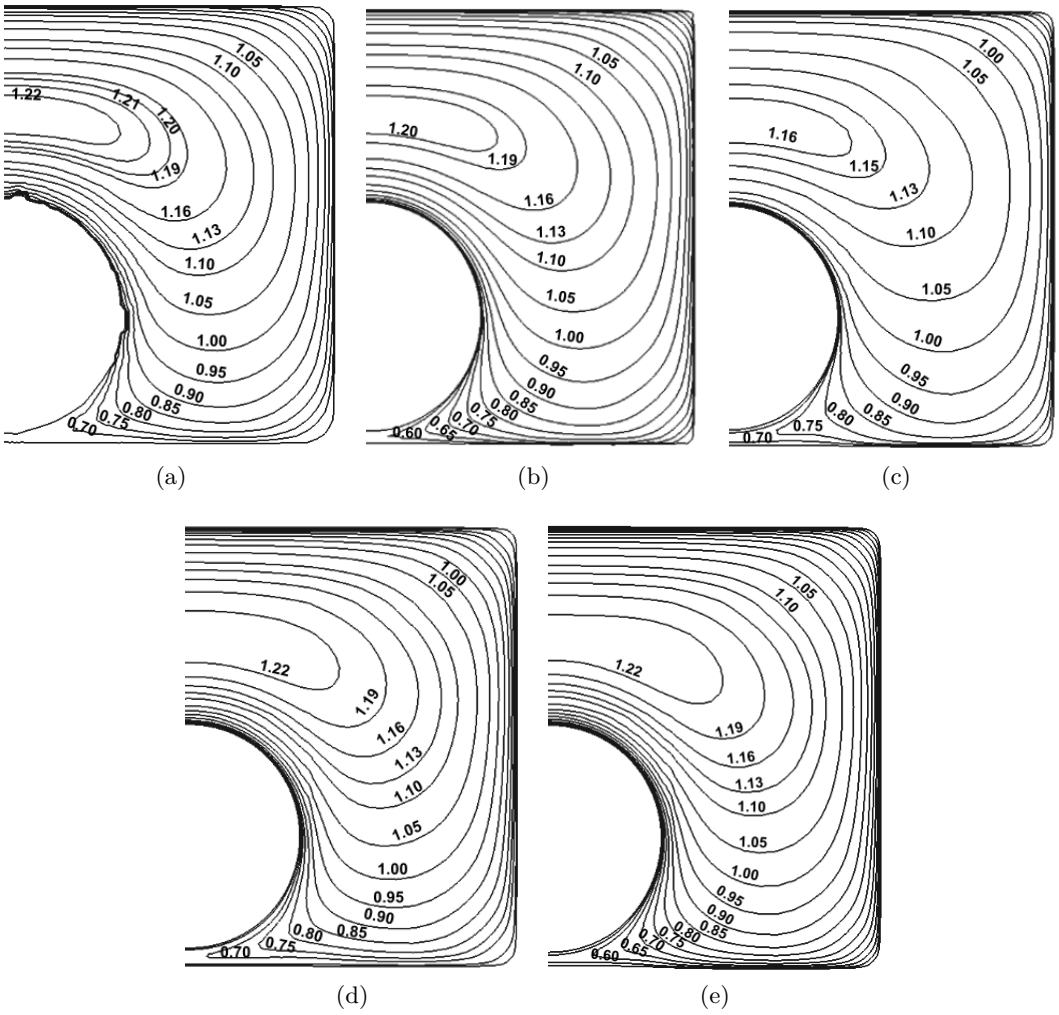

Figure 5.12: Time-averaged dimensionless streamwise velocity component (u_z/U_b) on the cross-plane for different turbulence models: (a) $k-\varepsilon$, (b) LRR, (c) Lam-Bremhorst, (d) Lien-Leshziner and (e) Launder-Sharma

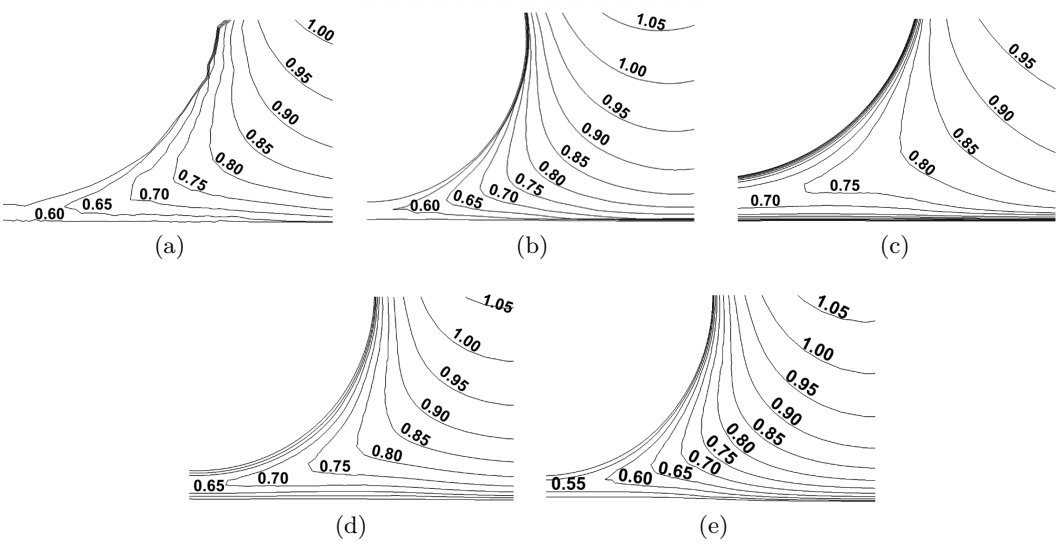

Figure 5.13: Time-averaged dimensionless streamwise velocity component (u_z/U_b) in the near-gap region for different turbulence models: (a) $k-\varepsilon$, (b) LRR, (c) Lam-Bremhorst, (d) Lien-Leshziner and (e) Launder-Sharma

peaks at low-intensities. Physically this translates to the fact that the Reynolds-stress model is able to capture a richer dynamics of the flow in comparison to that of the eddy-viscosity based models. However, the most dominant fluctuations are captured by all the turbulence models. This suggests that the bulk flow dynamics are caused by a mechanism which is not very complex in nature. The fact that a simple $k-\varepsilon$ model is able to predict the fluctuations, indicates that there is no major effect of either the complex turbulence dynamics or the anisotropy associated with the flow.

Table 5.5 summarizes the various coherent structure characteristics and mean flow parameters for all the turbulence models. Firstly, on comparing the results obtained between the $k-\varepsilon$ model with and without wall functions, the maximum differences (considering $k-\varepsilon$ with wall functions as the base model) are 15 % for St, 4.5 % for U_c and 8.5 % for λ. Comparing the eddy-viscosity based $k-\varepsilon$ model and Reynolds-stress LRR model (both using wall functions), the differences are 8 % for St, 3 % for U_c and 12 % for λ. Hence, it can be concluded that the $k-\varepsilon$ model using wall functions is able to capture the flow dynamics fairly accurately, and considering the least computational effort, it was chosen as the main working model for the present work.

5.5 Flow Development

This section tries to address the issue flow development in the geometry used for simulations. The recent work by Chang and Tavoularis [2012] concludes that the experimental

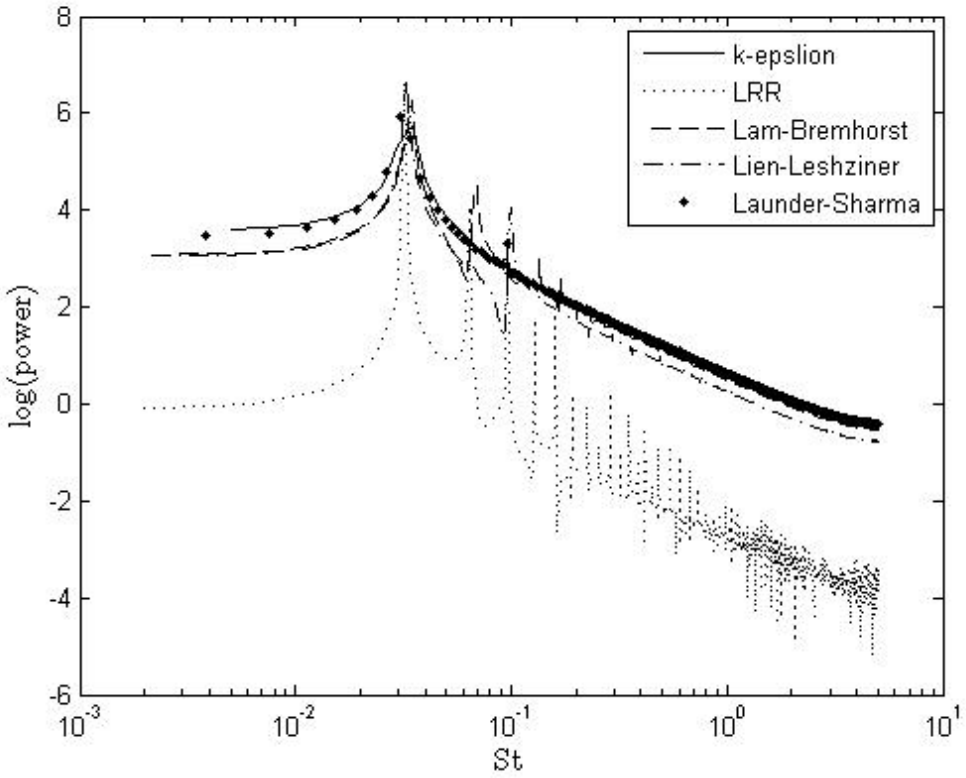

Figure 5.14: Comparison of power spectral distributions of spanwise velocity fluctuations measured at the center of the gap for different turbulence models

Table 5.5: Effect of the turbulence model on flow dynamics

Model	Wall-Function	St	U_c/U_b	λ/D	U/U_b at gap center	k/U_b^2 near the gap
$k-\varepsilon$	Y	0.035	0.808	23.06	0.63	0.0125
LRR	Y	0.032	0.782	24.43	0.60	0.0128
Lam-Bremhorst	N	0.034	0.844	24.37	0.73	0.0127
Lien-Leshziner	N	0.032	0.813	25.02	0.69	0.0145
Launder-Sharma	N	0.030	0.784	25.79	0.57	0.0132

flow conditions were not fully developed, and simulations with a uniform inlet boundary conditions were used to benchmark the experimental results. Similar findings are obtained in the present simulations.

According to the Taylor's hypothesis (Taylor [1938]), the spatial and temporal characteristics of turbulence can be related by the bulk velocity, U_b. Hence, in the present work, the terms developing length and developing time are used synonymously.

Comparisons between the current simulation results (using mesh M2-1, $L_z = 25$D and $k-\varepsilon$ turbulence model with wall functions) with those the experiments and simulations reported in the literature are done. Many recent simulation works (Chang and Tavoularis [2005, 2006, 2008], Liu and Ishiwatari [2011], Chang and Tavoularis [2012]) have tried to benchmark the experimental results of Guellouz and Tavoularis [2000a,b]. A summary of the simulation settings, turbulence model and the type of simulations is given in Table 5.6.

Table 5.6: Summary of past simulations

Reference	L_z	Turbulence model	Inlet boundary-conditions
Chang and Tavoularis [2005, 2006]	20D	low Re RSM	Periodic
Chang and Tavoularis [2008]	20D	low Re RSM	Periodic
Liu and Ishiwatari [2011]	20D	EARSM [1]	Periodic
Chang and Tavoularis [2012]	108D	low Re RSM, LES	Uniform inlet
Experiment	54D	N/A	Fully-developed

Firstly, a comparison of the time-averaged velocity and turbulence kinetic energy profiles in the case of present simulations and those of the past experiments and simulations is done, and the differences are noted. This is followed by comparisons of the temporal dynamics (frequency and length scales of fluctuations) in all the cases.

5.5.1 Mean-Flow Characteristics

Figures 5.15 and 5.16 compares the normalized time averaged axial velocity contours for the experiment, past simulations and the current $k-\varepsilon$ model simulations in the half cross-sectional plane and the near-gap region respectively. It can be seen that contours of the experiment in Figure 5.15a are very similar to the contours of the developing flow simulations of Chang and Tavoularis [2012] at z = 50D in Figure 5.15e. They are also similar to the contours of Liu and Ishiwatari [2011] in Figure 5.15d. This indicates

[1] Explicit-Algebraic Reynolds Stress Model

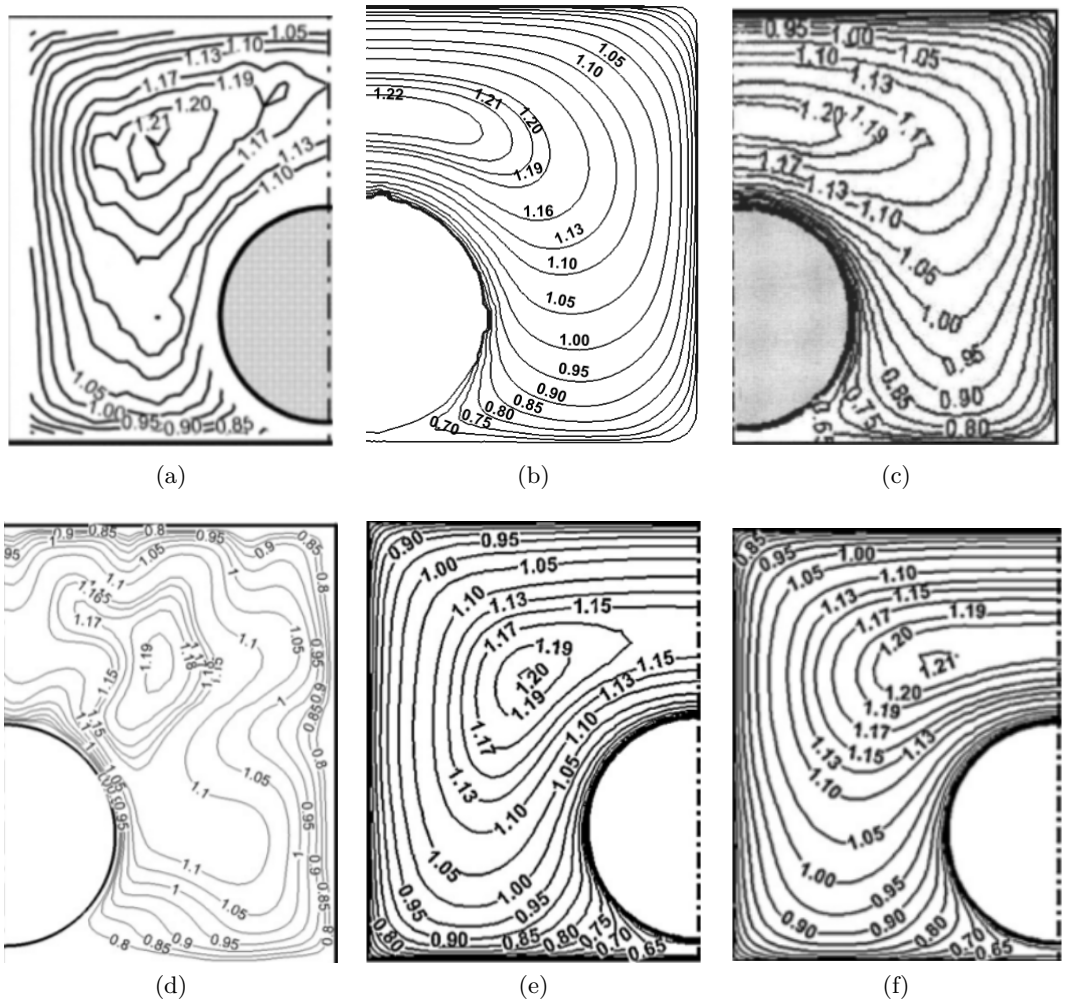

Figure 5.15: Time-averaged dimensionless streamwise velocity component (u_z/Ub) on the cross-plane for (a) GT experiments, (b) current simulations, (c) Chang(2005) simulations, (d) Liu et al. (2011) simulations, (e) Chang et al. (2012) at z = 50D, (f) Chang et al. (2012) at z = 100D

that the flow wasn't fully developed in both the experimental flow loop of Guellouz and Tavoularis [2000a,b] and the simulations of Liu and Ishiwatari [2011].

On comparing the contours at z=100D in (Figure 5.15f) and the current simulations (Figure 5.15b), differences can be observed in the open sub-channel. The contours of the current simulations are similar to that of the simulations of Chang and Tavoularis [2005], Figure 5.15c. The experimental u_z/U_b at the gap center is about 0.70 (Figure 5.16a), similar to that observed by Liu and Ishiwatari [2011] (Figure 5.16d). Low values of u_z/U_b are observed in the center of the gap in Figure 5.16c of the simulations of Chang and Tavoularis [2005]. The near-gap contours of the present simulations (Figure 5.16b) are closer to those of Chang and Tavoularis [2012](Figure 5.16f) at z=100D.

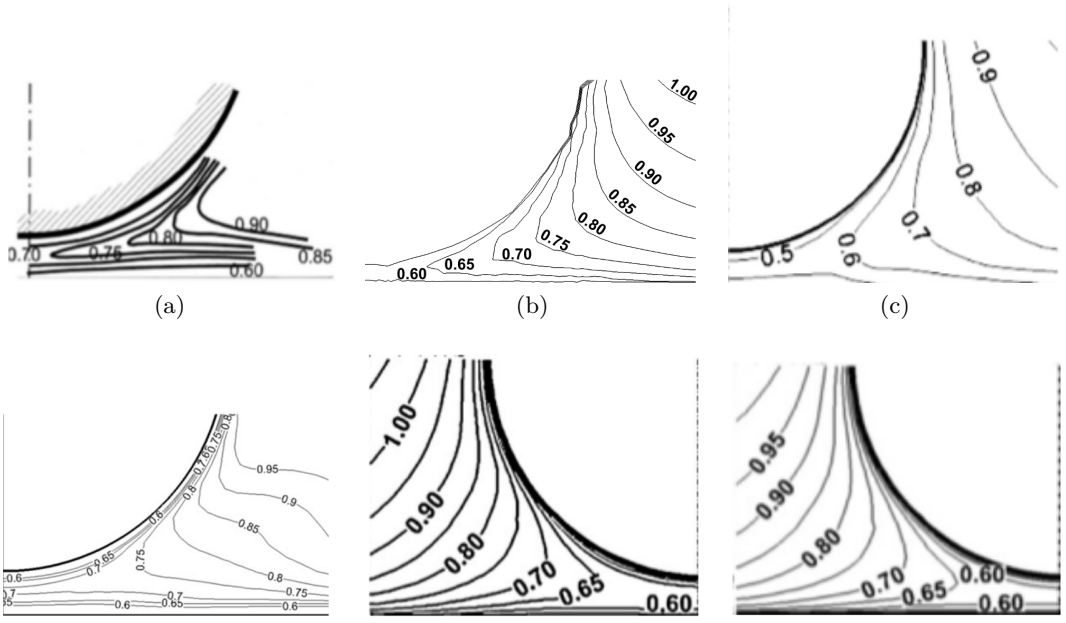

Figure 5.16: Time-averaged dimensionless streamwise velocity component (u_z/Ub) near-gap region (a) GT experiments, (b) current simulations, (c) Chang(2005) simulations, (d) Liu et al. (2011) simulations, (e) Chang et al. (2012) at z = 50D, (f) Chang et al. (2012) at z = 100D

Figure 5.17 shows a comparison of the streamwise velocity profiles at the equidistant plane, between the developing flow simulations and the present ones. Thinning of the shear layer can be observed with flow development. This could be the reason behind the differences in contour shapes of the present simulations (Figure 5.15b) and the developing flow simulations at z=100D (Figure 5.15f).

Figure 5.18 shows the contours of dimensionless turbulent kinetic energy in all the cases. Regions of high turbulent kinetic energy can be observed on either side of the gap in both experiments and simulations. The overall shape of the contours at the region above the rod are similar in all the cases, however, the finer details are different owing the developing flow in Figure 5.18a, 5.18d and 5.18e. Similarities are observed between the present simulations (Figure 5.18b) and those of Chang and Tavoularis [2005](Figure 5.18c).

The two core regions of high k/U_b^2 can be observed by looking at the near-gap contours of k/U_b^2 in Figure 5.19. A maximum value of 0.012 in the experiments (Figure 5.19a) compares well with the 0.013 in the present simulations (Figure 5.19b), however differences are observed in the open sub-channel region above the rod. The core region extends to distance of almost 0.75D on either side of the gap in the present simulations (Figure 5.19b), whereas the distance is about 0.6D in case of the simulations

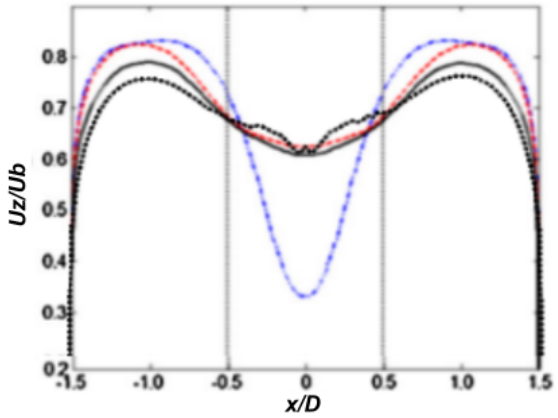

Figure 5.17: Axial velocity profiles in the equidistant plane of the developing flow simulations of Chang and Tavoularis [2012] (blue line is at z=30D, red line at z=50D, black line at z=100D) and those of the present simulations with periodic boundary conditions (dotted black line

of Chang and Tavoularis [2012] (Figure 5.19d, 5.19e). It can be clearly seen that very little development of the core region has taken place in the simulations of Chang and Tavoularis [2005] (Figure 5.19c).

5.5.2 Temporal and Spatial Scales of Fluctuations

Table 5.7 compares the St, λ and reported time for flow development in case of simulations with periodic boundary conditions. The time required for flow development is defined in terms of T_c, which is one flow over run time, defined as

$$T_c = \frac{L_z}{U_{bulk}} \tag{5.2}$$

The differences of a factor of 4-5 are observed in the reported time required for flow development. The values of St number in case of the past simulations with periodic boundary-conditions are very close to those of the experiment. The phenomenon of shear layer thinning with flow development can be cited as the main reason of significant differences in the Strouhal number of the present simulations with that of experiments.

Therefore, considering the velocity and turbulence kinetic energy contour plots, shear layer profile and the high values of St, it can be concluded that flow wasn't fully developed in time in both the experiment of Guellouz and Tavoularis [2000a,b] and the simulations of Chang and Tavoularis [2005, 2006, 2008], Liu and Ishiwatari [2011].

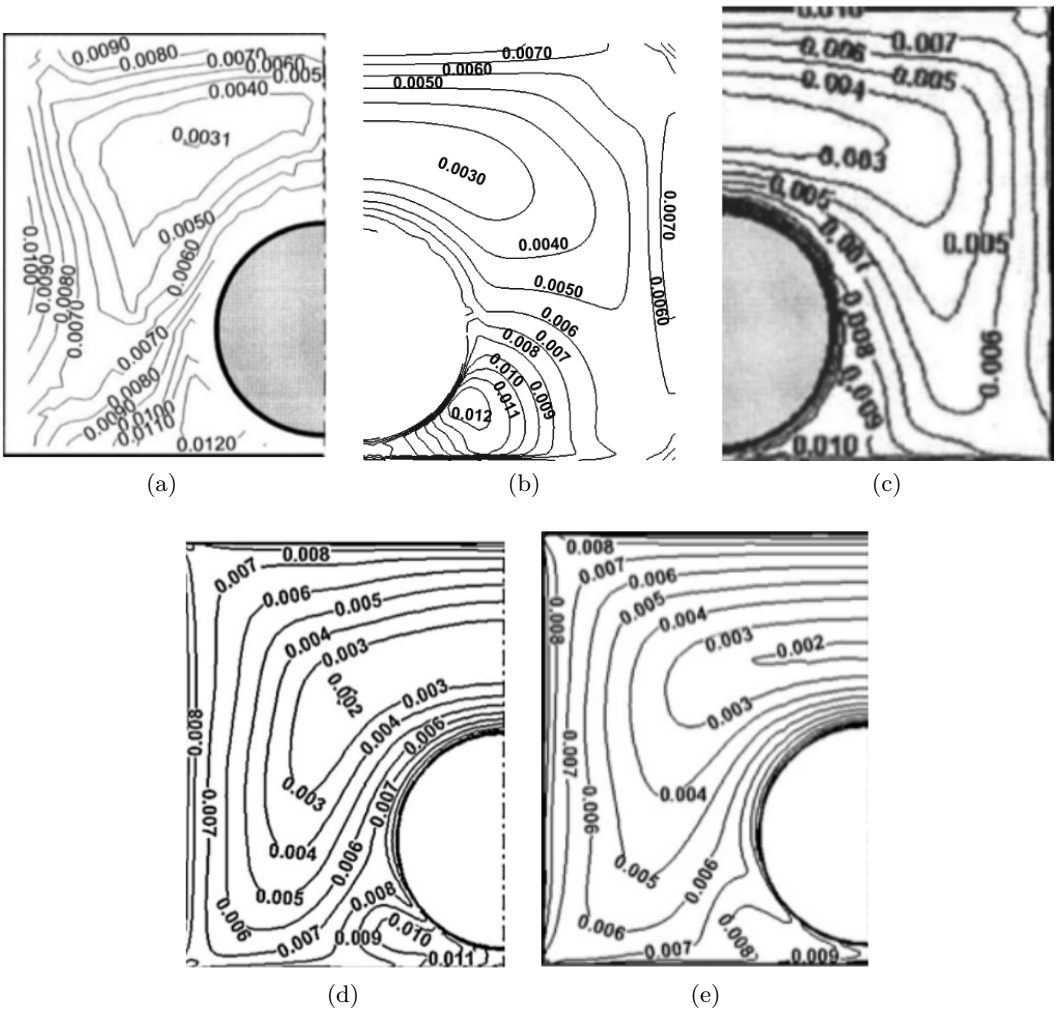

Figure 5.18: Time-averaged dimensionless turbulent kinetic energy (k/U_b^2) on the cross-plane for (a) GT experiments, (b) current simulations, (c) Chang(2005) simulations, Chang et al. (2012) at (d) z = 50D and (e) z = 100D

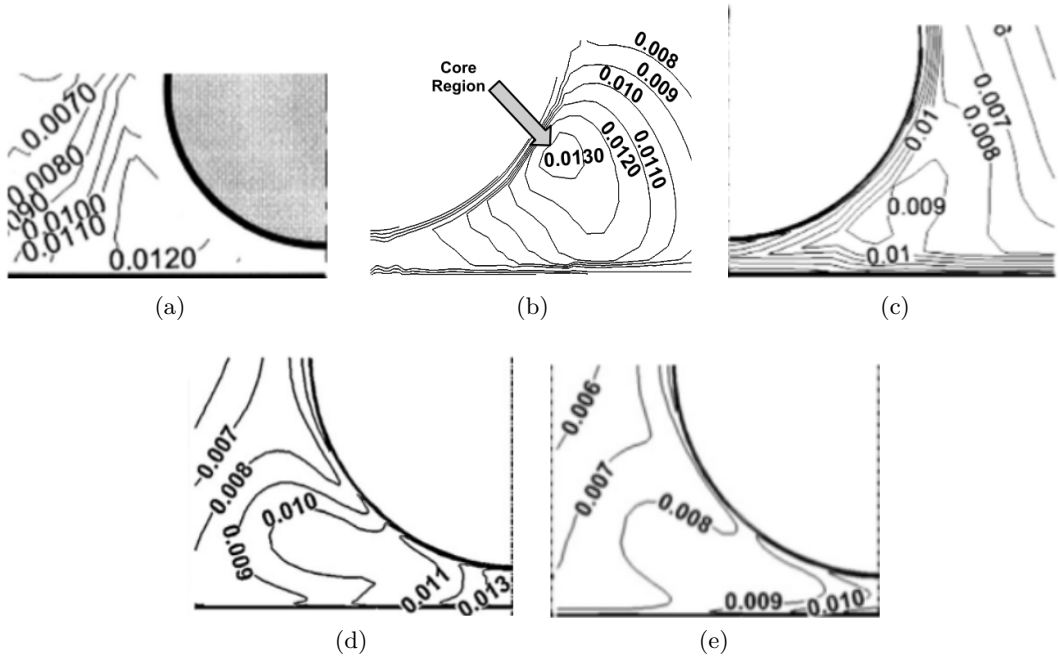

Figure 5.19: Time-averaged dimensionless turbulent kinetic energy (k/U_b^2) on the cross-plane for (a) GT experiments, (b) current simulations, (c) Chang(2005) simulations, Chang et al. (2012) at (d) z = 50D and at (e) z = 100D

Table 5.7: Comparison of the temporal characteristics

Reference	Reported Time for flow development	Strouhal number	Streamwise spacing
Chang and Tavoularis [2005, 2006]	$5.7T_c$	0.146	4.9D
Chang and Tavoularis [2008]	$7.6T_c$	0.18	4.0D
Liu and Ishiwatari [2011]	N/A	0.18	4.2D
Chang and Tavoularis [2012]	N/A	0.20 (RSM)	3.8D (RSM)
		0.17 (LES)	4.3D (LES)
Present simulations	$25T_c$	0.035	23.06D
Experiment	N/A	0.17	4.2D

5.6 Summary

The grid independence, effect of the streamwise length of the periodic domain, the effect of turbulence models and the comparisons of results with the past experiment and simulations were done. Interesting conclusions were obtained and they can be summarized as follows:

- The length of the periodic domain 25D is sufficient to resolve the flow dynamics accurately. This is against the claim by Chang and Tavoularis [2012] that past simulations led to erroneous results due the short length of periodic domain.
- There is very little effect of the turbulence models on the temporal and time-averaged characteristics of the coherent structures. The results are similar both with or without wall functions, and with eddy-viscosity or Reynolds-stress models. It is concluded that the $k-\varepsilon$ model using wall functions is sufficient to accurately capture the large-scale flow dynamics.
- The time required for flow development is much longer in the geometry used for simulations in this work. On comparing the results of past experiment and simulations with the current simulations, it can be seen that they were carried out for much shorter time.

With these interesting conclusions, the rest of the work is based on the following conditions,

- Length of Periodic Domain: $L_z = 25\text{D}$
- Type of simulations: Periodic boundary conditions
- Turbulence model: $k-\varepsilon$ model with wall functions

Chapter 6

Hydrodynamics in Channel with Rod Geometry

Following the conclusions of the benchmark and validations carried out, simulations were done using the $k - \varepsilon$ turbulence model with wall functions. The flow dynamics were investigated in order to answer a number of questions related to the structure of the fluctuations present in the flow. Firstly, in order to ascertain the effect of the flow fluctuations on the the mean-flow parameters, the various patterns of time-averaged velocity, RMS of velocity fluctuations and kinetic energy were studied.

The flow-visualization and streamlines of the resolved velocity field is shown. It is expected that the patterns observed will give an indication of the size, shape and extent of these fluctuations. The time-evolution of the streamlines are also plotted in order to determine the periodicity of the fluctuations. The quantification of the various characteristics: spatial, temporal and velocity scales of the fluctuations are done. This formalization will help not only in understanding the extent of these structures, but also for future comparisons.

An effect of the gap-size on these fluctuations is studied with an aim to obtain the critical gap-size at which the intensity of the fluctuations are the maximum. It will also be interesting to compare the various scales of these structures at different gap-sizes. It is expected that the domain will behave like a fully-developed turbulent channel at both zero and very-large gap-size.

6.1 Mean Flow Parameters

6.1.1 Streamwise Velocity

Figure 6.1a and 6.1b show the time-averaged dimensionless streamwise velocity contours in the cross-plane and the details in the near-gap region. The maximum velocity in the

simulations is predicted in the symmetry region above the rod. The symmetry of the mean flow about the center-line can also be noticed. The velocity gradually reduces towards the center of the channel, with a minimum of $0.62U_b$ at the center of the gap. The dimensionless time-averaged spanwise and wall-normal velocity components are of the order of 0.1 % of the bulk flow, indicating the absence of secondary flow. This can also be due to the inability of $k - \varepsilon$ turbulence model to predict secondary flows.

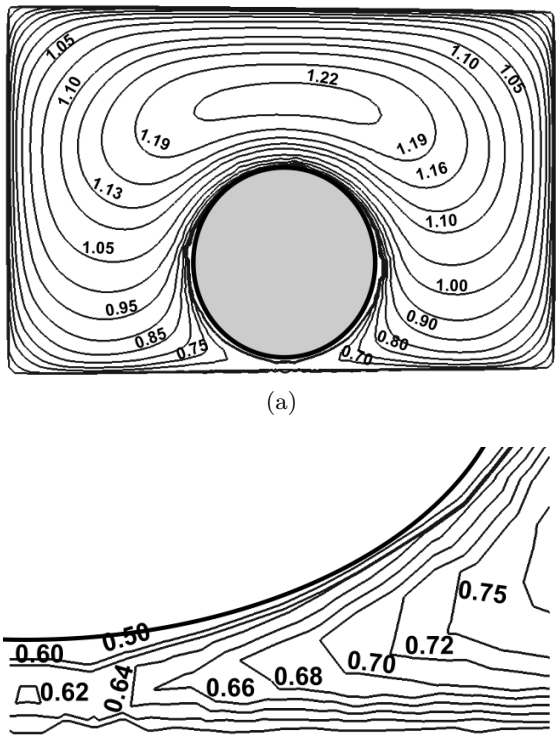

(a)

(b)

Figure 6.1: Time-averaged dimensionless streamwise velocity (u_z/U_b) on the (a) cross-sectional plane and (b) in the near-gap region

The streamwise velocity profile at two planes (shown in Figure 6.2) is plotted in Figure 6.3. It can be seen that the velocity profile at $y/D = 1.55$ (plane equidistant between the top of the rod and the upper wall) resembles that of a fully developed turbulent channel flow (Kim et al. [1987]). The center-line velocity is $1.22U_b$, compared to the $1.16U_b$ predicted by the DNS data of Kim et al. [1987] ($Re = 3300$), differing by around 5 %. The maximum velocity at the equidistant plane in the gap region is $0.74U_b$ located approximately at $x = -D$ and $x = D$. The velocity decreases by about 17 % towards the center of the gap, resulting in a relatively smooth shear layer.

The streamwise velocity profile at the symmetry plane from $y = 0$ to $y = 0.1D$ is plotted in Figure 6.4a. As only few mesh points were present in the gap region (due to the use of wall functions), a smooth curve is fitted. This also resembles the profile for a fully developed turbulent flow (Kim et al. [1987], $Re = 3300$). The local Re at the center

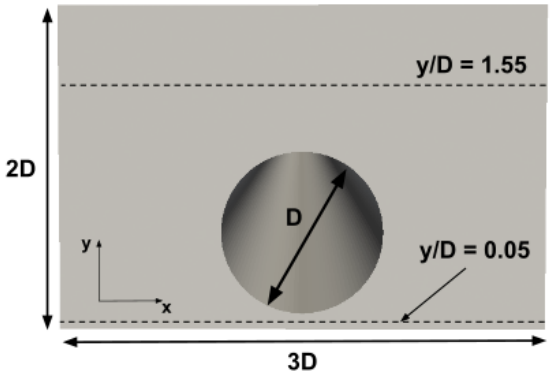

Figure 6.2: Equidistant plane in the gap and channel region

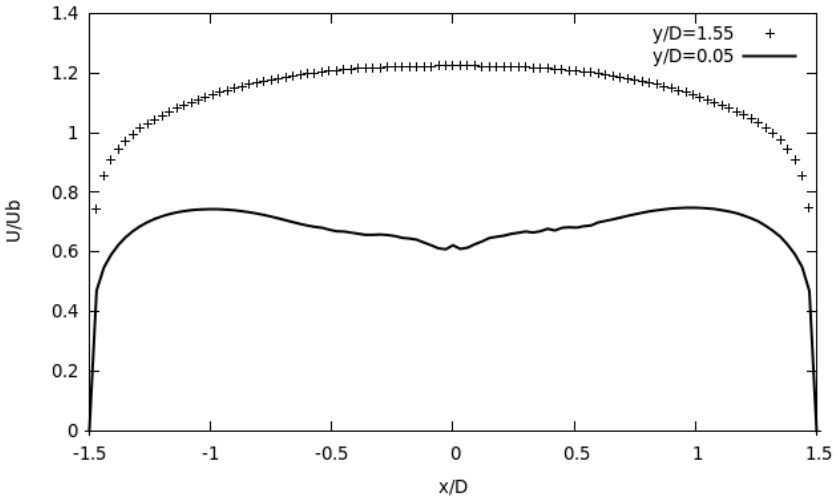

Figure 6.3: Time-averaged dimensionless streamwise velocity (U/U_b) in the equidistant planes

of the gap region was around 4000, indicating highly turbulent flow in the region. These predictions are qualitatively similar to the profiles observed by Chang and Tavoularis [2008] and Chang and Tavoularis [2012] in Figures 6.4b and 6.4c.

6.1.2 Velocity Fluctuations

The resolved velocity field is defined as

$$u' = u - \overline{u} \tag{6.1}$$

Figure 6.5 shows the plot of the RMS of the resolved velocity component ($\sqrt{\overline{u'^2}}$) at the equidistant plane in the gap region, $y = 0.05D$. The spanwise intensity has a maximum in the center of the gap, whereas two peaks are observed for the streamwise intensity. This indicates that the cross-flow is concentrated in the center of the gap, and

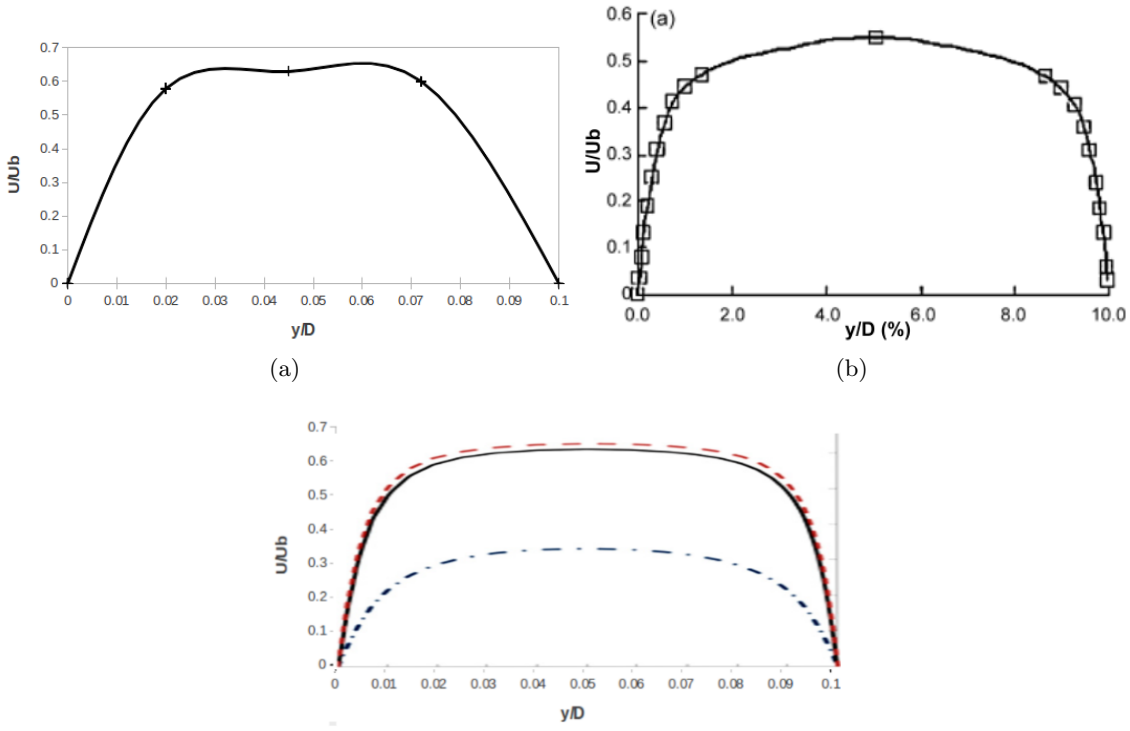

Figure 6.4: Time-averaged dimensionless streamwise velocity (U/U_b) in the gap region (a) present simulations, (b) Chang et al. (2008) and (c) Chang et al. (2012)

its effect on the axial flow is observed in the two regions or sub-channels on either side of the gap. This profile also suggests the presence of some additional mechanism other than turbulence that leads to a spike in the RMS fluctuations near the gap.

Figure 6.6 shows the comparison between the kinetic energy of resolved fluctuations ($\overline{k}_c = 0.5 * (\overline{u_x'^2} + \overline{u_y'^2} + \overline{u_z'^2})$) and time-averaged turbulence kinetic energy (k_{nc}). At regions away from the gap and above the rod, the k_{nc} is higher than k_c, which indicates that the intensity of additional dynamics discussed above reduces away from the gap. Whereas, in the near-gap region the resolved component is quite higher than the unresolved turbulence kinetic energy.

The total turbulence kinetic energy is obtained by the summation of the resolved and un-resolved components ($k_t = k_c + k_{nc}$), under the assumption that both the kinetic energy components are un-correlated. The profile is shown in Figure 6.7, and it should be noted that the values are zero at the wall (the walls are not shown in the figure). Two core regions of high turbulence kinetic energy exist at either side of the gap, which correspond to the two peaks in the profile of u_x' in Figure 6.5. The minimum is located in the center of the channel region above the rod. The partition of the turbulent kinetic energy is quite different in the gap region from that of the open channel. In the center of

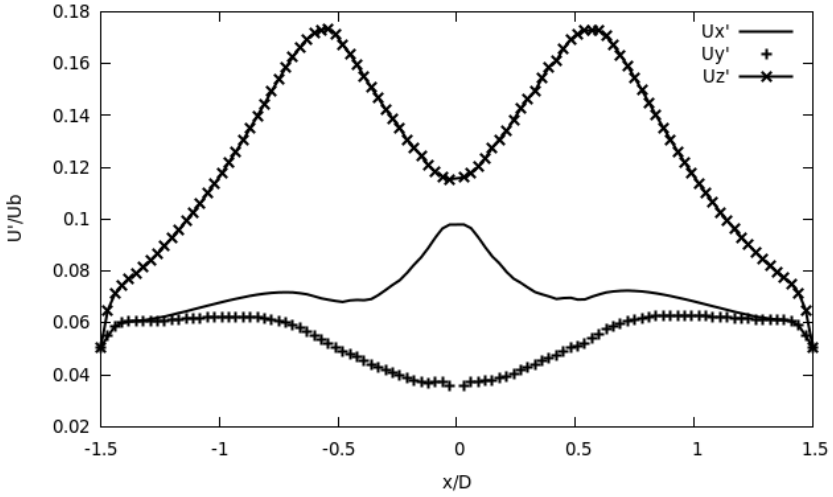

Figure 6.5: RMS of resolved velocity components (u'/U_b) in the equidistant planes

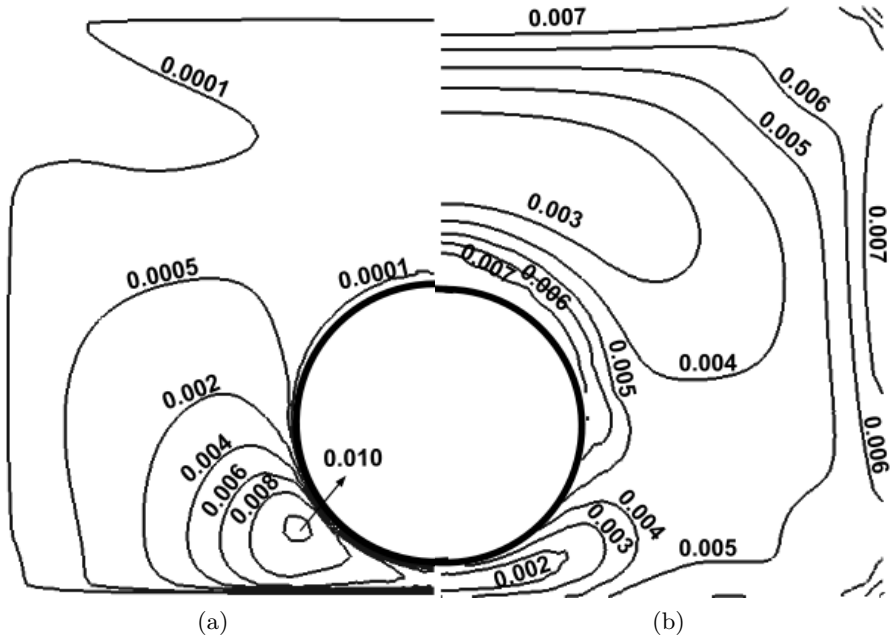

(a) (b)

Figure 6.6: Time-averaged kinetic energy of: (a) resolved fluctuations, k_c and (b) turbulence, k_{nc}

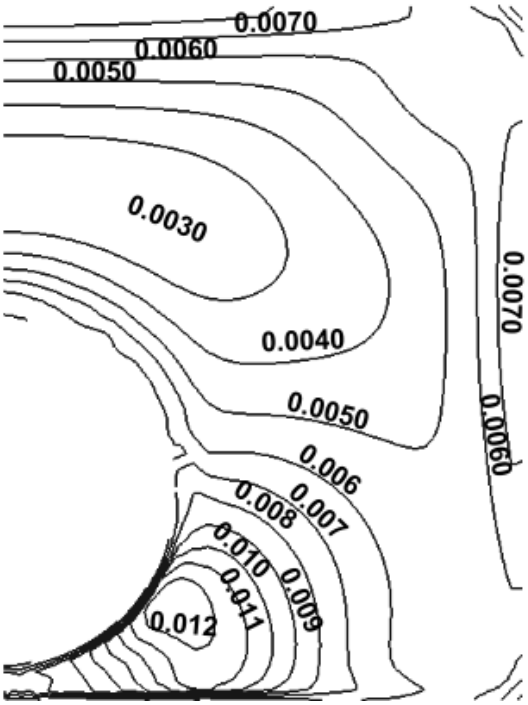

Figure 6.7: Contours of time-averaged dimensionless turbulence kinetic energy (k/U_b^2)

the gap, the axial turbulent intensity, u'_z contributes to 55 % of the total, the spanwise intensity 37 % and the contribution of u'_y is around 7 %. Whereas in the open channel region, where the turbulent intensity is maximum, the axial intensity contributes the maximum at around 80 %, and the other two contributes 10 % each.

The time-averaged profiles of various quantities indicate the presence of some additional dynamics present in the flow other than turbulence. Peaks were observed in the RMS of the resolved velocity components near the gap region.

6.2 Transient Analysis

6.2.1 Flow Visualizations

The streamlines of the resolved velocity vector field at the equidistant plane is plotted in Figure 6.8. Two large swirling zones can be noticed. The front of these swirling zones point in two different directions.

Three-dimensional streamlines are shown in Figure 6.9, and here the two large scale structures are clearly seen. These are two sledge-shaped structures, which extend from the gap region to all the way to the open channel region above the rod. The streamlines are colored by the dimensionless resolved spanwise velocity component, u'_x/Ub. There is also an indication of interaction between the structures. Zooming in the three-

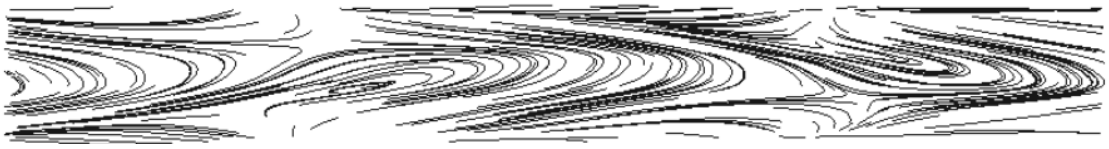

Figure 6.8: Streamlines of resolved velocity vector at the equidistant plane in the gap region

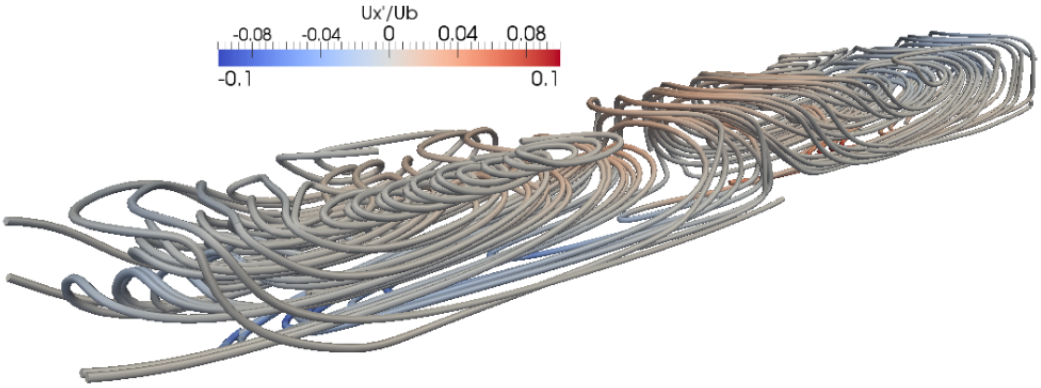

Figure 6.9: Three dimensional streamlines of the resolved velocity field

dimensional vectors of one of these structures, the swirling zones can be observed in greater detail. Figure 6.10 shows the vectors colored by the magnitude of dimensionless resolved velocity vector. Elongated elliptical shaped vortices are formed, and two bulging regions around the rod can be observed. The magnitude of the vectors are maximum in the gap region. These structures and their features clearly coincide with the profiles of RMS of resolved velocities observed in the gap region.

Figure 6.11 shows that the two structures are counter-rotating, similar to the coherent structures found in rod bundle flows (Meyer [2010]). Q-factor is generally used for

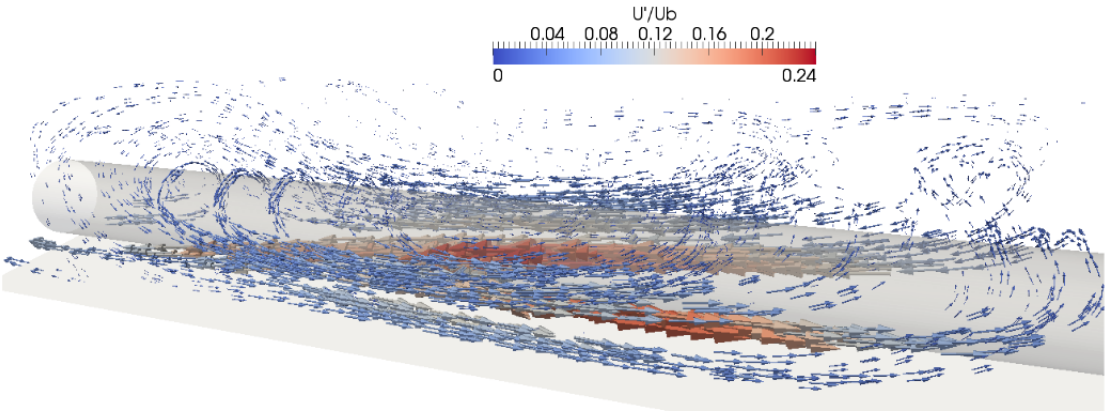

Figure 6.10: Three dimensional vectors of the resolved velocity field

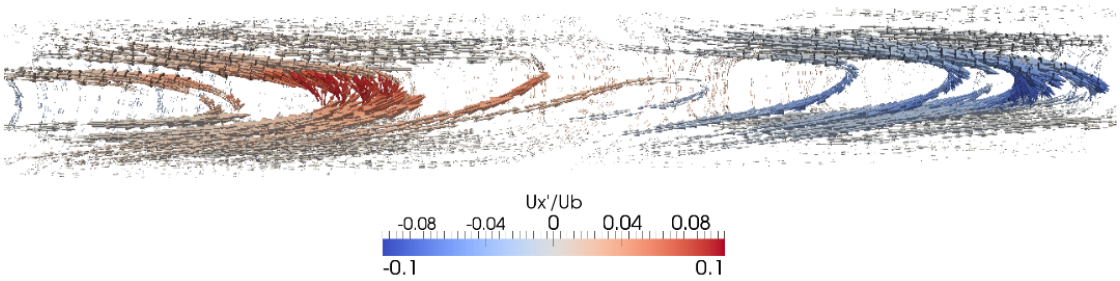

Figure 6.11: Vector field of the counter-rotating structures at the equidistant plane

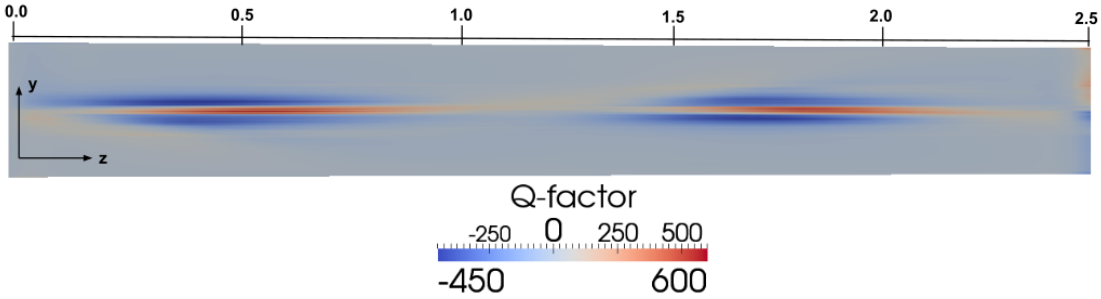

Figure 6.12: Q-factor in the equidistant plane of the gap region

visualizing coherent vortical structures. It is defined as the second invariant of the velocity gradient tensor (Dubief and Delcayre [2000]).

$$Q = -\frac{1}{2}\frac{\partial U_i}{\partial x_j}\frac{\partial U_j}{\partial x_i} = \frac{1}{2}(\Omega_{ij}\Omega_{ij} - S_{ij}S_{ij}) \tag{6.2}$$

where, Ω_{ij} and S_{ij} are the rotation tensor and rate of strain tensor respectively.

$$\Omega_{ij} = \frac{1}{2}(\frac{\partial U_i}{\partial x_j} - \frac{\partial U_j}{\partial x_i}) \tag{6.3}$$

$$S_{ij} = \frac{1}{2}(\frac{\partial U_i}{\partial x_j} + \frac{\partial U_j}{\partial x_i}) \tag{6.4}$$

At $Q > 0$, vorticity prevails over strain. The Q-factor plot at the equidistant plane is shown in Figure 6.12, and two regions are observed. These regions correspond to the two structures observed in the vector plots. On observing the Q-factor plots alone, incorrect conclusions about the extent of these structures could be drawn. This is due to the fact that the Q-factor is a derivative of the velocity field, and hence it represents only the gradients of the velocity field and not the velocity itself. Although the velocity field is highly three-dimensional, the Q-factor plot shows two-dimensional structures, that too only in the gap region. Hence, it can be concluded that Q-factor is not a suitable technique of visualizing these structures.

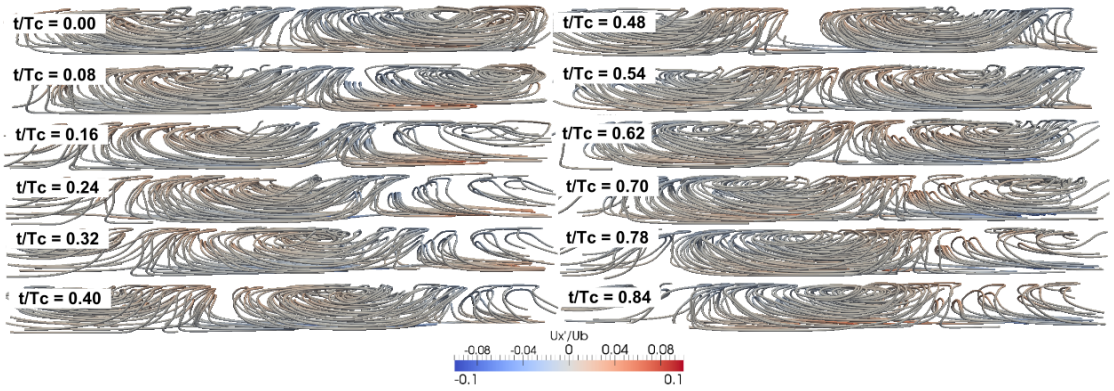

Figure 6.13: Temporal evolution of the streamlines of the resolved velocity field in the y-z plane

The temporal evolution of the streamlines can be seen in Figure 6.13. It can be seen that the structures are extremely stable and are convected with the mean flow. High periodicity can also be observed, suggesting that these structures are quite stable, i.e., there exists an unsteady stable periodic flow.

6.2.2 Temporal Scales of the Structures

The flow visualization leads to very interesting observations pertaining to the three dimensionality, periodicity and stability of the structures. The time-series and frequency spectra studies will substantiate the above findings and a quantification of the temporal and spatial scales of the structures can be obtained. Figure 6.14 shows the time-series of all the velocity components at the center of the gap in the equidistant plane. The periodic nature of the fluctuations observed in Figure 6.13 can be confirmed by the time series. Contrary to the quasi-periodic nature of the fluctuations observed in the experiment, the current results indicate highly periodic structures. This may be due to the use of URANS approach for turbulence modeling. Such high periodicity is also observed in the URANS simulations of Chang and Tavoularis [2012].

The time series of dimensionless spanwise velocity component at different x/D in the equidistant plane is shown in Figure 6.15; the maximum amplitude of fluctuations is observed at the center of the gap. This is consistent with the peak observed in the RMS plot of spanwise resolved velocity fluctuations in Figure 6.5. The periodicity of the flow is maintained even at regions far away from the gap, confirming the three-dimensionality of the structures observed in the vector fields.

The power spectra of the three velocity components is shown in Figure 6.16. The St number corresponding to the peak frequency is calculated to be 0.035 for the spanwise velocity component, and almost twice (0.067) for the other two velocity components. This is expected due to the presence of a y-z symmetry plane. The fluctuations used

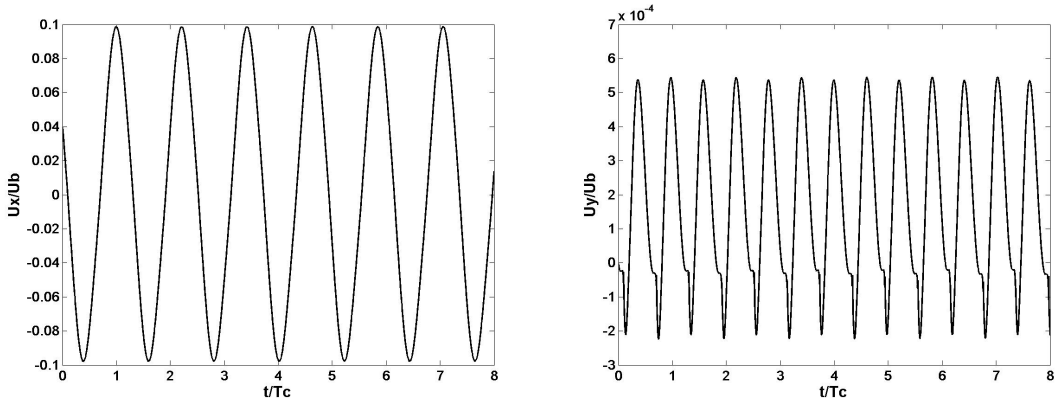

Figure 6.14: Time series of instantaneous velocity components in the equidistant plane, (a)u_x, (b)u_y and (c)u_z

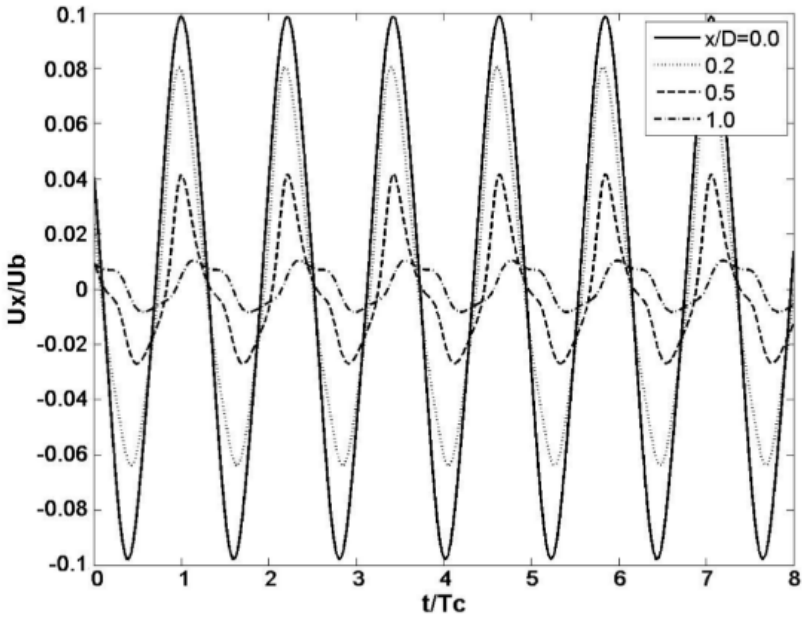

Figure 6.15: Fluctuations of spanwise velocity component at different x/D at the equidistant plane

to determine the power spectra was captured for a much longer time than that used while comparing the results of different turbulence models (Figure 5.14). This was done in order to ascertain the different shapes of the power-spectra between the LRR and $k-\varepsilon$ turbulence models observed in Figure 5.14. It can be observed that the different sub-harmonics of the peak frequency are also observed in the present case, i.e., while using the $k-\varepsilon$ turbulence model. This further substantiates the importance of the longer simulation time required to accurately capture all the dynamics of the flow. The sub-harmonics can be observed power spectra of u_y and u_z as well, reiterating the fact that the structures observed are highly periodic.

6.2.3 Velocity and Spatial Scales of Structures

The formalization of the coherent structures can be done by defining the associated spatial and velocity scales. Figure 6.17 shows the space-time correlation of u'_x as a function of the time delay. High correlation values indicate clear spatial periodicity, associated with the large three-dimensional structures observed in the flow visualization.

Figure 6.18 shows the time delay corresponding to the maximum correlation as a function of $\Delta z/D$. The slope of this line gives the convection speed, U_c of the structures.

The streamwise spacing, λ/D is around 23, which is associated to the two counter-rotating sledge shaped three dimensional velocity fields observed in the flow visualization. The parameters, St, λ and U_c were also computed at other points in the cross-section, and

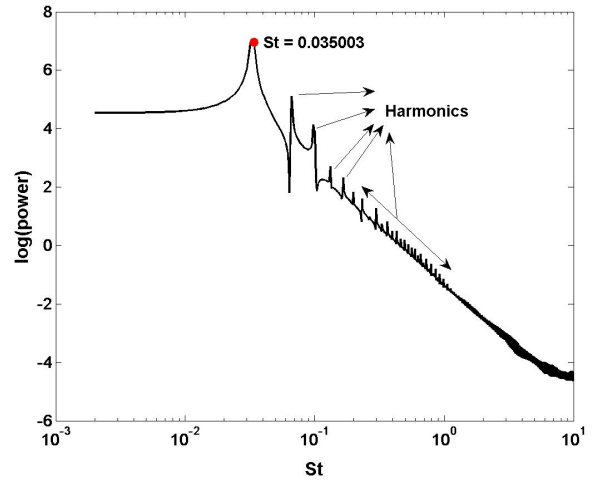

(a)

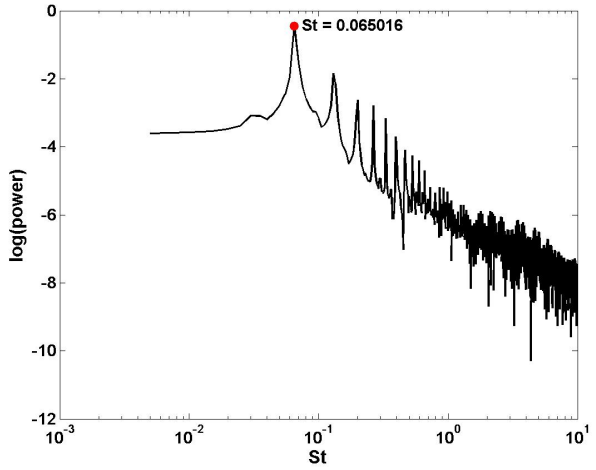

(b)

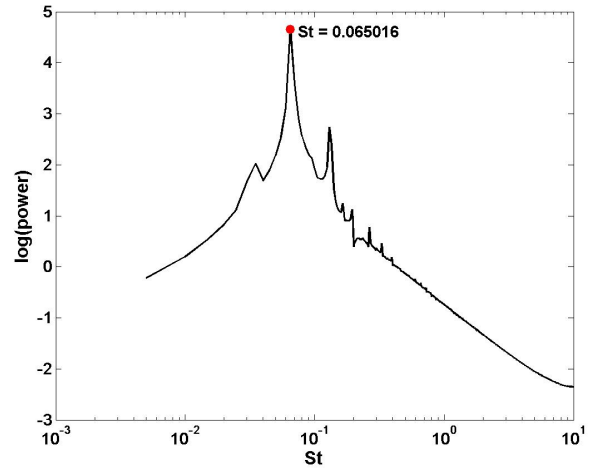

(c)

Figure 6.16: Power spectra of the instantaneous velocity components in the equidistant plane at x/D = 0 , (a)u_x, (b)u_y and (c)u_z

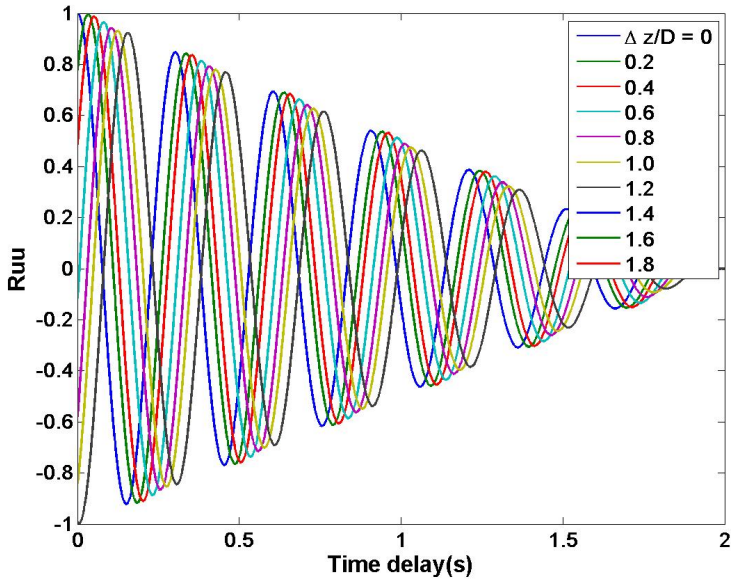

Figure 6.17: Space-time correlation as a function of time delay at various streamwise locations

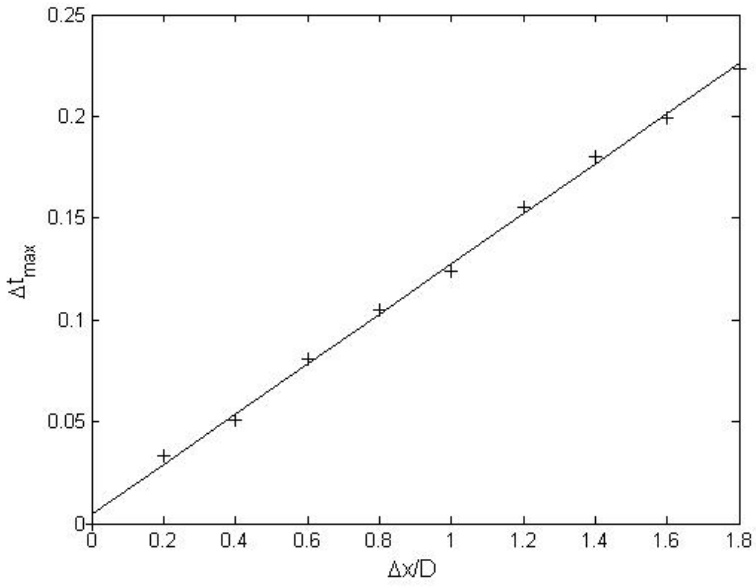

Figure 6.18: Time delay corresponding to the maximum correlation as a function of streamwise location

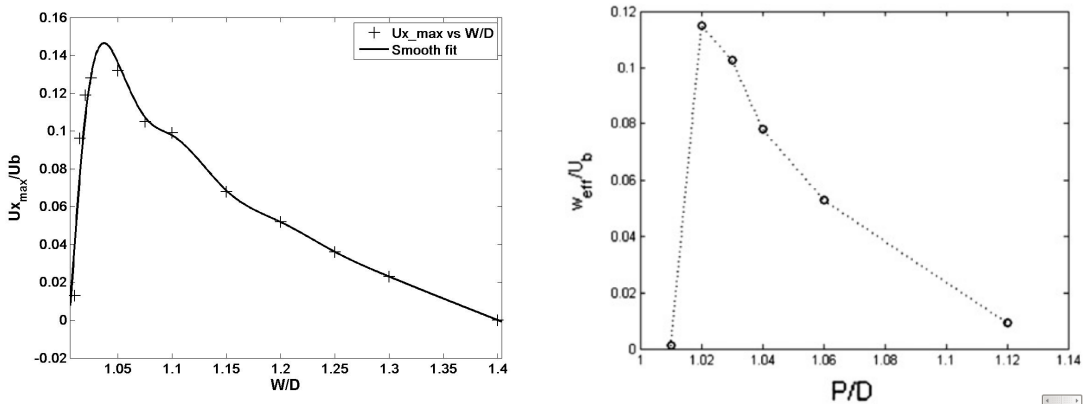

(a) (b)

Figure 6.19: Maximum spanwise velocity (Ux/Ub) as a function of the gap size, (a) Present simulations and (b) simulations of Yan et al. [2012b]

similar values to that at the center of the gap were obtained. This further substantiated the fact that the fluctuations are highly three-dimensional and exist as large structures encompassing the entire flow domain.

6.3 Effect of Gap Size on Coherent Structures

Simulations were carried out at various gap sizes to determine its effect on the coherent structures. The results of simulations at gap sizes $W/D < 1.025$ are subject to errors in turbulence modeling in the near gap region. Due to the usage of wall functions in all the simulations, the requirement of having the first computational cell in the log-log layer ($y^+ > 30$) could not be achieved for $W/D < 1.025$. The maximum (at the center of the gap) spanwise velocity fluctuations as a function of the gap size is shown in Figure 6.19a. Similar study was done on the experimental geometry of Krauss and Meyer [1996, 1998] (shown in Figure 3.5c) by Yan et al. [2012b] and the results obtained are plotted (Figure 6.19b) alongside those of the present simulations.

It can be seen that the maximum fluctuations occur at gap-size of $W/D = 1.04$. This is defined as the critical gap-size, either side of which the maximum velocity decreases. The critical gap size in case of Yan et al. [2012b] was around 1.03, which is comparable to the present case. It is interesting to note that low intensity fluctuations are observed even at high gap sizes such as $W/D = 1.30 - 1.40$. Mahmood [2011] also observed structures at high gap sizes such as 1.40. The maximum fluctuations decrease at a higher rate when going from the critical gap size to zero gap in comparison to the trend observed when the gap size is increased above the critical gap size.

The St number of the flow pulsations as a function of the gap size is shown in

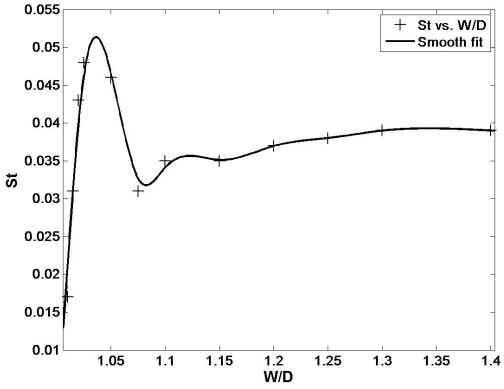

Figure 6.20: Strouhal number of coherent structures at the center of the gap ($St = f_p D/U_b$) as a function of the gap size

Figure 6.20. The maximum St corresponds to the critical gap size of $W/D = 1.04$. The St first increases to the maximum value, followed by a short decrease till a gap size of $W/D = 1.10$, after which it becomes constant. This indicates the presence of two different mechanisms (A and B) responsible for the flow fluctuations. Mechanism A is responsible for the fluctuations at gap sizes lower than $W/D = 1.10$, which is related to the presence of two regions of wide and narrow gaps. Whereas mechanism B is prevalent at higher W/D ratios, where the velocities in the open sub-channel and gap region are not very different. This suggests that the fluctuations are observed due to the complex distribution of the Reynolds-stresses as a result of the geometry.

The power spectra comparison for various gap sizes was also done (not shown here) and an order of magnitude difference in the peak power was observed on reduction of the gap size, $W/D < 1.15$. The decrease in the peak power in the spectra was also observed by Guellouz and Tavoularis [2000a] in their experiments.

The convection velocity, U_c and streamwise spacing, λ of the coherent structures for different gap sizes is shown in Figures 6.21 and 6.22 respectively. Similar to the St plot (Figure 6.20), at after a gap size of $W/D = 1.10$, there is no substantial change in the values of both U_c and λ. At larger gap-sizes, the U_c approaches the bulk velocity, which is consistent with characteristics of mechanism B described above. Both the profiles are similar to the experimental findings of Guellouz and Tavoularis [2000a].

When the gap size is close to zero, the boundary layers at the walls next to gap overlap, leading to high viscous effects in the region. This prevents the formation of any structures as the velocity is almost zero. Whereas, a similar effect should be observed at large gap-sizes when the flow is expected to behave like a fully-developed turbulent channel flow. Interestingly, this is not the case and the structures continue to exist at large gap-sizes of $W/D = 1.30 - 1.40$. A critical gap-size of $W/D = 1.04$ is observed, at which the fluctuations are the maximum. A cut-off gap size of $W/D = 1.10$ is defined,

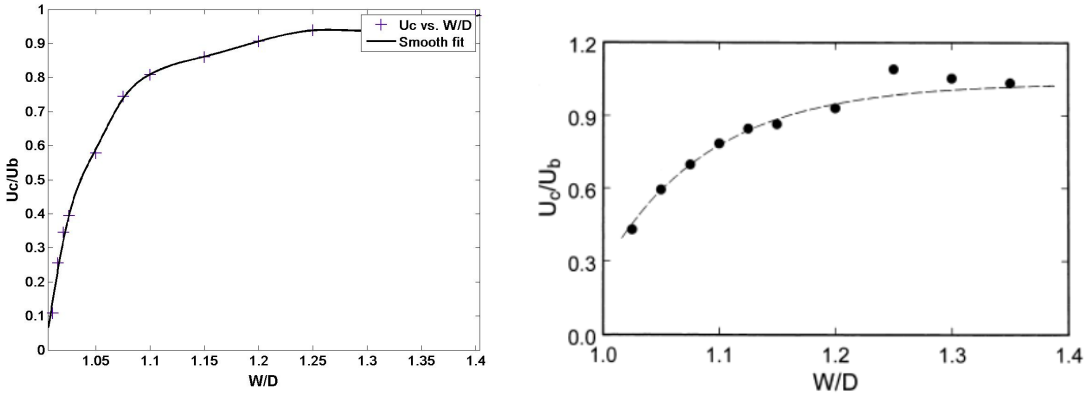

(a) (b)

Figure 6.21: Average convection velocity of coherent structures (Uc/Ub) as a function of the gap size, (a) Present simulations and (b) experiments of Guellouz and Tavoularis [2000a]

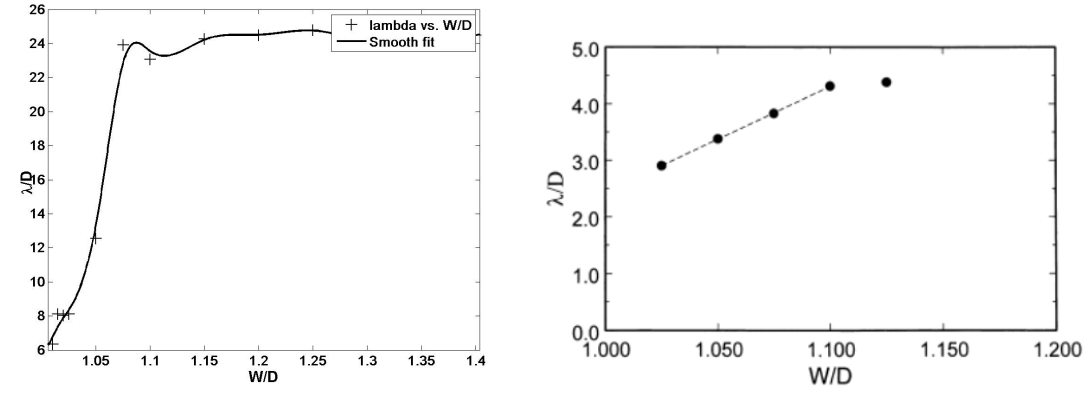

(a) (b)

Figure 6.22: Streamwise spacing of coherent structures (λ/D) as a function of the gap size, (a) Present simulations and (b) experiments of Guellouz and Tavoularis [2000a]

which is roughly the transition point between the two different mechanisms present. Below the cut-off gap-size the mechanism A dominates, and mechanism B plays a more important role above that.

6.4 Summary and Discussion

The dynamics of the flow, including the time-averaged velocity profiles, fluctuations and turbulence kinetic energy were discussed. The peaks in both the RMS of velocity fluctuations and kinetic energy indicated the presence of additional dynamics in the near-gap region. Upon visualization of the resolved velocity field, large three-dimensional sledge shaped structures were observed. These structures extended the entire length of the domain, and formed a pair of two interacting counter-rotating sledges. The spanwise component of time-averaged velocity and RMS of the spanwise velocity fluctuations had maximum values in the center of the gap, and decreased gradually while moving away from the gap. Whereas, the peaks in the axial component of the RMS of velocity fluctuations and the turbulence kinetic energy profiles were located at two core regions on either side of the gap in the open sub-channel.

Another interesting feature of these structures is the high periodicity and stability. After their formation, and stabilization upon initial transients, these structures stay as they are. The instantaneous velocity fluctuations profiles were quite sinusoidal in nature with a distinct dominant frequency. The power-spectra clearly showed the presence of the additional sub-harmonics. This leads to a conclusion that these three-dimensional stable structures are not turbulence structures, which are highly unstable and have a short life-time.

The effect of the gap size on these structures was also investigated. A critical gap size of $W/D = 1.04$ was obtained at which intensity of the flow pulsations are the maximum. Both the maximum spanwise velocity and the St number occurred at this gap size. The profiles of St, U_c and λ indicated the presence of these structures at very large gap sizes of $W/D = 1.30 - 1.40$ as well. Two competing mechanisms (A and B) leading to the formation of these structures were identified, and a cut-off gap size of $W/D = 1.10$ was observed as the transition point between the domination of these two mechanisms.

Various mechanisms leading to the formation of the structures was discussed in Chapter 3. The similarity to the Kelvin-Helmholtz instability mechanism has been cited extensively in the literature. Counter-rotating structures were also observed in the laminar flow experiments on Gosset and Tavoularis [2006] in the same geometry as used in the current simulations. A mechanism similar to that of the von Kármán vortex street which is formed in a wake region behind a cylinder is cited.

The current results clearly indicate the presence of more than one mechanism present.

The mechanism A, which dominates at lower gap-sizes could be similar to the Kelvin-Helmholtz instability. Whereas, the mechanism B probably suggests that the observed flow is akin to that of a complex-fluid, which stems from the complex Reynolds-stress profiles due to the geometry itself.

Chapter 7

Simulations of a Passive Scalar

The studies on the effect of the coherent structures on the transport and mixing of a passive scalar are reported in this chapter. The energy equation is solved along with the momentum and continuity equations. The temperature field acts as a passive scalar. Both fully developed and developing passive scalar fields are studied. The former gives an indication of the transport and fluctuations caused due to passive scalar, whereas the developing scalar field simulations indicate the effect on the mixing. A comparison of the effect of the coherent structures with that of turbulent diffusion is also done, and the relative contributions of each are estimated.

In both the cases the flow is fully developed. The simulations were carried out using the same settings that were used to study the hydrodynamics.

7.1 Decomposition of Temperature Fluctuations

The variance of the total temperature fluctuations (ϑ) is divided into resolved (ϑ_{res}) and non-resolved ϑ_{nr} components. The resolved fluctuations are due to the presence of the coherent structures, whereas the non-resolved fluctuations are caused due to turbulence.

$$\overline{\vartheta^2} = \overline{\vartheta^2_{res}} + \overline{\vartheta^2_{nr}} \tag{7.1}$$

The resolved component, $\overline{\vartheta^2_{res}}$, is given as

$$\overline{\vartheta^2_{res}} = \overline{(T - \overline{T})^2} \tag{7.2}$$

where, $\overline{T}$ is the time-averaged local temperature. As the URANS simulations do not explicitly calculate the unresolved temperature fluctuations, a mixing-length model assumption is used. The non-resolved temperature fluctuations in each of the three directions can be approximated as

$$T'_x \sim l\frac{\partial T}{\partial x} \tag{7.3}$$

$$T'_y \sim l\frac{\partial T}{\partial y} \tag{7.4}$$

$$T'_z \sim l\frac{\partial T}{\partial z} \tag{7.5}$$

The mixing-length, l is given in terms of the turbulence kinetic energy and dissipation rate as

$$l = \frac{k^{3/2}}{\varepsilon} \tag{7.6}$$

The variance of the total non-resolved temperature fluctuations can hence be approximated as

$$\overline{\vartheta^2_{nr}} = \frac{C_\mu}{C_{\nu 1} Pr_t}\frac{\overline{k}^3}{\overline{\varepsilon}}\left[(\frac{\partial \overline{T}}{\partial x})^2 + (\frac{\partial \overline{T}}{\partial y})^2 + (\frac{\partial \overline{T}}{\partial z})^2\right] \tag{7.7}$$

with the constant of proportionality $C_\mu/(C_{\nu 1} Pr_t)$ similar to the derivation in Chang and Tavoularis [2006], where $C_\mu = 0.09$, $C_{\nu 1} = 0.62$ and $Pr_t = 0.85$.

7.2 Fully Developed Passive Scalar Field

In order to study the transport of a passive scalar, simulations were done in a fully developed temperature field. Two heating modes were investigated:

- Case 1: constant wall-temperature with $T_{rod} = 335$ K and $T_{wall} = 298$ K.
- Case 2: constant heat flux at walls with $q_{rod} = 100$ W/mK and $q = 0$ at the other walls (i.e., zero gradient boundary condition is applied to the other walls)

The non-dimensionless time-averaged temperature difference is defined as

$$\overline{\theta(x,y)} = \frac{\overline{T(x,y)} - \overline{T_b(z)}}{\overline{T_{rod}(z)} - \overline{T_b(z)}} \tag{7.8}$$

In Case 2, the time-averaged temperature difference is represented by $\overline{\tilde{\theta}}$.

7.2.1 Time-Averaged Flow Parameters

The contours of $\overline{\theta}$ and $\overline{\tilde{\theta}}$ for the heating modes on the cross-plane are given in Figure 7.1, along with those of the simulations of Chang and Tavoularis [2006]. The contour shapes and values for all the four cases are similar. The near-gap contour values are higher in the present simulations, and this can be attributed to periodic-boundary conditions in

the simulations. High temperature zones can be observed near the gap. It can be also seen that the contours in the near-gap region are different for the two cases.

The rest of the results reported here are those of Case 1 (constant wall temperature) alone. The spanwise variation of time averaged dimensionless temperature difference, $\overline{\theta}$ at the equidistant plane is shown for in Figure 7.2. A significant increase is observed in the gap region, with the maximum at the center of the gap. This due to the presence of the two walls (bottom wall, where $\overline{\theta} = 0$ and the rod where $\overline{\theta} = 1$) close to each other in the gap region, and $\overline{\theta}$ is approximately 0.5.

To investigate the contribution of the coherent structures, the iso-contours of the dimensionless standard deviation of resolved ($\sqrt{\overline{\vartheta_{res}^2}}$) and un-resolved ($\sqrt{\overline{\vartheta_{nr}^2}}$) temperature fluctuations are plotted in Figures 7.3b and 7.4b respectively. This is compared with the simulation results of Chang and Tavoularis [2006], and similarities are observed in the contours of the un-resolved fluctuations. The resolved fluctuations on the other hand, extend more towards the open channel region than those observed by Chang and Tavoularis [2006], probably due to flow developmental reasons. This finding is similar to the contours of turbulence kinetic energy, which extended very much into the open channel region as discussed in Section 5.5.

The contribution of the coherent structures towards to the total temperature fluctuations of the present simulations along with those observed by Chang and Tavoularis [2006] is shown in Figure 7.5. Similar to the contours of ($\sqrt{\overline{\vartheta_{res}^2}}$), the contribution of coherent structures extend deep into the channel region. This is consistent with the three dimensional nature of the coherent structures determined in the Section 6.2.1. The contribution towards total fluctuations is almost 50% in the near gap region, and the maximum occurs on either side of the gap and not at the center. The contribution at the center is about 15%, which is consistent with the simulations of Chang and Tavoularis [2006].

7.2.2 Transient Analysis

Both the time-averaged and instantaneous (snap-shot) temperature difference are plotted as a function of streamwise distance in Figure 7.6. After the initial transient period, the time-averaged difference does not depend on the streamwise distance, whereas fluctuations can be observed in the instantaneous difference plot. These fluctuations are very similar to that of the spanwise velocity fluctuations (Figure 6.14). This clearly indicates that the transport of the passive scalar takes place via the coherent structures.

The iso-surfaces of the instantaneous resolved temperature fluctuations ($T - \overline{T}$) are shown in Figure 7.7. Three-dimensional structure of the iso-surfaces can be observed, and they extend all the way into the open-sub-channel. This is very consistent with the contours of $\sqrt{\overline{\vartheta_{res}^2}}$, substantiating the observation that the fluctuations are caused due to

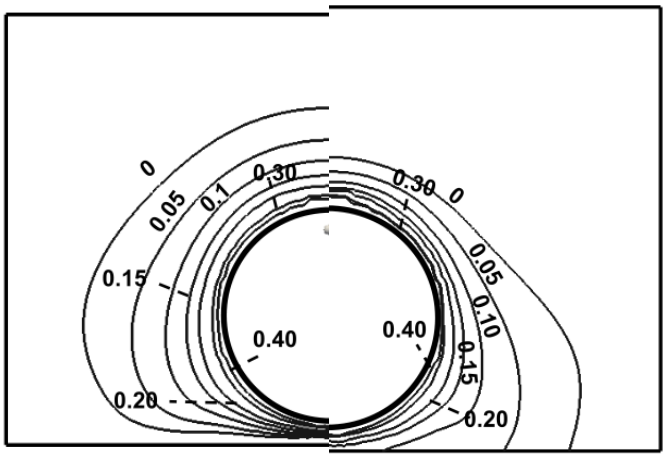

(a) (b)

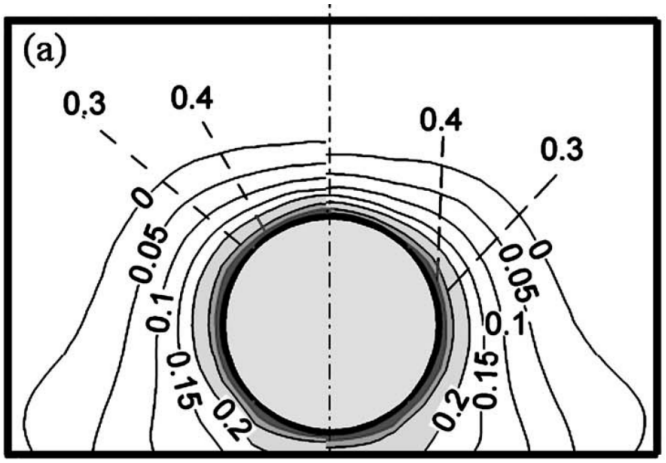

(c)

Figure 7.1: Contours of dimensionless temperature difference at the cross section, (a) Case 1 - Constant temperature at the walls, (b) Case 2 - Constant heat flux at the walls and (c) Chang and Tavoularis [2006] simulations, left side plot is the uniform-rod temperature case and right side the constant rod heat flux case

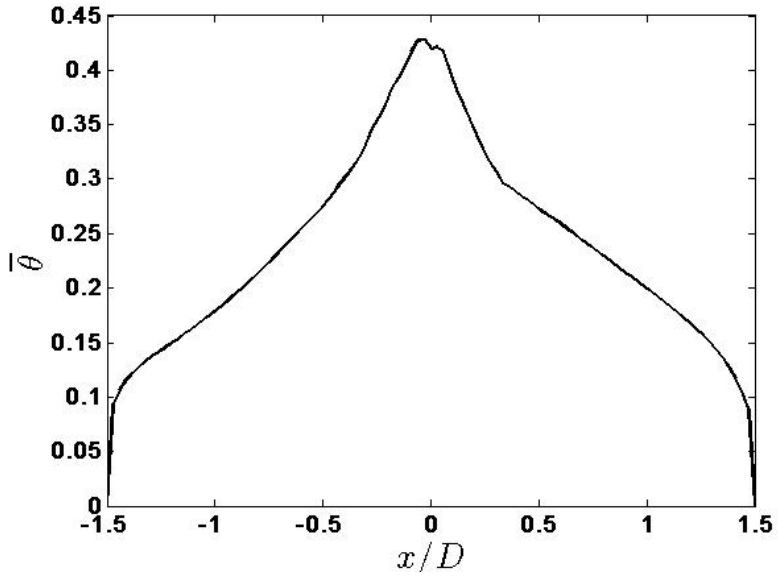

Figure 7.2: Spanwise variation of the $\overline{\theta}$ at the center of the gap in the equidistant plane

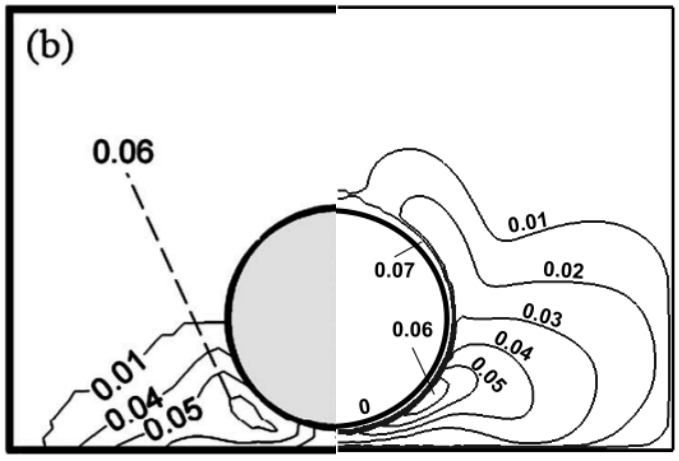

(a) (b)

Figure 7.3: Contours of dimensionless resolved temperature fluctuations $\sqrt{\overline{\vartheta_{res}^2}}/(\overline{T_{rod}} - \overline{T_b})$ at the cross section, (a) Chang and Tavoularis [2006] simulations and (b) present simulations, Case 1 - both with constant temperature at the walls

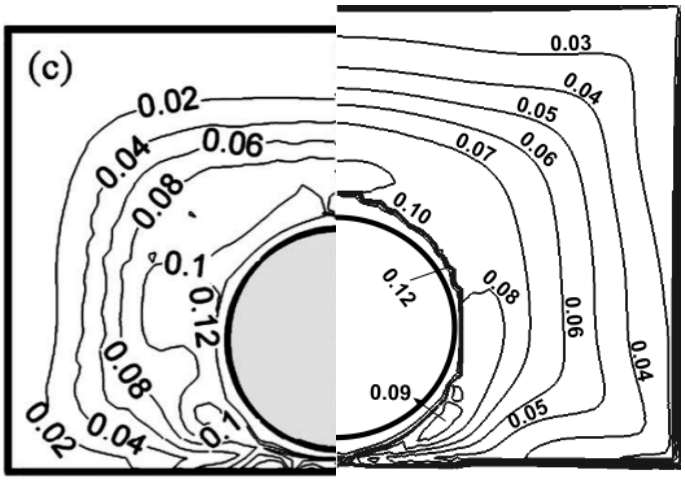

(a) (b)

Figure 7.4: Contours of dimensionless un-resolved temperature fluctuations $\sqrt{\overline{\vartheta_{nr}^2}}/(\overline{T_{rod}} - \overline{T_b})$ at the cross section, (a) Chang and Tavoularis [2006] simulations and (b) present simulations, Case 1 - both with constant temperature at the walls

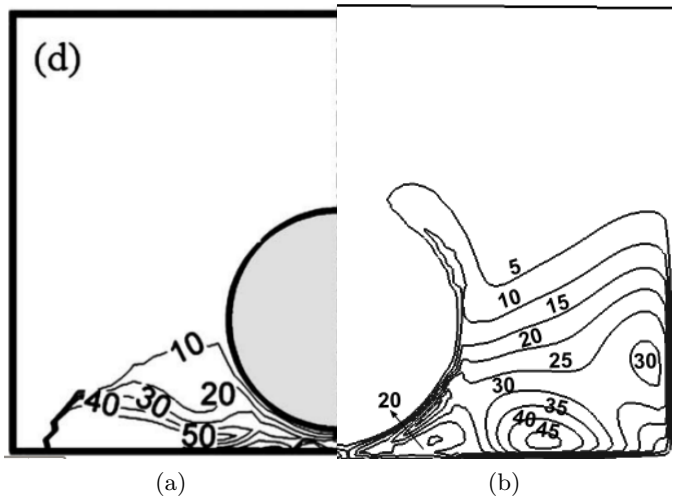

(a) (b)

Figure 7.5: Contours of the contribution of coherent temperature fluctuations $\overline{\vartheta_{res}^2}/\overline{\vartheta^2}$ (in %) at the cross section, (a) Chang and Tavoularis [2006] simulations and (b) present simulations, Case 1 - Constant temperature at the walls

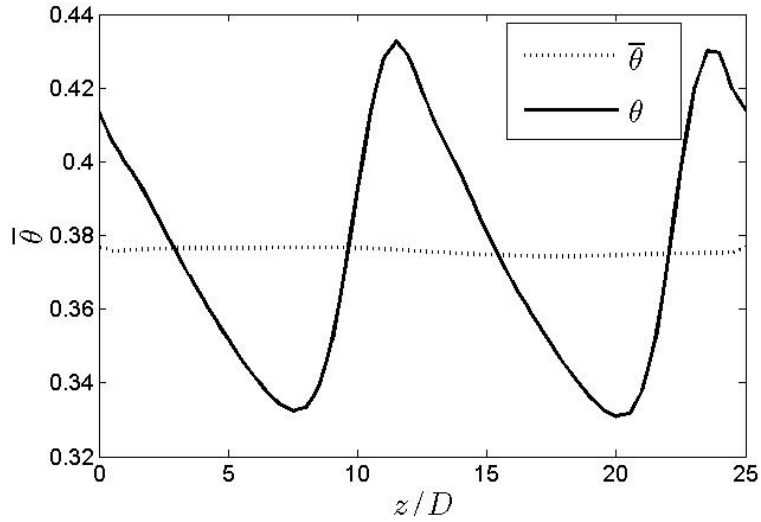

Figure 7.6: Streamwise variation of the θ and $\overline{\theta}$ at the center of the gap

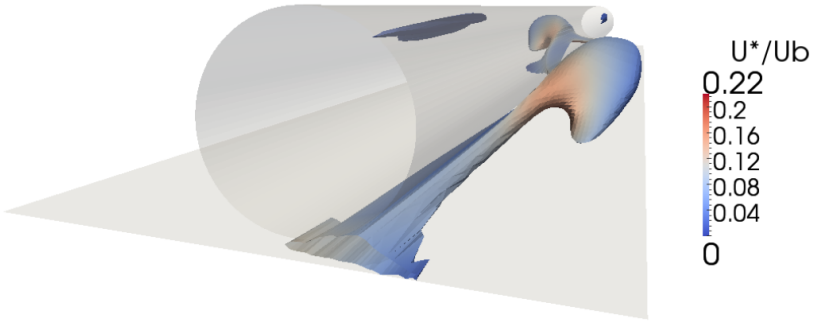

Figure 7.7: Iso-surface of resolved temperature ($\theta' = \theta - \overline{\theta}$), $\theta' = 0.01$ colored by the magnitude of resolved velocity vector

the coherent structures. It can be also noticed that the iso-surfaces are present as a pair, with each present on either side of the gap. The coherent structures were also observed in the form of three-dimensional counter-rotating sledge shaped pairs (Figure 6.10)

The power spectra of the instantaneous temperature fluctuations is shown in Figure 7.8, and the St corresponding to the peak frequency is twice that of the St associated with that of spanwise velocity fluctuations. This is expected due to the presence of a y-z symmetry plane, and the passive scalar will be transported twice across the gap compared to the spanwise velocity. The convection velocity, U_c and streamwise spacing, λ of the structures of the resolved temperature fluctuations were found to be exactly similar to that of the spanwise velocity fluctuations.

From both the contour plots of the time-averaged resolved temperature, and the analysis of the instantaneous profiles, it can be concluded that the coherent structures play a very important role in the transport of passive scalar. Their contribution is almost

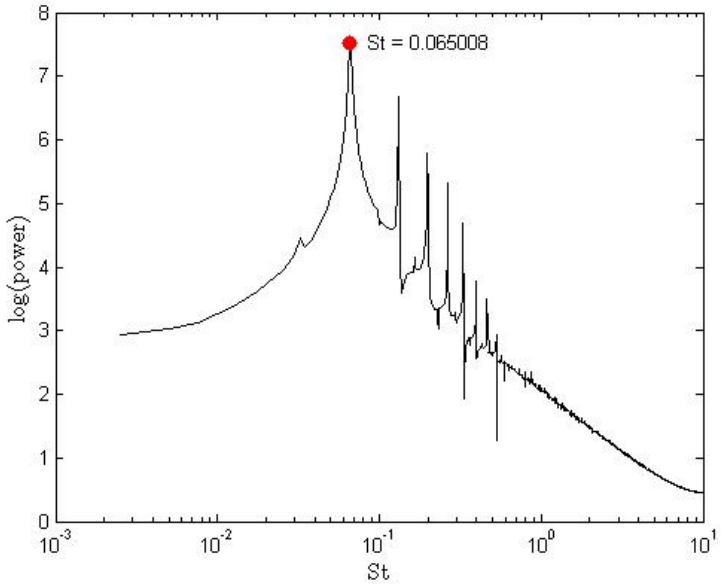

Figure 7.8: Power spectra of the instantaneous temperature fluctuations at the equidistant plane

50% in the near-gap regions, with decreasing effect away from it.

7.3 Developing Passive Scalar Field

In the previous section, the contribution of coherent structures towards the total temperature fluctuations was analyzed. In this section, the effect of the coherent structures on the mixing characteristics in a developing passive-scalar field is studied. It should be noted here that a highly fluctuating temperature field will not necessarily cause good mixing. As the resolved T' fields were illustrative in observing the transport of the passive scalar, the resolved $u'T'$ field will help in determining the mixing.

Figure 7.9 shows the inlet cross-section of the channel. A higher temperature of $T_1 = 310$ K was maintained in the small rectangular region shown in the figure, and the rest of the plane has an inlet value of $T_2 = 298$ K. The entire flow domain was initialized with $T_b = 298$ K. The higher temperature T_1 will be convected downstream, and a more uniform temperature distribution is expected at the end of the channel. This is expected due to the presence of both turbulent diffusion and coherent structures.

Re-writing the URANS equations of the temperature field from Equations 2.12 and 2.22 results in:

$$\frac{\partial T}{\partial t} + u_j \frac{\partial T}{\partial x_j} = (\alpha + \alpha_t) \frac{\partial^2 T}{\partial {x_j}^2} \tag{7.9}$$

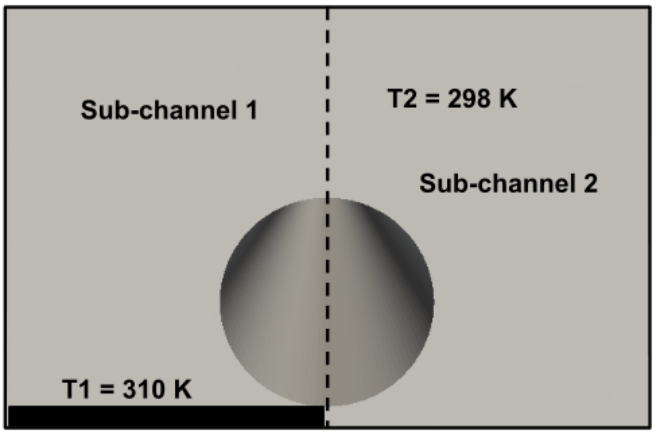

Figure 7.9: Inlet cross-section of the domain showing the two temperature zones, black denotes $T_1 = 310$ K and grey is $T_2 = 298$ K

where α_t is the turbulent diffusivity, defined as

$$\alpha_t = \frac{\nu_t}{Pr_t} \tag{7.10}$$

The temperature, velocity and turbulence diffusivity are divided into a time-averaged component and a resolved fluctuation component.

$$T = \langle T \rangle + T' \tag{7.11}$$
$$u = \langle u \rangle + u' \tag{7.12}$$
$$\alpha_t = \langle \alpha_t \rangle + \alpha_t' \tag{7.13}$$

Substituting the above expressions into Equation 7.9 and considering that the turbulence diffusivity is much higher than the molecular diffusivity ($\alpha_t \sim O(10^{-3})$ and $\alpha \sim O(10^{-5})$), hence, $\alpha_t + \alpha \sim \alpha_t$, the equation reduces to:

$$\frac{\partial}{\partial x_j}\left[\overline{u_j}\,\overline{T} + \langle u_j' T' \rangle\right] = \overline{\alpha_t}\frac{\partial^2 \overline{T}}{\partial x_j^2} + \langle \alpha_t' \frac{\partial^2 T'}{\partial x_j^2} \rangle \tag{7.14}$$

The $\langle u_j' T' \rangle$ term can be written as:

$$\langle u_j' T' \rangle \sim \sqrt{\langle u_j'^2 \rangle \langle T'^2 \rangle}\,\rho_{uT} \tag{7.15}$$

where ρ_{uT} is the correlation coefficient, with values ranging from -1 to 1.

In the cross-section of the channel $\overline{u_j}\,\overline{T} = 0$. Hence, a comparison between the resolved component $\sqrt{\langle u_j'^2 \rangle \langle T'^2 \rangle}$ and the time-averaged $\overline{\alpha_t}\partial\overline{T}/\partial x_j$ will give a measure of the relative contribution of the coherent structures and the mean turbulent diffusion.

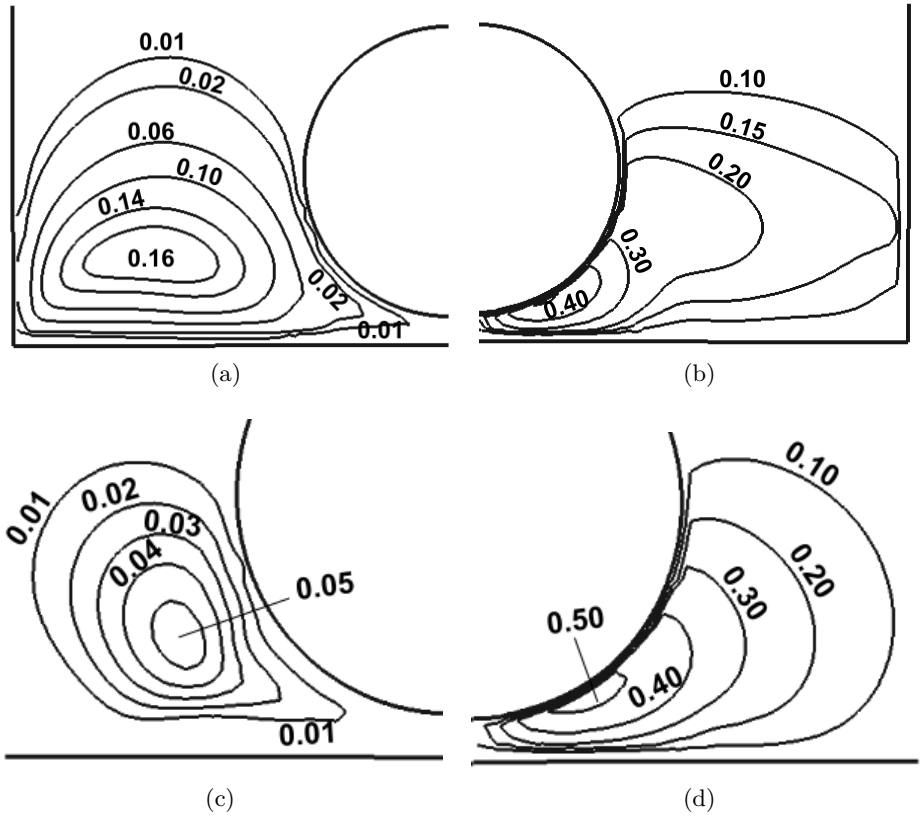

Figure 7.10: Contours at the cross-section plane of (a) $\overline{\alpha_t}\partial\overline{T}/\partial y$ at sub-channel 1 (b) $\sqrt{\langle u_y'^2\rangle\langle T'^2\rangle}$ at sub-channel 1, (c) $\overline{\alpha_t}\partial\overline{T}/\partial y$ at sub-channel 2 and (d) $\sqrt{\langle u_y'^2\rangle\langle T'^2\rangle}$ at sub-channel 2

The exact comparison will depend on the values of ρ_{uT} and $\langle\alpha_t'\partial^2 T/\partial x_j^{2'}\rangle$. However, a qualitative understanding of the possible importance of the coherent structures can be obtained here.

Figure 7.10 shows the contours of $\sqrt{\langle u_y'^2\rangle\langle T'^2\rangle}$ and $\overline{\alpha_t}\partial\overline{T}/\partial y$ for both the sub-channels at the cross-section plane. It can be seen that the values of the resolved component are higher by a factor of almost 2.5-10. The maximum of the resolved component is located near the center of the gap, whereas that of the time-averaged heat-flux is in the open sub-channel. If the values of ρ_{uT} are of the order 0.1-0.5, then the contribution of $\langle u_j'T'\rangle$ associated with the coherent structures and the turbulent diffusion are almost equal.

It can be clearly concluded that the contribution of the resolved component (hence coherent structures) is significant and cannot be neglected. This is consistent with the earlier findings related to the resolved turbulence kinetic energy and the transport due to coherent structures, where the magnitude of the kinetic energy of the coherent structures was higher than the kinetic energy of turbulence near the gap region, with high turbulence kinetic energy far away from the gap.

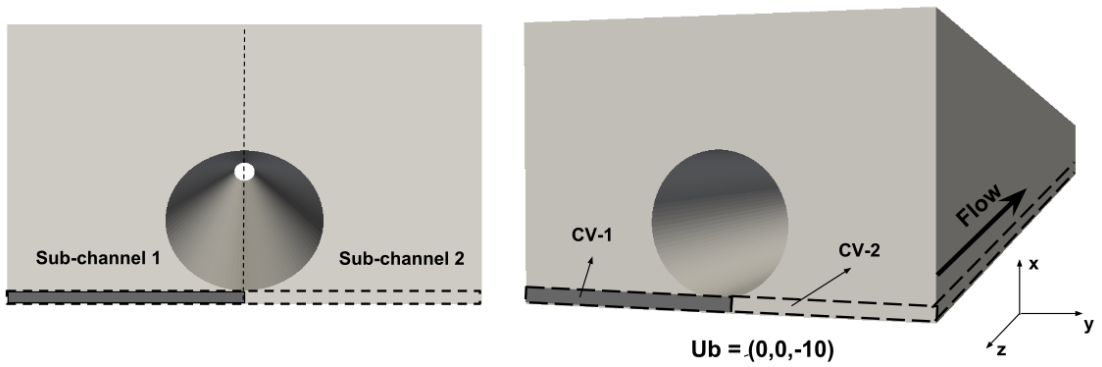

Figure 7.11: Control volumes

An energy balance is done over the control volumes shown in Figure 7.11, in order to analyze the contribution of mixing due to turbulent diffusion and coherent structures.

All the fluxes are shown in Figure 7.12, and the net energy balance is:

$$\begin{aligned}\int(\overline{u_z}\overline{T})_{outlet}dA_1 - \int(\overline{u_z}\overline{T})_{inlet}dA_1 &= \int\left(\overline{\alpha_t}\frac{\partial\overline{T}}{\partial y} + \langle\alpha_t'\frac{\partial T'}{\partial y}\rangle\right)dA_2 \\ &\quad + \int\left(\overline{\alpha_t}\frac{\partial\overline{T}}{\partial x} + \langle\alpha_t'\frac{\partial T'}{\partial x}\rangle\right)dA_3 \qquad (7.16)\end{aligned}$$

where the streamwise diffusion at the outlet and inlet is neglected with respect to convection. The total heat-flux can be represented as a sum of the mean turbulent diffusion q_{diff} and the diffusion due to resolved components (q_{res})

$$q_{diff} = \int\overline{\alpha_t}\frac{\partial\overline{T}}{\partial y}dA_2 + \int\overline{\alpha_t}\frac{\partial\overline{T}}{\partial x}dA_3 \qquad (7.17)$$

$$q_{res} = \int\langle\alpha_t'\frac{\partial T'}{\partial y}\rangle dA_2 + \int\langle\alpha_t'\frac{\partial T'}{\partial x}\rangle dA_3 \qquad (7.18)$$

$$q_t = q_{diff} + q_{res} \qquad (7.19)$$

The energy balance equation reduces to,

$$\int(\overline{u_z}\overline{T})_{outlet}dA_1 - \int(\overline{u_z}\overline{T})_{inlet}dA_1 = q_{diff} + q_{res} \qquad (7.20)$$

In the above equation, all the terms except q_{res} are known, hence the relative contribution due to the diffusion and resolved (or coherent structures) components can be determined. This was done for both the control-volumes. In control volume 1, which is a part of sub-channel 1, the contribution due to turbulent diffusion is twice as large as that of the coherent structures. Whereas in the control volume 2, the coherent structures

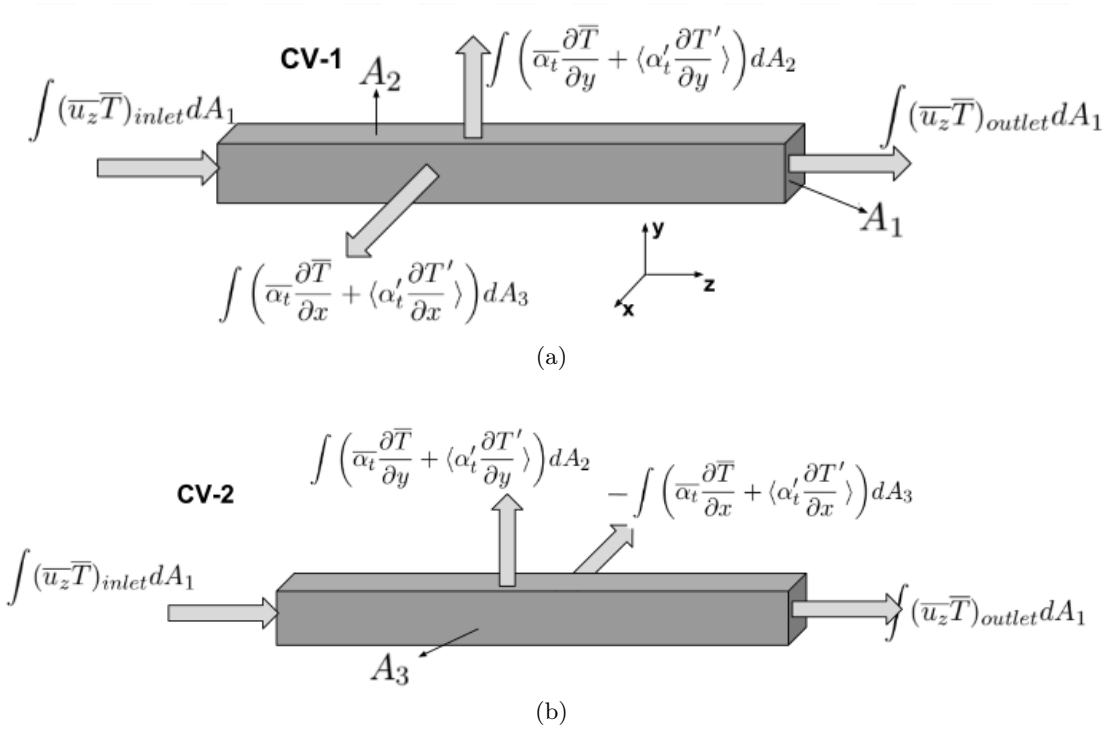

Figure 7.12: Schematic of the two control volumes and all the associated heat fluxes

contribution is 1.5 times larger than that of turbulent diffusion. This once again substantiates the finding that both turbulent diffusion and coherent structures have significant contribution towards the total mixing.

7.4 Summary and Discussions

The simulations with a passive scalar have led to interesting conclusions regarding the contribution of coherent structures towards their transport and mixing. The developed passive scalar field simulations with periodic boundary conditions was done to predict the effect of coherent structures on the transport of the temperature field. Whereas the developing passive scalar field simulations were done to analyze the mixing effect of coherent structures.

In the fully developed scalar field simulations with periodic boundary conditions, it was observed that the effect of the coherent structures on the temperature fluctuations extended all the way up to the open sub-channel region, with the maximum resolved temperature fluctuation occurring on either side of the gap, and not in the gap center. The contour profiles were similar to those of the kinetic energy of resolved velocity fluctuations and the kinetic energy due to turbulence. The instantaneous temperature fluctuations were highly periodic, which was similar to the velocity fluctuations observed

before. This clearly suggested that the temperature fluctuations were caused due to the presence of coherent structures.

Highly three-dimensional structures of the iso-surface of resolved temperature field were observed, which was consistent with the contour plots of the coherent component of the temperature fluctuations. Hence, it was concluded that coherent structures significantly contribute towards the total fluctuations. The effect was not only present in the narrow-gap region, but also in the open sub-channel.

The developing passive scalar field simulations were done in order to analyze the effect of coherent structures on the mixing characteristics. A high temperature source was applied on a rectangular zone on the flow inlet cross-section, and the evolution of the temperature field was studied. It was found that the coherent structures have a significant effect on the total mixing. This was consistent with its effect on turbulence kinetic energy and temperature transport.

In spite of the low frequency of the coherent structures, they have a significant effect on the transport and mixing of the passive scalar. Owing to their large three-dimensional structure, the effect is not only confined to the gap region, but extends all the way into the open sub-channel. The major influence of the structures observed in the relatively simple geometry suggests that there could be an enhanced effect in full-scale rod bundles where multiple gaps are present.

Chapter 8

Conclusions and Recommendations

Three-dimensional, unsteady RANS (URANS) simulations were carried out on a fully developed turbulent flow with periodic boundary conditions in a geometry consisting of an eccentric cylindrical rod inside a rectangular channel. The interesting flow patterns observed in tightly packed rod bundles in a nuclear reactor formed the main motivation of this study. The major conclusions obtained in this work are reported in this chapter. This is followed by the recommendations for future study.

8.1 Conclusions

The main objective of this work was to study the effect of coherent structures on the mean velocity profiles, turbulence quantities, and the transport and mixing of passive scalar. In order to gain confidence on the simulation, an extensive benchmark study was done. In this study, the effect of the computational mesh, length of periodic domain and turbulence model were evaluated. This was followed by the comparisons with the experimental and computational studies in the literature. The simulation settings obtained upon these validation studies were used for further investigation of both the flow dynamics and the transport and mixing of a passive scalar. The major conclusions are presented below.

8.1.1 Benchmark and Validation

Effect of the Length of the Periodic Domain

Due to the presence of periodic fluctuations in the flow, it was important that there was no effect of the length of the periodic domain on them. In other words, the periodicity of

the flow domain should not interfere with that of the flow fluctuations. Simulations were carried out using different lengths: 20D, 25D, 40D, 50D and 100D. The time-averaged profiles of velocity, turbulence kinetic energy, magnitude of velocity fluctuations and the various scales (length, time and velocity) of the fluctuations were compared and no significant differences were observed. It was therefore concluded that a length of 25D is sufficient to capture accurately the various structures occurring in the flow.

Effect of Turbulence Model

Among the various Unsteady RANS turbulence models, a comparison was done between the eddy viscosity $k-\varepsilon$ model and the Reynolds stress model of Launder, Rodi and Reece (LRR). The power spectra of the velocity fluctuations in case of the LRR model represented richer dynamics with multiple sub-harmonics compared to that of the $k-\varepsilon$ model. This indicates that the Reynolds-stress model is probably better suited to predict the intricacies of the flow. However, the primary flow structure was the same in both the models, the time-averaged contours as well as the dominant frequency of the fluctuations were the same. The $k-\varepsilon$ model was chosen for further simulations due to the significantly lower computational cost.

A comparative study was also done to ascertain the effect of the wall treatment on the results. The results of the $k-\varepsilon$ model using wall functions were compared with the available low-Re $k-\varepsilon$ turbulence models in OpenFOAM. These low-Re models employ damping functions to adjust the turbulence quantities in the near-wall region. No significant differences were observed between these low-Re models and the $k-\varepsilon$ model with wall-functions. Hence, the computationally cheaper wall-function $k-\varepsilon$ turbulence model was found acceptable for predicting accurately the various flow characteristics, and used in the rest of this work.

The conclusions obtained here suggest that the large scale fluctuations are associated with the inherent dynamics of the URANS equations in this geometry, and are largely independent of the turbulence model used.

Flow Development and Comparisons with the Literature

Significant differences were observed between the results of the present simulation and those of the benchmark experiment and past simulations reported in the literature. The phenomena of thinning of the shear layer was observed with flow development. For the purpose of the current study, the development in time and space are considered synonymous, with the bulk velocity acting as a transformation between them. A comparison was also done with a recently reported developing flow simulation in space, results of which are much closer to that of the experiment than that of the present simulations with periodic boundary conditions.

The temporal and spatial scales of the flow pulsations were off by a factor of five on comparison with the experiments and literature simulations. Some of the simulation work in the literature has also cited the possibility of the flow still being developing in the benchmark experiments. This has been confirmed in this study. The reported time of flow development for the (supposedly) developed flow simulations were a factor of 3-4 less than the time required in the current simulations. Based on comparisons between the various time-averaged and time-dependent parameters, it is concluded that a significantly longer time than that in turbulent pipe and channel flows is required for flow development in such geometries, and that the number of structures decrease with flow development.

On the basis of these validation studies, it was concluded that the present simulation settings (periodic domain of 25D and wall function based $k - \varepsilon$ turbulence model) accurately predicts both the time-averaged and temporal characteristics of the flow pulsations.

8.1.2 Flow Dynamics

A detailed study on the physics of the flow pulsations was done. The time-averaged axial velocity profile resembled that of a fully developed turbulent channel flow. The peaks in the profiles of the RMS of velocity fluctuations near the gap region indicated the presence of some additional dynamics. The turbulence kinetic energy obtained from the resolved fluctuations was higher than the un-resolved component near the gap region. The contour profiles suggested that the effect of the resolved fluctuations was maximum in the gap region, decreasing gradually away from it.

The flow visualization studies resulted in large three-dimensional sledge shaped structures encompassing the entire flow domain. High periodicity and stability was also observed. They occurred in a pair of two counter-rotating structures. It was also determined that the Q-factor is not a good tool to visualize these structures. Highly misleading two-dimensional patterns were obtained, which was not the case while observing the vector fields.

The temporal, spatial and velocity scales of the structures were defined and determined by the St number, λ, the streamwise spacing, and U_c, the convection velocity. The instantaneous fluctuations were highly periodic in nature, with its maximum magnitude at the center of the gap. However, the St, λ and U_c were constant in the entire cross-section, consistent with the large three-dimensional vector fields of the resolved velocity. These results also clearly suggest that these structures are not *turbulence structures*, which have relatively shorter life-times and are highly unstable.

The effect of the gap size on the structures was studied, and a critical gap size of $W/D = 1.04$ was obtained, at which the intensity of the fluctuations had a maximum

value. With both the decrease and increase in gap-size, the intensity of the fluctuations decreased. However, a very different behavior was obtained for the St, λ and U_c. All these parameters approached a constant value at a gap size of $W/D = 1.10$. The shape of the St curve suggested the presence of two co-existing mechanisms for the formation of the structures, with either of them dominating on the two sides of the cut-off gap size, $W/D = 1.10$.

8.1.3 Transport and Mixing of a Passive Scalar

The energy equation was solved, using temperature as a passive scalar. The transport of the temperature was studied by conducting developed passive scalar field simulations with periodic boundary conditions. A high contribution of the coherent structures towards the total temperature fluctuations was observed near the gap region. The effect of the structures was present at regions away from the gap region, however, the magnitude was highest in the near-gap regions. This was consistent with the profiles of the resolved velocity kinetic energy.

The effect on mixing of the passive scalar was studied by performing developing passive scalar field simulations. The inflow was specified with two different temperature sources, and the downstream temperature distribution was studied. Although exact quantitative comparisons could not be obtained between the relative contributions of turbulent diffusion and coherent structures, an order of magnitude study was done. This concluded that the mixing caused by coherent structures is of the same order of magnitude of that caused by turbulent diffusion.

8.2 Recommendations

Several recommendations are proposed in order to understand in detail the characteristics of the large-scale coherent structures and their respective dynamics.

As it was concluded in this work that the coherent structures are not *turbulence structures*, it will interesting to investigate if they are also present in a laminar flow. Simulations can be done in the same geometry using the turbulence viscosity ν_t, as the effective viscosity of the fluid. This will help in determining whether turbulent flow is a necessary condition for the formation of these structures.

The simulations conducted on different gap-sizes indicate two different mechanisms responsible for the fluctuations. In order to investigate this further, Proper Orthogonal Decomposition of DNS or LES can be performed. Via this, the eigen-value corresponding to the dominant mode can be determined and compared with the instability modes obtained in Merzari et al. [2008]. This will provide information on whether these large-scale structures are somehow associated with the dynamics of instability or whether

they are mostly associated with the dynamics of Reynolds-stresses and eddy viscosity, or both.

In the current simulations, $k - \varepsilon$ model with wall functions was able to predict the primary flow structure fairly accurately and no significant differences were observed when compared to the other turbulence models. If the mechanism of the formation of structures is similar in full-scale rod bundles, this model can be used to accurately predict the mixing characteristics due to coherent structures in a full-scale rod-bundle. Due to the lower computational cost, this can act as an excellent tool for accurate engineering estimates. However, in order to study the detailed physics of the structures, a more complex turbulence model or LES/DNS will probably be needed.

The presence of a large channel-region in the current geometry could be a reason behind the large three-dimensional structures. In a rod-bundle, such regions are not present, and hence it is expected that there will be more number of smaller structures. Also, it will be interesting to study the interaction of the structures formed in different sub-channels.

A more detailed study on the mixing characteristics of coherent structures can be done. In the current work, many approximations were used to compare the contribution of turbulent diffusion and that of structures. The exact values of the terms $\langle u_j' T' \rangle$ and $\langle \alpha_t' \frac{\partial T}{\partial x_j}' \rangle$ can be calculated during run-time. Also, the effect of gap-size on the mixing characteristics can be studied. It is expected that the trend will be similar to the one observed in the flow characteristics.

Bibliography

R.J. Belt. *On the liquid film in inclined annular flow.* Dissertation, Delft University of Technology, 2007.

D Chang and S Tavoularis. Unsteady numerical simulations of turbulence and coherent structures in axial flow near a narrow gap. *ASME Journal of Fluids Engineering*, 127: 458–466, may 2005.

D Chang and S Tavoularis. Convective heat transfer in turbulent flow near a gap. *ASME Journal of Heat Transfer*, 128:701–708, july 2006.

D Chang and S Tavoularis. Simulations of turbulence, heat transfer and mixing across narrow gaps between rod-bundle subchannels. *Nuclear Engineering and Design*, 238 (1):109–123, jan 2008.

Dongil Chang and Stavros Tavoularis. Numerical simulations of developing flow and vortex street in a rectangular channel with a cylindrical core. *Nuclear Engineering and Design*, 243:176–199, feb 2012.

JJ Derksen. Simulations of lateral mixing in cross-channel flow. *Computers & Fluids*, 39(6):1058–1069, 2010.

Yves Dubief and Franck Delcayre. On coherent-vortex identification in turbulence. *Journal of Turbulence*, 1:N11, 2000.

A. Gosset and S. Tavoularis. Laminar flow instability in a rectangular channel with a cylindrical core. *Physics of Fluids*, 18(4):044108, 2006.

M S Guellouz and S Tavoularis. The structure of turbulent flow in a rectangular channel containing a cylindrical rod - part 1 : Reynolds-averaged measurements. *Experimental Thermal and Fluid Science*, 23:59–73, 2000a.

M S Guellouz and S Tavoularis. The structure of turbulent flow in a rectangular channel containing a cylindrical rod part 2 : phase-averaged measurements. *Experimental Thermal and Fluid Science*, 23:75–91, 2000b.

Tsutomu Ikeno and Takeo Kajishima. Analysis of dynamical flow structure in a square arrayed rod bundle. *Nuclear Engineering and Design*, 240(2):305–312, feb 2010.

John Kim, Parviz Moin, and Robert Moser. Turbulence statistics in fully developed channel flow at low reynolds number. *Journal of Fluid Mechanics*, 177:133–166, 1987.

T Krauss and L Meyer. Characteristics of turbulent velocity and temperature in a wall channel of a heated rod bundle. *Experimental Thermal and Fluid Science*, 12:75–86, 1996.

T Krauss and L Meyer. Experimental investigation of turbulent transport of momentum and energy in a heated rod bundle. *Nuclear Engineering and Design*, 180:185–206, 1998.

P.K. Kundu and I.M. Cohen. *Fluid Mechanics 2nd ed.* Academic Press, 2002.

C.K.G Lam and K. Bremhorst. A modified form of the $k - \varepsilon$ model for predicting wall turbulence. *ASME Journal of Fluids Engineering*, 103:456–460, 1981.

B.E. Launder and B.I. Sharma. Application of the energy dissipation model of turbulence to the calculation of flow near a spinning disk. *Letters in Heat and Mass Transfer*, 1: 131–138, 1974.

B.E. Launder, G.J. Reece, and W. Rodi. Progress in the development of a reynolds-stress turbulence closure model. *Journal of Fluid Mechanics*, 68(3):537–566, 1975.

F.S. Lien and M.A. Leshziner. Modelling 2d separation from high-lift aerofoil with non-linear eddy-viscosity model and second-moment closure. *Aeronauatical Journal*, 99 (984):125–144, apr 1995.

Maolong Liu and Yuki Ishiwatari. Unsteady numerical simulations of the single-phase turbulent mixing between two channels connected by a narrow gap. *Nuclear Engineering and Design*, 241(10):4194–4205, oct 2011.

Amer Mahmood. *Single-phase crossflow mixing in a vertical tube bundle geometry An experimental study.* Dissertation, Delft University of Technology, 2011. URL `http://repository.tudelft.nl/view/ir/uuid:61a25a99-06da-4731-9fbb-6479c6865288/`.

E. Merzari and H. Ninokata. Proper orthogonal decomposition of the flow in a tight lattice rod-bundle. *Nuclear Engineering and Design*, 241(11):4621–4632, nov 2011.

E. Merzari, S. Wang, H. Ninokata, and V. Theofilis. Biglobal linear stability analysis for the flow in eccentric annular channels and a related geometry. *Physics of Fluids*, 20:114104, 2008.

Elia Merzari and Hisashi Ninokata. Anisotropic turbulence and coherent structures in eccentric annular channels. *Flow, Turbulence and Combustion*, 82(1):93–120, sep 2008.

Elia Merzari and Hisashi Ninokata. Development of an les methodology for complex geometries. *Nuclear Engineering and Technology*, 41(7):893–906, sep 2009.

L. Meyer. From discovery to recognition of periodic large scale vortices in rod bundles as source of natural mixing between subchannels a review. *Nuclear Engineering and Design*, 240(6):1575–1588, 2010.

L Meyer and K Rehme. Large-scale turbulence phenomena in compound rectangular channels. *Experimental Thermal and Fluid Science*, 8:286–304, 1994.

NURETH–13. *Proceedings of the 13th International Topical Meeting on Nuclear Reactor Thermal Hydraulics(NURETH–13)*, 2009.

NURETH–14. *Proceedings of the 14th International Topical Meeting on Nuclear Reactor Thermal Hydraulics(NURETH–14)*, 2010.

OpenFOAM Documentation. *OpenFOAM – The Open Source CFD Toolbox – User Guide v2.0.1.* OpenFOAM Foundation, 2010.

Estelle Piot and Stavros Tavoularis. Gap instability of laminar flows in eccentric annular channels. *Nuclear Engineering and Design*, 241(11):4615–4620, feb 2011.

S. B. Pope. *Turbulent Flows.* Cambridge University Press, 2000.

G. I. Taylor. The spectrum of turbulence. *Proceedings of the Royal Society of London. Series A - Mathematical and Physical Sciences*, 164(919):476–490, 1938.

N E Todreas and M S Kazimi. *Nuclear Systems I Thermal Hydraulic Fundamentals.* Taylor & Francis, Washington, 1993.

S. Tóth and A. Aszódi. Cfd analysis of flow field in a triangular rod bundle. *Nuclear Engineering and Design*, 240(2):352–363, 2010.

David C. Wilcox. *Turbulence Modeling for CFD.* DCW Industries, 1993.

B.H. Yan and L. Yu. Urans simulation of the turbulent flow in a tight lattice: Effect of the pitch to diameter ratio. *Progress in Nuclear Energy*, 53(4):428–437, may 2011.

B.H. Yan, H.Y. Gu, and L. Yu. Numerical simulation of large scale vortex structure and flow pulsation in rectangular channels. *Progress in Nuclear Energy*, 54(1):29–35, jan 2012a.

B.H. Yan, H.Y. Gu, and L. Yu. Numerical simulation of the coherent structure and turbulent mixing in tight lattice. *Progress in Nuclear Energy*, 54(1):81–95, jan 2012b.

Y.Q. Yu, B.H. Yan, X. Cheng, and H.Y. Gu. Simulation of turbulent flow inside different subchannels in tight lattice bundle. *Annals of Nuclear Energy*, 38(11):2363–2373, nov 2011.

List of Figures

List of Tables

Appendix A

Turbulence Models

The governing equations for the three low-Re turbulence models are listed here.

A.1 LaunderSharmeKE

The low-Re Launder-Sharma $k-\varepsilon$ turbulence model was developed by Launder and Sharma [1974]. The governing equations are

$$\frac{Dk}{Dt} = \frac{\partial}{\partial x_j}\left[(\nu + \frac{\nu_t}{\sigma_k})\frac{\partial k}{\partial x_j}\right] + P_k - \tilde{\varepsilon} - D \tag{A.1}$$

$$\frac{D\tilde{\varepsilon}}{Dt} = \frac{\partial}{\partial x_j}\left[(\nu + \frac{\nu_t}{\sigma_\varepsilon})\frac{\partial \tilde{\varepsilon}}{\partial x_j}\right] + C_{\varepsilon 1} f_1 \frac{\tilde{\varepsilon}}{k} P_k - C_{\varepsilon 2} f_2 \frac{\tilde{\varepsilon}^2}{k} + E \tag{A.2}$$

The turbulence viscosity is given by:

$$\nu_t = C_\mu f_\mu \frac{k^2}{\varepsilon} \tag{A.3}$$

The model constants are given in Table A.1. The parameters P_k, S, S_{ij}, $C_{\varepsilon 1}$, $C_{\varepsilon 2}$, C_μ and σ_k are the same as that of the simple $k-\varepsilon$ turbulence model, mentioned in Table 2.2.

A.2 LamBremhorstKE and LienLeschzinerLowRe

The low-Re models by Lam and Bremhorst [1981] and Lien and Leshziner [1995] have identical governing equations, and the difference is in the formulation of the damping functions. The governing equations are:

$$\frac{Dk}{Dt} = \frac{\partial}{\partial x_j}\left[(\nu + \frac{\nu_t}{\sigma_k})\frac{\partial k}{\partial x_j}\right] + P_k - \varepsilon \tag{A.4}$$

Table A.1: Model coefficients for low-Re Launder-Sharma $k-\varepsilon$ turbulence model (Launder and Sharma [1974])

Coefficient	Value
$\tilde{\varepsilon}$	ε - D
D	$2\nu(\frac{\partial\sqrt{k}}{\partial x_j})^2$
E	$2\nu\nu_t\left(\frac{\partial^2 u_i}{\partial x_j \partial x_k}\right)^2$
f_μ	$e^{\left(\frac{-3.4}{(1+R_T/50)^2}\right)}$
f_1	1
f_2	$1-0.3e^{(-R_T^2)}$
R_T	$\frac{k^2}{\nu\tilde{\varepsilon}}$
σ_ε	1.22

Table A.2: Model coefficients for low-Re Lam-Bremhorst $k-\varepsilon$ turbulence model (Lam and Bremhorst [1981])

Coefficient	Value
f_μ	$\left[1-e^{(1-0.0165Re_n)}\right]^2\left(1+\frac{20.5}{Re_t}\right)$
f_1	$1+(\frac{0.05}{f_\mu})^3$
f_2	$1-e^{(-Re_t^2)}$
Re_n	$\frac{\sqrt{k}Y_n}{\nu}$
Re_t	$\frac{k^2}{\nu\varepsilon}$

$$\frac{D\varepsilon}{Dt} = \frac{\partial}{\partial x_j}\left[(\nu+\frac{\nu_t}{\sigma_\varepsilon})\frac{\partial\varepsilon}{\partial x_j}\right] + C_{\varepsilon 1}f_1\frac{\varepsilon}{k}P_k - C_{\varepsilon 2}f_2\frac{\varepsilon^2}{k} \tag{A.5}$$

The turbulence viscosity is expressed similar to the formulation in Equation A.3. The damping functions for the two turbulence models are mentioned in Table A.2 and A.3.

Y_n is the distance to the nearest wall.

Table A.3: Model coefficients for low-Re Lien-Leschziner $k-\varepsilon$ turbulence model (Lien and Leshziner [1995])

Coefficient	Value
f_μ	$\frac{1-e^{(-0.016y^*)}}{1-e^{(-0.263y^*)}}$
f_1	$1+\frac{P'_k}{P_k}$
f_2	$1-0.3e^{(-R_T^2)}$
y^*	$y(\frac{\sqrt{k}}{\nu})$
R_T	$\frac{k^2}{\nu\varepsilon}$
P'_k	$\left(\frac{1.92[1-0.3e^{(-R_T^2)}]k^{3/2}}{3.53y[1-e^{(-0.263y^*)}]}\right)e^{-0.00222y^{*2}}$

The parameters P_k, S, S_{ij}, $C_{\varepsilon 1}$, $C_{\varepsilon 2}$, C_μ, σ_k and σ_ε are the same as that of the simple $k-\varepsilon$ turbulence model, given in Table 2.2.